UTS UNIVERSITY OF TECHNOLOGY SYDNEY

Measurement and Modelling of Magnetic Properties of Fe-based Amorphous Magnetic Material

by Pejush Chandra Sarker

Thesis submitted in fulfilment of the requirements for the degree of

Doctor of Philosophy

under the supervision of Professor Youguang Guo, Associate Professor Hai Yan Lu, and Professor Jian Guo Zhu

University of Technology Sydney
Faculty of Engineering and Information Technology

February 2022

Title of the thesis:

Measurement and Modelling of Magnetic Properties of Fe-based Amorphous Magnetic Material

Ph.D. student:

Pejush Chandra Sarker

Email: pejushchandra.sarker@student.uts.edu.au

Principal Supervisor:

Professor Youguang Guo

Email: youguang.guo-1@uts.edu.au

Co-Supervisor:

Associate Professor Haiyan Lu

Email: haiyan.lu@uts.edu.au

Co-Supervisor:

Professor Jian Guo Zhu

Email: jianguo.zhu@sydney.edu.au

Address:

School of Electrical and Data Engineering

Faculty of Engineering and Information Technology

University of Technology Sydney, 15 Broadway, Ultimo, NSW 2007, Australia

CERTIFICATE OF ORIGINAL AUTHORSHIP

I, Pejush Chandra Sarker declare that this thesis, is submitted in fulfilment of the requirements for the award of Doctor of Philosophy, in the School of Electrical and Data Engineering at the University of Technology Sydney.

This thesis is wholly my own work unless otherwise referenced or acknowledged. In addition, I certify that all information sources and literature used are indicated in the thesis.

This document has not been submitted for qualifications at any other academic institution.

This research is supported by the Australian Government Research Training Program.

Signature: Production Note:
Signature removed prior to publication.

Date: 20 February 2022

Acknowledgments

First and foremost, I would like to express special appreciate and heart felt thanks to my principal supervisor, Professor Youguang Guo, for the continuous support in my research. His mentorship, guidance and sincere encouragement were invaluable throughout the Doctor of Philosophy (Ph.D.) study. I also would like to thank my co-supervisors, A/Professor Hai Yan Lu and Professor Jian Guo Zhu, for their opinions, suggestions and mentorships in my research.

The gratitude also goes to staff of the school Mr. Brett Lowder and Dr. Mike Zhong, and friend Dr. Shakil Ahamed Khan for their assistances and suggestions to drive the different equipment in the laboratory.

I would like to acknowledge the financial support from University of Technology Sydney and Australia Government.

Finally, I appreciate my family for their cooperations, inspirations and supports during the entire course of my Ph.D. study.

List of Publications

The following articles based on this thesis were published during the study.

Peer reviewed international journal publications:

[1] **P. C. Sarker**, M. R. Islam, Y. Guo, J. G. Zhu, and H. Y. Lu, "State-of-the-art technologies for development of high frequency transformers with advanced magnetic materials," *IEEE Transactions on Applied Superconductivity*, vol. 29, no. 2, Mar. 2019, Art. no. 7000111. (DOI: 10.1109/TASC.2018.2882411)

[2] **P. C. Sarker**, Y. Guo, H. Y. Lu, and J. G. Zhu, "A generalized inverse Preisach dynamic hysteresis model of Fe-based amorphous magnetic materials," *Journal of Magnetism and Magnetic Material*, vol. 514, Nov. 2020, Art. no. 167290. (https://doi.org/10.1016/j.jmmm.2020.167290)

[3] **P. C. Sarker**, Y. Guo, H. Y. Lu, and J. G. Zhu, "Measurement and modelling of rotational core loss of Fe-based amorphous magnetic material under 2-D magnetic excitation," *IEEE Transactions on Magnetics*, vol. 57, no. 11, Nov. 2021, Art no. 8402008. (DOI: 10.1109/TMAG.2021.3111498)

[4] **P. C. Sarker**, Y. Guo, H. Y. Lu, and J. G. Zhu, "Improvement on parameter identification of modified Jiles-Atherton model for iron loss calculation," *Journal of Magnetism and Magnetic Materials*, vol. 542, Jan. 2022, Art. no. 168602. (https://doi.org/10.1016/j.jmmm.2021.168602)

Abstract

Fe-based amorphous magnetic materials are attracting more and more attentions in the low and medium frequency electrical machines and transformers due to their favourable properties of low core loss and high saturation magnetic flux density. In this study, the core loss of a Fe-based amorphous magnetic material (amorphous 1k101) is measured and modelled under alternating and rotating magnetic field excitations. In particular, for numerical analysis using the vector magnetic potential under alternating magnetic field, an inverse magnetic hysteresis model is needed to predict the magnetic field strength from the magnetic flux density. This study proposes a generalised inverse Preisach model for characterisation of the magnetic material which considers the reversible magnetisation and magnetisation dependent hysteresis effect. Thus, the proposed inverse Preisach model improves the accuracy of the prediction of core loss compared to the normal inverse Preisach model. In addition, a modified Jiles-Atherton (J-A) model is utilised for modelling the magnetic material which eliminates the drawbacks of the inverse Preisach model such as high computational time and memory requirements. The implementation of J-A model is associated with model parameter identification which is generally carried out by different optimisation techniques. In the optimisation techniques, an additional error criterion along with conventional error criterion for the identification of the J-A model parameters is proposed in this study which improves the core loss prediction**.** Furthermore, a modified J-A model is proposed to improve the agreement between experimental and calculated results especially at the low magnetic induction levels by introducing a scaling factor in the anhysteretic magnetisation. Both the proposed inverse Preisach model and modified J-A model are verified by the results obtained from experimental methods and existing modellings in the literature. Moreover, the rotating (two-dimensional) magnetic properties of the Fe-based amorphous magnetic material is experimentally investigated in this thesis where a square specimen tester is exploited for experimental measurement. For modelling of the rotational hysteresis loss, an improved and simplified analogical model is proposed and verified for the magnetic material. The total specific rotational loss of the amorphous magnetic material for both circular and elliptical rotating magnetic fields are measured and modelled. Furthermore, an optimal design of a high-power density medium frequency transformer (MFT) using the Fe-based amorphous magnetic material is presented in this thesis where the effects of magnetisation

current is considered in the design process. A prototype of the MFT is utilised for the experimental verification of the design.

Keywords: Fe-based amorphous magnetic material; Direct and inverse Preisach models; Jiles-Atherton model; Hysteresis loss; Dynamic core loss; Alternating core loss; Rotational core loss; Medium frequency transformer.

Content

List of figures

List of Tables

Abbreviations

MFT	Medium frequency transformer
HFT	High frequency transformer
1-D	One-dimensional
J-A	Jiles-Atherton
DC	Direct current
AC	Alternating current
SST	Solid state transformer
GSE	Generalized Steinmetz equation
SiFe	Silicon iron
NiFe	Nickel iron
CoFe	Cobalt iron
SMC	Soft magnetic composite
2-D	Two-dimensional
Fe	Iron
Co	Cobalt
Ni	Nickel
OSE	Original Steinmetz equation
IGSE	Improved generalised Steinmetz equation
UTS	University of Technology Sydney
CUT	Core under test
FEM	Finite-element method
DSP	Digital signal processing
GRG	General reduced gradient
NSE	Natural Steinmetz equation
AWG	American wire gauge
3-D	Three-dimensional
RMS	Root mean square
WCSE	Waveform coefficient Steinmetz equation

Nomenclature*

P	Core loss
t	Time
B	Magnetic flux density
$\mathbf{B}$	Magnetic flux density vector
K_h, K_e, K_{exc}, a, b, and c	Constants associated with core loss separation model
k, α and β	Steinmetz parameters
f_r	Fundamental frequency
f_{eq}	Equivalent frequency associated with OSE model
k_i	Parameter associated with GSE model
f	Frequency
T	Time period
ΔB	Magnetic flux density variation
k_N	Parameter associated with NSE model
K_{FWC}	The ratio of areas of the non-sinusoidal and sinusoidal waveforms
V	Flow rate of the coolant
C_s	Specific heat of fluid
A	Cross section of coolant path
B_m	Maximum magnetic flux density
i_p	Primary current
v_s	Secondary voltage
H	Magnetic field strength
$\mathbf{H}$	Magnetic field strength vector
R_{ref}	Resistance of current sensor
v_R	Voltage across the current sensor resistor
C_r	Resonant capacitance
η	Porosity factor
d_t	Conductor height
M_w	$\alpha_1 d_t \coth\left(\alpha_1 d_t\right)$
D_w	$2\alpha_1 d_t \tanh\left(\frac{\alpha_1 d_t}{2}\right)$
M_w'' and D_w''	Imaginary parts of M_w and D_w respectively
M_w' and D_w'	Real parts of M_w and D_w respectively

* Symbols that are not listed are explained where they firstly appear

α_1	$\sqrt{\frac{j\omega\eta\mu_0}{\rho_r}}$
ω	Angular frequency
μ	Permeability
R_{dc}	DC resistance of the winding
R_{ac}	AC resistance of the winding
Δ	Ratio of thickness of conductor and skin depth
δ	Skin depth
γ	$d_c / (\sqrt{2}\delta)$
d_c	Diameter of conductor
I_{rms}	Root mean square value of current
I'_{rms}	Derivative of I_{rms}
N_s, N_{s1}, N_{s2}	Number of strands, and numbers of strands of primary and secondary windings
d_s	Diameter of a strand.
Δ_s	Ratio of thickness of conductor and skin depth for Litz wire
G_W	Core window width
H_w	Core window height
M	Magnetisation
$\mathbf{M}$	Magnetisation vector
M_{irr}	Irreversible magnetisation
M_{rev}	Reversible magnetisation
H_e	Effective magnetic field strength
M_s	Saturated magnetisation
B_e	Effective magnetic flux density
H_x, H_y	Magnetic field strength components in X and Y-directions
H_n	Magnetic field strength at the last reversal point
L_{lP}	Leakage inductance refer to primary winding
χ	Magnetic susceptibility
χ_{io}	Initial susceptibilities of normal magnetisation
χ_{anho}	Initial susceptibilities of anhysteretic magnetisation
ΔT	Temperature rise
R_{th}	Thermal resistance
I_0	No-load transformer current
B_x, B_y	Magnetic flux density components in-X and Y-directions
A_c	Cross sectional area of the core

K_f	Form factor
R_{ac1} and R_{ac2}	AC resistances of primary and secondary windings
V_p, V_s, I_s, I_p	Voltage and current of primary and secondary windings
d_{ins}, d_{iso}	Thicknesses of insulation and isolation
d_{w1}	Diameter of the primary Litz wire
d_{w2}	Diameter of the secondary Litz wire
W_1	Primary half winding width
W_2	Secondary half winding width
M_{an}	Anhysteretic magnetisation
H_e	Effective magnetic field strength
σ	Conductivity of the amorphous ribbon
d_l	Thickness of amorphous ribbon
A_l	Cross sectional area of the lamination
G, V_0	Constant coefficients depending on material metallurgical properties

Chapter 1 Introduction

1.1 Background of the Research

The increase of the operating frequency reduces the volume and weight of an electro-magnetic device such as medium frequency transformer (MFT). In recent years, MFTs, which are normally used in solid-state transformers (SSTs), have been developed for the emerging applications in smart grids, renewable energy, energy storage, and traction systems [1.1]−[1.6]. According to the Massachusetts Institute of Technology Review in 2010 [1.3], the SST has been considered as one of the highly growing technologies. One of the important elements of SST is the DC-DC converter where MFT is used for galvanic isolation and voltage conversion [1.6]. Fig. 1.1 shows a typical MFT based voltage conversion system where DC-DC converter is used. However, the operating magnetic flux density (B) in a transformer is inversely proportional to the cross-sectional area of the core. Thus, the core material with high saturation magnetic flux density (B_s) is generally recommended for the design of the high-power density MFT. Therefore, researchers and engineers are focusing on the research and development of soft magnetic materials with low core loss and high B_s.

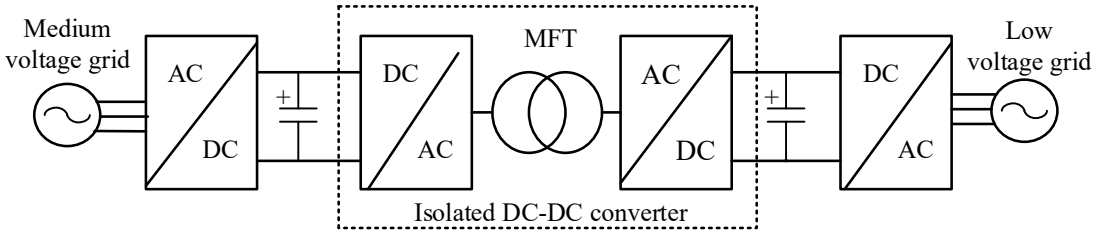

(a)

Fig. 1.1. A typical MFT based voltage conversion system [1.4].

Different soft magnetic materials such as silicon irons (SiFe), amorphous magnetic materials, nanocrystalline materials, and soft ferrites have been developed which are utilised for the applications in different frequency ranges [1.7]. In instance, silicon iron magnetic materials are generally used for low frequency range, whereas amorphous magnetic materials for low and medium frequency ranges, nanocrystalline materials for medium and high frequency ranges, and ferrites for high frequency range [1.8], [1.9].

Since low and medium frequency electrical machines are generally used for high power applications, amorphous magnetic materials are becoming interests as core materials. There are many types of amorphous magnetic materials depending on the chemical compositions such as Fe-based, Co-based and Ni-based. Among the different amorphous magnetic materials, Fe-based amorphous materials are commonly used as the core material due to their high saturation magnetic flux densities and low prices. There are many Fe-based amorphous magnetic suppliers over the world, e.g., Hitachi Metals Ltd., Japan, and Henan ZY Amorphous Technology Co. Ltd., China. In this study, the amorphous 1k101 metal [1.10], [1.11], which is produced by Henan ZY Amorphous Technology Co. Ltd., is used for the investigation of magnetic properties.

In the last decade, different types of transformers were reported in [1.12]−[1.15], where amorphous magnetic materials are used as the core materials. Since the magnetic properties of a core affects the design of transformers and electrical machines, the modelling of the core material is important for their designs. As the transformer operates under the alternating magnetic field, the modelling of alternating (one-dimensional, 1-D) magnetic properties of the magnetic material is generally exploited for its design.

There are generally two types of models used for modelling of magnetic cores under alternating magnetic field. In the first type of modellings, the Steinmetz equation based empirical models [1.16], [1.17] are used for core loss prediction where the Steinmetz parameters are calculated by curve fitting of core loss data of material samples. In the empirical models, the core loss is mainly concerned but other non-linear physical behaviour of the magnetic core is ignored. The empirical model is normally used for fast and easy designing and analysing the electromagnetic devices. On the other hand, for considering actual physical characteristic of the core and realistic magnetic flux distribution throughout the core, incorporation of FEM into the design process is necessary. The main problem of the empirical models is that they cannot be directly incorporated into FEM as the prediction of the pattern of magnetic field strength (H) from magnetic flux density (B), which is one of the steps in the FEM analysis [1.18], is not possible using the empirical models. Therefore, for incorporation of magnetic properties of a magnetic material with FEM, a single value B-H curve is used along with the empirical models [1.19]. Since the complete physical behaviour of a magnetic material

cannot be expressed by a single value *B*-*H* curve of the material, the actual results cannot be obtained by this approach [1.19].

On the other hand, in the second type of modellings, it is possible to predict the core loss by tracing explicitly the magnetisation trajectory of magnetic flux density versus magnetic field strength. In addition, the actual physical behaviours of the magnetic cores are considered, and the patterns of *H* from *B* or its vice versa are possible to be calculated by this type of modellings. Preisach [1.20]−[1.22] and Jiles-Atherton (J-A) [1.23]−[1.26] models are generally utilised as the second type of modellings. Both Preisach and J-A models are utilised in this study for modelling the selected Fe-based magnetic material. The electromagnetic devices, e.g., transformers are generally subjected to both sinusoidal and non-sinusoidal excitations. Therefore, in this study the modelling of the magnetic material is carried out for both types of excitations. However, in this study the selected amorphous magnetic material has been modelled by an improved magnetisation dependent Preisach model. Moreover, a generalised inverse Presich model has been studied for investigation of the magnetic material for up to medium frequency range.

The drawbacks of the Preisach model are that the model needs more computational time and memory resources compared to the J-A model [1.27], [1.28]. Consequently, J-A model becomes popular and useful tools for characterisation of magnetic materials [1.29]. The accurate J-A model parameter identification is one of the challenges of the implementation of the J-A model. Improved parameter identification technique as well as modified J-A model have been studied in this study.

The magnetic field in transformers generally varies with time which is known as alternating magnetic field that can also be defined as one-dimensional (1-D) magnetic field since the magnetic field is considered as only time varying along a fixed orientation. On the other hand, for some cases, e.g., the rotating electrical machines and the T-joints of the three-phase transformers, the magnetic field varies with respect to both time and orientation [1.30], [1.31], and the dissipated power in the magnetic core due to the rotating magnetic field is different from that caused by the alternating magnetic field. In many rotating electrical machines, the rotational stator core loss can be accounted for up to half of the total core losses [1.31]. Therefore, it is important to take into account the rotational core losses of magnetic materials so that the proper thermal and laminated insulation

specifications can be contemplated in the design of the electrical machines. Recently, various rotating electrical machines of amorphous material cores were reported by different researchers [1.32]−[1.34] due to their low core loss property especially compared to the silicon steel sheets. In this thesis, the 2-D vector magnetic properties of the selected Fe-based amorphous magnetic material are investigated under 2-D rotating magnetic fields. In addition, the modelling of rotational core loss is carried out in this study.

Since the magnetic core material with high saturation magnetic flux density is generally recommended for the design of the MFT, the Fe-based amorphous magnetic material can be a good choice as a core material. However, the design of an MFT is associated with many design variables such as core parameters, frequency, voltage, magnetic flux density, number of turns and so on. The change of one variable affect the other parameters and design objective functions such as efficiency and power density. Therefore, an optimisation technique is generally exploited to cope with the multi-variables and multi-objectives based MFT design. In this research, an optimal design process of a high-power density MFT using the Fe-based magnetic material has been also presented.

1.2 Research Gaps

For design and performance analysis of electromagnetic devices and systems, the proper prediction of iron or core loss in their magnetic cores is essential as the iron loss is one of the key heat sources in the devices. Steinmetz equation based empirical model is the easiest way to model the magnetic material but the model does not provide the actual properties of the material. Consequently, inverse Preisach and inverse J-A model, which are generally incorporated with the finite element method, are commonly employed to calculate the magnetic field distribution by using the vector magnetic potential, which requires the prediction of magnetic field strength from the magnetic flux density.

In the literature, different inverse Preisach models were proposed in [1.35], [1.36] and [1.37], where irreversible magnetisation is mainly considered. The magnetisation process is also affected by the reversible magnetisation, and magnetisation dependent hysteresis effects that is normally considered by a feedback coefficient. Therefore, for more accurate modelling of magnetic material, the inclusion of the reversible magnetisation and the

feedback magnetisation is required to be considered with the irreversible magnetisation in the inverse Preisach model. In addition, to the best knowledge of the author of this thesis, no investigation has been reported in the literature on the effects of minor loops on characterisation process using the inverse Preisach models. Moreover, neither has the normal or inverse Preisach models been used to characterise the selected Fe-based amorphous magnetic material (amorphous 1k101).

For implementation of the J-A model for characterisation of any magnetic material, firstly it requires identification of model parameters. The optimisation techniques [1.38]−[1.42] as well as other similar methods [1.26], [1.28] are generally exploited in such a way that an error becomes the minimum. The error criterion is generally based on the error between experimental and simulated B or H. The identified model parameters are then used for calculation of B-H loop, and the iron loss is finally obtained from the calculated B-H loop. The detailed analysis of measured and experimental B-H loop shows that the minimum relative error in the iron loss calculation does not often occur simultaneously with the minimum root mean square error of calculated B or H. It is also observed that a slight increase of root mean square (RMS) error between calculated and experimental waveforms of B or H, the relative error of the calculation of iron loss decreases significantly. Therefore, in the optimisation techniques double error criteria, where one is based on the conventional root mean square of error and the other is based on the relative iron loss error, can be a good technique for high accuracy of iron loss calculation along with satisfactory simulated waveform of B or H. If the RMS error of calculated B or H slightly increases, the error in the calculation of coercive magnetic force (H_c) increases a little bit. To improve the calculation of H_c as well as B or H, a scaling factor can be included in the anhysteretic magnetisation instead of its general inclusion into the equation of rate of change of reversible magnetisation. The inclusion of the scaling factor in the anhysteretic magnetisation simultaneously reduces the rate of irreversible magnetisation and anhysteretic magnetisation, and consequently it provides better agreement between experimental and calculated results than the existing inclusion way of the scaling factor.

The 2-D rotational core losses of different magnetic materials, such as soft magnetic composite materials and silicon steels, were investigated and modelled by different researchers [1.43]−[1.45]. The 2-D vector magnetic properties of Metglas 2605 HB1 and

Metglas 2650S-2 amorphous materials were examined at constant frequencies in [1.46] and [1.47], respectively. In those works, the core loss modellings were not carried out. However, no investigation and modelling of 2-D magnetic core loss of the selected Fe-based magnetic material (Amorphous 1k101) have been yet done. From the literature [1.31], it is observed that, an analogical approach which is based on the torque equation of a single-phase induction motor is utilised to model the rotational hysteresis loss. In the same way, it can be observed that the equation of developed mechanical power of a three-phase induction motor, which is simpler than torque equation of a single-phase induction motor, can be also used as an analogical approach to model the rotational hysteresis loss. Therefore, it is a great aspect to use the developed mechanical power equation of a three-phase induction motor to model the rotational hysteresis loss for not only simplifying the approach but also improving the accuracy of the prediction of the rotational hysteresis loss.

The optimal design process of the MFT involves different design constraints and modelling of different parameters. In the literature, researchers focused on different design constraints and parameters' modellings such as the ripple voltages [1.48], the isolation requirement [1.49]−[1.51], thermal models [1.52], Litz wire modelling for leakage inductance [1.53]], and winding loss modelling [1.54]. However, the no-load current, which is mainly responsible for magnetising current, of a high-power density MFT at low and medium power ranges affect the efficiency as well as the overall leakage inductance. Therefore, the no-load current is also essential to be counted in the design of the high-power density MFT. The designs of MFTs which are only based on the empirical core loss model for consideration of the magnetic properties of cores, generally ignore the effect of no-load current.

1.3 Research Objectives

Based on the above-mentioned research background and research gaps, the main objectives of the study are as follows:

- To characterise the selected Fe-based amorphous magnetic material experimentally, and model the magnetic material by improved direct and inverse Preisach model.

- To model the selected Fe-based amorphous magnetic material by modified J-A model.
- To investigate the 2-D rotating magnetic properties of the Fe-based amorphous magnetic material experimentally, and model the corresponding 2-D core loss.
- To design of a high-power density MFT using the Fe-based amorphous magnetic material.

1.4 Contributions of the Research

Based on the above-mentioned research gaps and objectives, the contributions of this thesis are discussed below.

The study has firstly been started with the experimentally measurement of core loss of the selected Fe-based magnetic material under alternating magnetic field. After that the magnetic material is modelled by Preisach and inverse Preisach models. The main contributions of this case are as follows: (i) characterisation of the static hysteretic effects of the selected Fe-based amorphous magnetic materials by the normal and inverse Preisach models; (ii) development of a generalised inverse Preisach model based on the generalised Preisach model by incorporating the reversible magnetisation and magnetisation dependent hysteresis effects; (iii) development of a new technique to find out the feedback coefficient of the generalised Preisach model whose value varies with the magnitude of magnetic flux density.

The selected Fe-based amorphous magnetic material is also characterised under alternating magnetic field by modified J-A model. The main contributions in this case include incorporation of an additional error criterion along with general error criterion for the identification of the J-A model parameters, and a proposal of a modified J-A model where scaling factor is incorporated into the anhysteretic magnetisation of original J-A model in order to reduce the rate of irreversible magnetisation and anhysteretic magnetisation especially at the low magnetic induction levels.

The vector magnetic properties of the Fe-based amorphous magnetic material have been carried out under the 2-D rotating magnetic field. The key contributions in this case are: (i) measurement of the rotational core losses of the magnetic material at different magnetic flux densities and frequencies; (ii) proposal of an improved analogical model

for modelling of the rotational hysteresis loss; and (iii) modelling of the total core loss of the selected Fe-based amorphous magnetic material under circularly and elliptically rotating magnetic field.

Another target of this study is to design a high-power density medium frequency transformer using the selected Fe-based magnetic material. In this study, an optimal design of a high-power density MFT is proposed which includes the effect of the no-load currents in the empirical based design process.

The above-mentioned proposed models, parameter identification techniques related to the different models, and optimal design of the MFT are validated by comparing the calculated results with experimental and/or works in the literature.

1.5 Thesis Outline

This thesis consists of seven chapters where each chapter contains different contents of the study. Short descriptions of each chapter are discussed as follows:

Chapter 1 presents background of the study which directs scopes of the study. In addition, the contributions of the research are included in this chapter. Moreover, the chapter presents outline of the thesis.

Chapter 2 presents the literature survey on previous works which are related with this study. The chapter includes the general magnetisation process in a magnetic material, experimental techniques for their conventional core loss measurement, and their mathematical models such as empirical models, Preisach model and Jiles-Atherton models. In addition, the chapter presents descriptions of two-dimensional rotational core loss measurement testers, and measurement methods. The different design parameters of a medium frequency transform are also explained in this chapter.

Chapter 3 presents the experimental characterisation of the selected Fe-based amorphous materials. Then based on the experimental results, the magnetic material is modelled by using direct Preisach and inverse Preisach models. This chapter also includes a proposal of a generalised inverse Preisach model based on the generalised Preisach model by incorporating the reversible magnetisation and magnetisation dependent hysteresis effects into the conventional model. Investigation of the effects of minor loops are also carried

out into the chapter. Finally, the validation of the proposed method is shown by a comparison between calculated and experimental results.

Chapter 4 presents a proposal of an additional error criterion along with general existing error criterion for the identification of the J-A model parameters by optimisation techniques. The chapter also includes a proposal of a modified J-A model. Dynamic losses are also incorporated with the static modified J-A model to make the model generalised. The chapter presents the validations of the proposed method of identifying the model parameters, and proposed modified J-A model by comparing the calculated results with experimental and recently works in the literature.

Chapter 5 presents the experimental rotational core loss measurement of the selected Fe-based amorphous magnetic material. It also includes investigation of different loci of magnetic flux density (**B)** and magnetic field strength (**H)** vectors under the various types of rotational magnetic excitations. A proposal of an improved and simplified analogical model of the rotational hysteresis loss is presented in this chapter. Moreover, investigation of dynamic loss and investigation of effects of the changing axis ratio of **B** loci on the total loss of the material are experimentally carried out. The chapter includes a verification of the proposed model by a comparison between experimental and simulation results.

Chapter 6 presents a methodology of an optimum design of an MFT. The magnetisation current affects the design of an MFT especially for high power density. This chapter considers the magnetising current in the empirical based design process. Modelling of a round Litz wire is presented in this chapter. Based on the design consideration, a prototype of a 2.5 kW, 1 kHz MFT is considered, and that prototype is used for experimental verification of the design.

The chapter 7 presents the conclusion of the study. Future research directions are also included in this chapter.

References

[1.1] M. R. Islam, Y. G. Guo, and J. G. Zhu, "A multilevel medium-voltage inverter for step-up-transformer-less grid connection of photovoltaic power plants," *IEEE J. Photo.*, vol. 4, no. 3, pp. 881–889, May 2014.

[1.2] M. R. Islam, Y. G. Guo, and J. G. Zhu, "A medium-frequency transformer with multiple secondary windings for medium-voltage converter-based wind turbine generating systems," *J. Appl. Physics*, vol. 113, no. 17, May 2013, Art. no. 17A324.

[1.3] X. She, A. Q. Huang, and R. Burgos, "Review of solid-state transformer technologies and their application in power distribution systems," *IEEE J. Emer. Sele. Topics Power Electron*., vol. 1, no. 3, pp. 186–198, Sep. 2013.

[1.4] P. Shuai and J. Biela, "Influence of material properties and geometric shape of magnetic cores on acoustic noise emission of medium-frequency transformers," *IEEE Transactions on Power Electron*., vol. 32, no. 10, pp. 7916–7931, Oct. 2017.

[1.5] S. Zhao, Q. Li, F. C. Lee, and B. Li, "High-frequency transformer design for modular power conversion from medium-voltage ac to 400 Vdc," *IEEE Trans. Power Electron.*, vol. 33, no. 9, pp. 7545–7557, Sept. 2018.

[1.6] M. A. Bahmani, T. Thiringer, and M. Kharezy, "Design methodology and optimization of a medium-frequency transformer for high-power dc–dc applications," *IEEE Trans. Ind. Appl.*, vol. 52, no. 5, pp. 4225–4233, Sept.-Oct. 2016.

[1.7] A. Krings, A. Boglietti, A. Cavagnino, and S. Sprague, "Soft magnetic material status and trends in electric machines," *IEEE Trans. Ind. Electron*., vol. 64, no. 3, pp. 2405–2414, Mar. 2017.

[1.8] T. Kauder and K. Hameyer, "Performance factor comparison of nanocrystalline, amorphous, and crystalline soft magnetic materials for medium-frequency applications," *IEEE Trans. Magn.,* vol. 53, no. 11, Nov. 2017, Art no. 8401504.

[1.9] A. Krings, M. Cossale, A. Tenconi, J. Soulard, A. Cavagnino, and A. Boglietti, "Magnetic materials used in electrical machines: a comparison and selection guide for early machine design," *IEEE Ind. Appl. Mag.,* vol. 23, no. 6, pp. 21–28, Nov.-Dec. 2017.

[1.10] Henan ZY Amorphous Technology Co. Ltd. [Online]. Available: https://www.zyamorphous.com/. Accessed on: Sep. 25, 2019.

[1.11] Guangzhou Amorphous Electronic Technology Co. Ltd. [Online]. Available: https://www.coilcore.com/. Accessed on: Dec. 22, 2019.

[1.12] Y. Xu, L. Chen, W. Guo, C. Shangguan, J. Zuo, and K. He, "Optimal design of medium-frequency Fe-based amorphous transformer based on genetic algorithm," *IEEE Trans. Plas. Sci.*, vol. 46, no. 10, pp. 3240–3248, Oct. 2018.

[1.13] M. R. Islam, Y. Guo, and J. Zhu, "A high-frequency link multilevel cascaded medium-voltage converter for direct grid integration of renewable energy systems," *IEEE Trans. Power Electron.*, vol. 29, no. 8, pp. 4167–4182, Aug. 2014.

[1.14] L. Zhang, D. Zhang, H. Shui, Y. Yuan, Q. Pei, and J. Zhu, "Optimisation design of medium frequency transformer for the offshore dc grid based on multi-objective genetic algorithm," *IET Power Electron.*, vol. 10, no. 15, pp. 2157–2162, Dec. 2017.

[1.15] M. Jafari, Z. Malekjamshidi, G. Lei, T. Wang, G. Platt, and J. Zhu, "Design and implementation of an amorphous high-frequency transformer coupling multiple converters in a smart microgrid," *IEEE Trans. Ind. Electron.*, vol. 64, no. 2, pp. 1028–1037, Feb. 2017.

[1.16] I. Villar, U. Viscarret, I. Etxeberria-Otadui, and A. Rufer, "Global loss evaluation methods for nonsinusoidally fed medium-frequency power transformers," *IEEE Trans. Ind. Electron.*, vol. 56, no. 10, pp. 4132–4140, Oct. 2009.

[1.17] P. K. Venkatachalam, C. R. Sullivan, T. Abdallah, and H. Tacca, "Accurate prediction of ferrite core loss with nonsinusoidal waveforms using only Steinmetz parameters," In Proc. *IEEE Workshop Comp. Power Electron.,* pp. 36-41, 3-4 Jun. 2002,

[1.18] N. Sadowski, N. J. Batistela, J. P. A. Bastos, and M. Lajoie-Mazenc, “An inverse Jiles-Atherton model to take into account hysteresis in time-stepping finite-element calculations,” *IEEE Trans. Magn.*, vol. 38, no. 2, pp. 797–800, Mar. 2002.

[1.19] S. Hussain and D. A. Lowther, “The Modified Jiles–Atherton Model for the accurate prediction of iron losses,” *IEEE Trans. Magn.*, vol. 53, no. 6, Jun. 2017, Art no. 7300504.

[1.20] I. D. Mayergoyz, “Dynamic Preisach models of hysteresis,” *IEEE Trans. Magn.,* vol. 24, no. 6, pp. 2925–2927, Nov. 1988.

[1.21] S. R. Naidu, “Simulation of the hysteresis phenomenon using Preisach's theory,” *IEE Proc. A Phy. Sci. Mea. Inst. Man. Edu.,* vol. 137, no. 2, pp. 73–79, Mar. 1990.

[1.22] E. Cardelli, E. D. Torre, and B. Tellini, “Direct and inverse Preisach modeling of soft materials,” IEEE Trans. Magn., vol. 36, no. 4, pp. 1267–1271, Jul. 2000.

[1.23] D. C. Jiles and D. L. Atherton, “Theory of ferromagnetic hysteresis,” *J. Magn. Magn. Mat.*, vol. 61, no. 1–2, pp. 48–60, Sep. 1986.

[1.24] D. C. Jiles and J. B. Thoelke, “Theory of ferromagnetic hysteresis: determination of model parameters from experimental hysteresis loops,” *IEEE Trans. Magn.*, vol. 25, no. 5, pp. 3928–3930, Sep. 1989.

[1.25] D. C. Jiles, J. B. Thoelke, and M. K. Devine, “Numerical determination of hysteresis parameters for the modeling of magnetic properties using the theory of ferromagnetic hysteresis,” *IEEE Trans. Magn.*, vol. 28, no. 1, pp. 27–35, Jan. 1992.

[1.26] P. Kis and A. Iványi, “Parameter identification of Jiles–Atherton model with nonlinear least-square method,” *Phy. B: Cond. Mat*., vol. 343, nos. 1–4, pp. 59-64, Jan. 2004.

[1.27] S. Rosenbaum, M. Ruderman, T. Strohla, and T. Bertram, “Use of Jiles–Atherton and Preisach Hysteresis Models for Inverse Feed-Forward Control,” *IEEE Trans. Magn.*, vol. 46, no. 12, pp. 3984–3989, Dec. 2010.

[1.28] M. Toman, G. Stumberger, and D. Dolinar, “Parameter identification of the Jiles–Atherton hysteresis model using differential evolution,” *IEEE Trans. Magn.*, vol. 44, no. 6, pp. 1098–1101, Jun. 2008.

[1.29] Z. Birčáková, P. Kollár, J. Füzer, R. Bureš, and M. Fáberová, “Magnetic properties of selected Fe-based soft magnetic composites interpreted in terms of Jiles-Atherton model parameters,” *J. Magn. Magn. Mater*., volume 502, May 2020, Art. no. 166514.

[1.30] J. C. Akiror, J. Wanjiku, P. Pillay, J. Cave, and A. Merkhouf, “Rotational core loss magnetizer: design and measurements,” *IEEE Trans. Ind. Appl., vol.* 54, no. 5, 4355–4364, Sep.-Oct. 2018.

[1.31] J. G. Zhu, “Numerical modelling of magnetic materials for computer aided design of electromagnetic devices,” *Ph.D. Dissertation*, School of Electrical Engineering, University of Technology Sydney, Australia, July 1994.

[1.32] N. Ertugrul, R. Hasegawa, W. L. Soong, J. Gayler, S. Kloeden, and S. Kahourzade, “A novel tapered rotating electrical machine topology utilizing cut amorphous magnetic material,” *IEEE Trans. Magn.,* vol. 51, no. 7, Jul. 2015, Art. 8106006.

[1.33] Z. Wang, *et al*., “Development of a permanent magnet motor utilizing amorphous wound cores,” *IEEE Trans. Magn., vol.* 46, no. 2, pp. 570–573, Feb. 2010.

[1.34] S. Kahourzade, N. Ertugrul, and W. L. Soong, “Loss analysis and efficiency improvement of an axial-flux PM amorphous magnetic material machine,” *IEEE Trans. Ind. Electron*., vol. 65, no. 7, pp. 5376–5383, Jul. 2018.

[1.35] Y. Bernard, E. Mendes, and F. Bouillault, “Dynamic hysteresis modeling based on Preisach model,” *IEEE Trans. Magn.* vol. 38, no. 2, pp. 885–888, Mar. 2002.

[1.36] J. E. Cardelli, E. D. Torre, and B. Tellini, “Direct and inverse Preisach modeling of soft materials,” *IEEE Trans. Magn*., vol. 36, no. 4, pp. 1267–1271, Jul. 2000.

[1.37] E. Fallah and J. S. Moghani, “A new approach for finite-element modeling of hysteresis and dynamic effects,” *IEEE Trans. Magn.,* vol. 42, no. 11, pp. 3674–3681, Nov. 2006.

[1.38] P. R. Wilson, J. N. Ross, and A. D. Brown, “Optimizing the Jiles-Atherton model of hysteresis by a genetic algorithm,” *IEEE Trans. Magn.*, vol. 37, no. 2, pp. 989–993, Mar. 2001.

[1.39] D. Lederer, H. Igarashi, A. Kost, and T. Honma, “On the parameter identification and application of the Jiles-Atherton hysteresis model for numerical modelling of measured characteristics,” *IEEE Trans. Magn.*, vol. 35, no. 3, pp. 1211–1214, May 1999.

[1.40] I. Podbereznaya and A. Pavlenko, “Accounting for dynamic losses in the Jiles-Atherton model of magnetic hysteresis,” *J. Magn. Magn. Mater*., volume 513, Nov. 2020, Art. 167070.

[1.41] Y. Li, J. Zhu, Yongjian Li, H. Wang, and L. Zhu, “Modeling dynamic magnetostriction of amorphous core materials based on Jiles–Atherton theory for finite element simulations,” *J. Magn. Magn. Mater*., vol.529, Jul. 2021, Art. 167854.

[1.42] F. R. Fulginei and A. Salvini, “Softcomputing for the identification of the Jiles-Atherton model parameters,” *IEEE Trans. Magn.*, vol. 41, no. 3, pp. 1100–1108, Mar. 2005.

[1.43] Y. G. Guo, J. G. Zhu, and J. J. Zhong, “Measurement and modelling of magnetic properties of soft magnetic composite material under 2D vector magnetisations,” *J. Mag. Magn. Mat.,* 302, no. 1, pp. 14–19, Jul. 2006.

[1.44] M. Enokizono, T. Suzuki and J. D. Sievert, “Measurement of iron loss using rotational magnetic loss measurement apparatus,” *IEEE Trans. J. Magn. Jpn.*, vol. 6, no. 6, pp. 508–514, Jun. 1991.

[1.45] A. Cecchetti, G. Ferrari, F. Masoli, and G. Soardo, “Rotational power losses in 3% SiFe as a function of frequency,” *IEEE Trans. Magn*., vol. 14, no. 5, pp. 356–358, Sep. 1978.

[1.46] S. Ueno, T. Todaka, and M. Enokizono, “Measurement of vector magnetic properties of Fe–Si–B amorphous material,” *IEEE Trans. Magn*., vol. 47, no. 10, pp. 3188–3191, Oct. 2011.

[1.47] M. Enokizono, G. Shirakawa, and J. Sievert, “Anomalous anisotropy and rotational magnetic properties of amorphous sheet,” *J. Magn. Magn. Mater*., vol. 112, no. 1–3, pp. 195–199, Jul. 1992.

[1.48] P. Huang, *et al*., “Optimal design and implementation of high-voltage high-power silicon steel core medium-frequency transformer,” *IEEE Trans. Ind. Electron.*, vol. 64, no. 6, pp. 4391–4401, Jun. 2017.

[1.49] G. Ortiz, J. Biela, and J. W. Kolar, “Optimized design of medium frequency transformers with high isolation requirements,” *IECON 2010 - 36th Ann.l Conf. IEEE Ind.l Electron. Society*, Glendale, AZ, 2010, pp. 631–638.

[1.50] M. Jaritz, S. Blume, and J. Biela, “Design procedure of a 14.4 kV, 100 kHz transformer with a high isolation voltage (115 kV),” *IEEE Trans. Dielec. Elect. Ins.*, vol. 24, no. 4, pp. 2094–2104, 2017.

[1.51] S. Zhao, Q. Li, and F. C. Lee, “High frequency transformer design for modular power conversion from medium voltage ac to 400V dc,” *2017 IEEE Appl. Power Electron. Conf. Exp. (APEC)*, Tampa, FL, 2017, pp. 2894–2901.

[1.52] M. Leibl, G. Ortiz, and J. W. Kolar, “Design and experimental analysis of a medium-frequency transformer for solid-state transformer applications,” *IEEE J. Emerg. Select. Top. Power Electron.*, vol. 5, no. 1, pp. 110–123, Mar. 2017.

[1.53] E. L. Barrios, A. Ursúa, L. Marroyo, and P. Sanchis, “Analytical design methodology for litz-wired high-frequency power transformers,” *IEEE Trans. Ind. Electron.*, vol. 62, no. 4, pp. 2103–2113, Apr. 2015.

[1.54] M. A. Bahmani, T. Thiringer, and M. Kharezy, “Design methodology and optimization of a medium-frequency transformer for high-power dc–dc applications,” *IEEE Trans. Ind. Appl.*, vol. 52, no. 5, pp. 4225–4233, Sept.-Oct. 2016.

Chapter 2 Literature Review

The existing works in the literature related to this study are discussed in this chapter. When a magnetic material is exposed to a magnetic field strength, magnetisation occurs and electromagnetic power loss is dissipated there. Before designing the electromagnetic devices, magnetisation and power loss of the core are necessary to be investigated. Therefore, proper experimental and mathematical models are essential for characterisation of a magnetic material under both alternating and rotating magnetic fields. This chapter presents different ways of characterisation of magnetic materials. In addition, the general design parameters of an MFT is discussed in this chapter.

2.1 Magnetisation Process

Magnetisation is obtained from two ways: one is from permanent magnet and another from electromagnetic process where electrical charge motion generates a magnetic field. Magnetic field obtained from the permanent magnet is uncontrollable. Consequently, in the electromagnetic devices, the electromagnetic process is generally utilised for magnetisation process where a magnetic material is normally used for high magnetisation. When magnetic field strength (H), which is the magnetomotive force per unit distance, is applied to a magnetic material, a magnetic field is produced there, and its response to H is defined by the magnetic flux density (B). Thus, a magnetic material is generally characterised by the relation between H and B or its B-H loop which is also known as magnetisation curve. Fig. 2.1 shows the general pattern of B-H loop of a magnetic material. The power dissipation in the magnetic materials is presented by the area of B-H loop. Therefore, depending on the B-H loops, the magnetic materials can be divided into soft magnetic materials and hard magnetic materials [2.1]. The B-H loops of soft magnetic materials are generally narrow which indicates low power dissipation and low magnetic energy storing. On the other hand, the hard-magnetic materials, the B-H loops are generally wide which represents high power loss as well as the high magnetic energy storing. From the Fig. 2.1, it is observed that for a specific magnetic field strength, two values of magnetic flux density are obtained which happens due to the hysteresis effect of magnetic material. However, the pattern of initial magnetisation curve is a single value

B-H curve, as shown Fig. 2.2. From Figs. 2.1 and 2.2, it is observed that the magnetic material shows non-linear properties especially at the vicinity of knee point as well as saturation region. Magnetic domain's theory is commonly used to explain the magnetisation of magnetic materials.

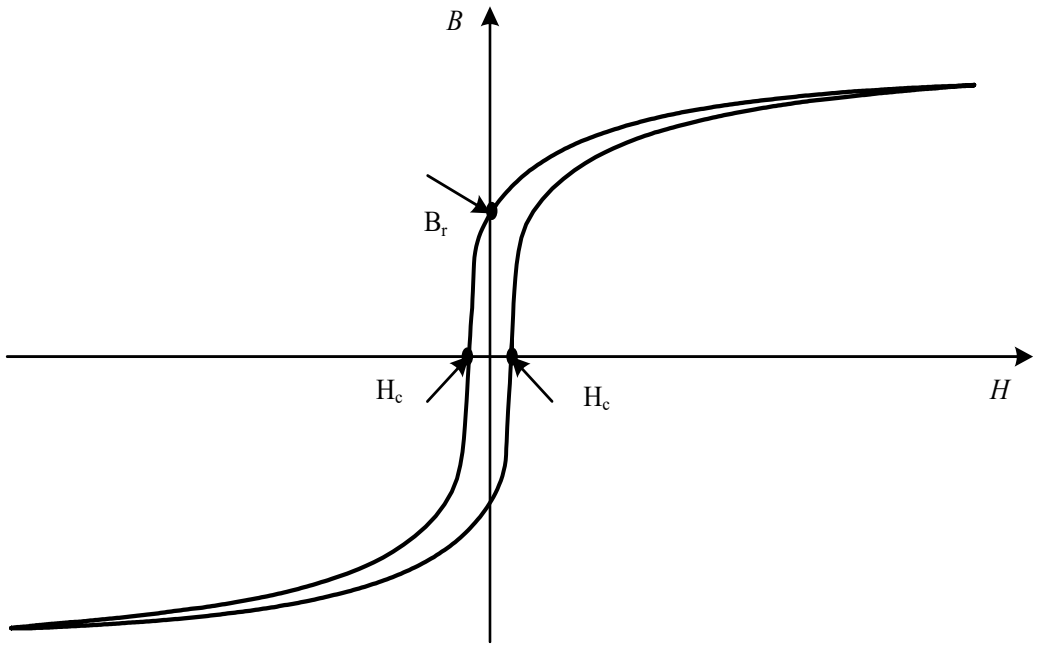

Fig. 2.1. The general pattern of *B-H* loop of a magnetic material.

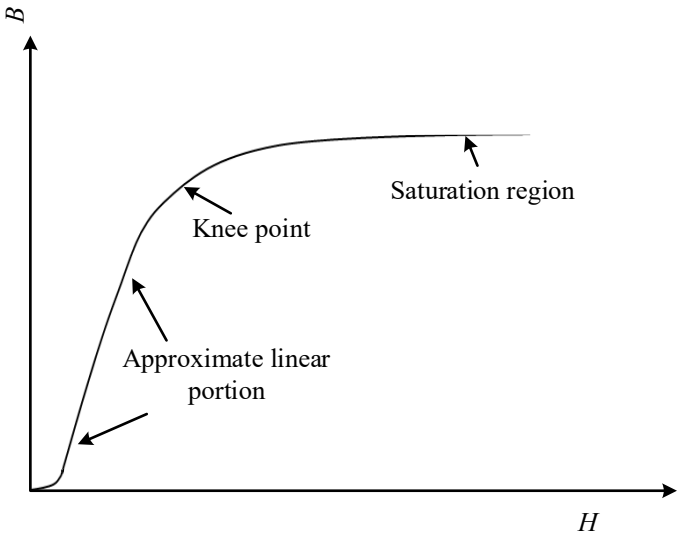

Fig. 2.2. A typical initial *B-H* magnetisation curve of a magnetic material.

According to the magnetic domain theory, magnetic materials are considered as a combination of small regions known as domains, and each domain consists of many

magnetic moments [2.2]. When a magnetomotive force is imposed on a magnetic material, the magnetic moments change their orientations in the region between domains [2.3]. This region is known as domain wall as shown in Fig. 2.3 [2.4]. The size of the domains also changes along with the orientations' changes. The change of orientations and sizes of the magnetic domains can be reversible and irreversible. In the reversible change, the magnetic moments return to their original state after removal of applied magnetic field. The magnetisation related to the reversible change is known as reversible magnetisation. On the other hand, the magnetisation related to the irreversible change is known as irreversible magnetisation. Both the reversible and irreversible magnetisation generally happen together. The magnetisation process [2.5] in a magnetic material starting from zero to saturation magnetic field is discussed below.

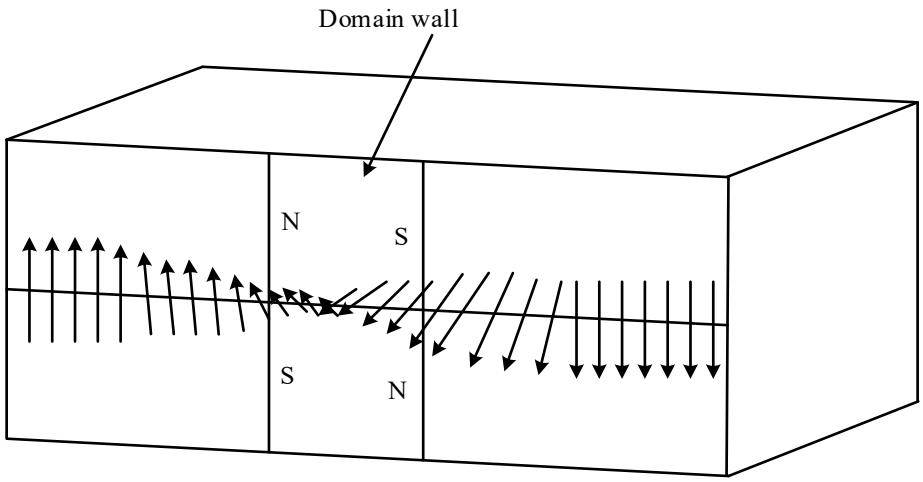

Fig. 2.3. Orientation change of magnetic moments at magnetic domain wall [2.4].

Firstly, a low external magnetic field is considered into a sample of magnetic material with demagnetised state. This external magnetic field produces domain wall movement and changes the domain sizes. In this case both the domain wall movement and domain size changes are mainly reversible, and the corresponding magnetisation becomes reversible. After increase of the magnetic field strength, the irreversible domain wall movement also occurs, and it increases with the magnetic field. In that case, the rapid change of domain direction occurs due to the overcome of barriers presented by pinning sites in the structure. In this case, the magnetisation increases almost linearly with increase of magnetic field strength as shown in Fig. 2.2. With further rise of the magnetic field, the magnetic domains with favoured directions become a single domain state, the

whole volume of the magnetic material comes under magnetisation. With more increase of external magnetic field, magnetisation vectors within individual domains rotate and they simultaneously come close to the direction of applied magnetic field. The resulting magnetisation is mainly irreversible as after removal of the external magnetic field, all magnetic vectors do not return back to their original axes. In this case, the magnetisation increases slowly with increase of magnetic field strength which is represented in the region of knee point of Fig. 2.2. At higher external magnetic field, the magnetisation vectors of individual domains become parallel to the direction of the external magnetic field which is reversible magnetisation. After that, further rise of applied magnetic field does not generate any increase of magnetisation [2.1]. This situation is called the magnetisation saturation. The details of magnetisation process according to Domain's theory can be obtained in [2.5].

2.2 Measurement and Modelling of Alternating Core Loss

2.2.1 Measurement of Alternating Core Loss

Magnetic core loss plays one of the vital roles in the design of electrical machines and transformers. The core loss, which mainly depends on the frequency, magnetic flux density and properties of the material, affects the efficiency and heat dissipation of the electrical devices [2.6]. Consequently, the accurate core loss measurement becomes significant in design of electrical machines and transformers. There are many core loss measurement techniques reported in the literature which can be generally classified into two groups: thermal or calorimeter technique, and electrical technique [2.7]–[2.10].

2.2.1.1 Thermal or Calorimeter Technique

In the thermal method, different types of coolants, e.g., water and air are used to absorb heat produced by core loss and winding loss. As a result, the temperature of the coolant increases due to the power loss dissipation in the device. The power loss can be obtained from the temperature difference and flow rate of coolant. In [2.7], the authors used a calorimeter to measure the core loss. A core under test (CUT) is placed inside the vessel, where FC-40 is used as coolant which flows at a constant rate with a pump and control valve, as shown in Fig. 2.4. Under steady state condition, the final temperature difference is measured. Finally, the total dissipated power is calculated by [2.7]

$$P = \rho A V C_s \Delta T \tag{2.1}$$

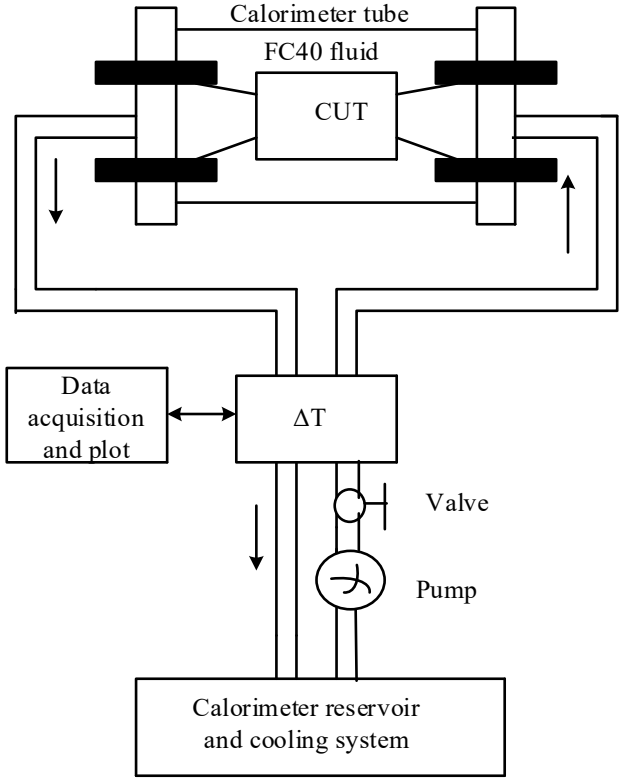

Fig. 2.4. The block diagram of a core loss measurement system using calorimeter [2.7].

where ρ is the mass density of the coolant, V the flow rate of the coolant, C_s the specific heat of fluid, and A the cross-sectional area of coolant path. To reduce the loss due to the convection and radiation, the authors of [2.8] proposed an improved calorimeter technique to measure the core loss, where the CUT is placed inside a vacuum chamber, and the test is done under isothermal conditions. The thermal methods have some common disadvantages, e.g., time consuming, difficulty of separating winding loss from core loss, high error in case of low core loss and difficulty of making test platform [2.9].

2.2.1.2 Electrical Technique

The disadvantages of thermal techniques can be eliminated by using the electrical techniques. The electrical techniques are classified into two groups: impedance technique and wattmeter technique. In impedance techniques, the core loss is considered as an equivalent loss resistance, which may be associated with parallel or series with the

magnetising inductance. The Maxwell-Wien Bridge and network analyser are generally utilised in this approach to measure the core loss. The wattmeter technique is the mostly used technique to measure the core loss of magnetic materials where two windings are wound around a core used for experiment as shown in Fig. 2.5. Instead of traditional wattmeter, oscilloscopes are commonly exploited to measure core loss especially for non-sinusoidal excitation [2.10]. A signal generator is generally used as excitation source. The excitation current and secondary open circuit voltage are used for calculation of core loss by the following equation [2.10]:

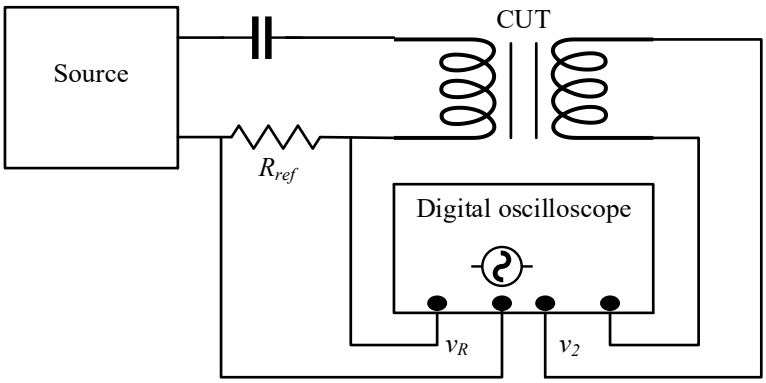

Fig. 2.5. Schematic diagram of core loss measurement using oscilloscope [2.11].

$$P = \frac{1}{T}\int i_p(t)v_s(t)dt \tag{2.2}$$

where i_p indicates the excitation current in the primary winding and v_s indicates induced voltage in the secondary winding. Authors of [2.12] used digital signal processing for data accusations instead of oscilloscope. Instead of signal generator as source, and oscilloscope for data accusations, LabVIEW was used for both source and output measurements in [2.13]. However, in the above-mentioned methods, DC bias in magnetisation current is not included during the core loss measurement set up. The experimental set up for core loss measurement with DC bias is shown in Fig. 2.6. A digital oscilloscope is exploited to sample the excitation current and voltage. Finally, the core loss is calculated from sampled data by using the following equation [2.14]:

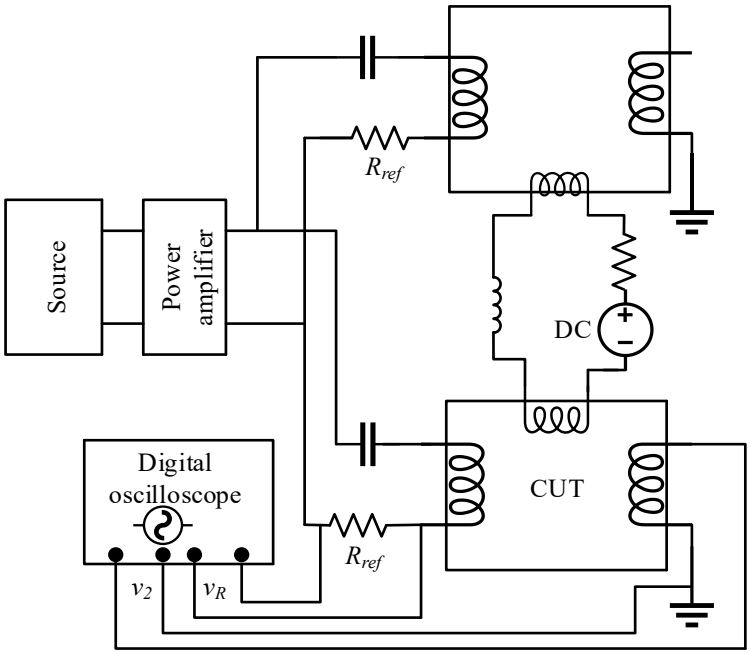

Fig. 2.6. Schematic diagram of core loss measurement with DC bias [2.14].

$$P = \frac{N_p}{N_s}\frac{1}{N_t}\sum_{i=1}^{N_t} v_s \frac{v_R}{R_{ref}} \tag{2.3}$$

where N_p and N_s are the numbers of turns in primary and secondary windings, respectively, R_{ref} the resistance of current sensor, v_R the voltage across the current sensor resistor, and N_t the number of samples per period. To decrease the effect of phase discrepancy which exists in abovementioned methods, a resonant capacitor or ideal inductor is connected in series with excitation winding [2.11], [2.15], [2.16]. In these approaches, the sum of voltage of secondary winding, and capacitor or inductor voltage is closely equal to the voltage due to core loss. Consequently, the effect of phase discrepancy decreases. Fig. 2.7 shows core loss measurement using capacitive cancellation where a capacitor is connected with windings. The value of the capacitor (C_r) is given by [2.15]

$$C_r = \frac{N_p}{N_s (2\pi f)^2 L_m} \tag{2.4}$$

where L_m is the magnetising inductance of the winding.

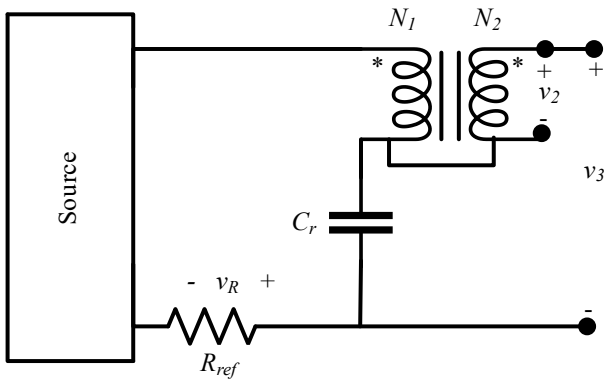

Fig. 2.7. Core loss measurement using capacitive cancellation [2.15].

2.2.2 Modelling of Alternating (1-D) Core Loss

For design of electrical machines and transformers, one of the main challenges is to predict the core loss accurately. Several models in the literature have been proposed to predict the core loss in the last few decades. These models can be grouped into two approaches: empirical based models and microstructures-based models. Both models are deliberated in the following subsections.

2.2.2.1 Empirical Core Loss Model

Empirical core loss model can be divided into two groups: loss separation model and Steinmetz based model. In the first model, the core loss is divided into three parts: hysteresis loss, eddy current loss and the anomalous or excess loss [2.17]. Authors of [2.18] proposed a loss separation model for sinusoidal excitation which is given by

$$P = K_h B_m^{aB_m^2+bB_m+c} f + K_e B_m^2 f^2 + 8.76 K_{exc} B_m^{1.5} f^{1.5} \tag{2.5}$$

where f is the frequency, B_m is the maximum magnetic flux density, and K_h, K_e, K_{exc}, a, b, and c are the constant coefficients. The measurements for determining the coefficients of (2.5) are extensive which makes the method impractical for designers. In contrast, the Steinmetz equation based empirical methods [2.19]−[2.22] are more practical and straightforward to predict the core losses. The expression of original Steinmetz equation (OSE) is given below [2.19], [2.22].

$$P = kf^{\alpha} B_m^{\beta} \tag{2.6}$$

where k, α and β are the Steinmetz parameters. The main downside of OSE is that the equation is effective for only sinusoidal excitation. However, in MFT topologies, the excitation voltage is non-sinusoidal. Therefore, many models have been proposed to predict the core loss for non-sinusoidal excitation. The OSE was modified by authors of [2.20] where, the core loss is also related to the rate of the change of magnetic flux density which is given by

$$P = k\, f_{eq}^{\alpha-1} B_m^{\beta} f_r \tag{2.7}$$

where f_r is the fundamental frequency and f_{eq} is given by

$$f_{eq} = \frac{2}{\Delta\beta^2 \pi^2} \int_0^T \left(\frac{dB}{dt} \right)^2 dt\,. \tag{2.8}$$

In [2.21], it is shown that core loss not only depends on the rate of the change of the magnetic flux density but also depends on its instantaneous value. Thus, the following generalised Steinmetz equation (GSE) was proposed for prediction of core loss [2.21]:

$$P = \frac{1}{T} \int_0^T k_i \left| \frac{dB(t)}{dt} \right|^{\alpha} \left| B(t) \right|^{\beta-\alpha} dt \tag{2.9}$$

where $k_i = \dfrac{k}{(2\pi)^{\alpha-1} \displaystyle\int_0^{2\pi} \left|\cos\theta\right|^{\alpha} \left|\sin\theta\right|^{\beta-\alpha} d\theta}$.

In [2.22], authors reported that the time history of magnetic material also affects the core loss. For that, the instantaneous value of magnetic flux density is substituted by the peak to peak value and the equation of the loss is given by [2.22]:

$$P = \frac{1}{T} \int_0^T k_i \left| \frac{dB(t)}{dt} \right|^{\alpha} \left| \Delta B \right|^{\beta-\alpha} dt \tag{2.10}$$

where $k_i = \dfrac{k}{(2\pi)^{\alpha-1}\int_0^{2\pi}\left|\cos\theta\right|^{\alpha}2^{\beta-\alpha}\,d\theta}$.

The author of [2.23] proposed another modified Steinmetz equation known as natural Steinmetz equation (NSE) to predict the core loss. The equation of NSE method is as follows [2.23]:

$$P=\left(\frac{\Delta B}{2}\right)^{\beta-\alpha}\frac{K_N}{T}\int_0^T\left|\frac{dB(t)}{dt}\right|^{\alpha}dt \tag{2.11}$$

where $k_N = \dfrac{k}{(2\pi)^{\alpha-1}\int_0^{2\pi}\left|\cos\theta\right|^{\alpha}d\theta}$.

The simplest way to predict the core loss for non-sinusoidal excitation with slight modification of Steinmetz equation was proposed in [2.24], known as waveform coefficient Steinmetz equation (WCSE). A factor (K_{FWC}), which is the ratio of areas of the non-sinusoidal and sinusoidal magnetisation waveforms, is just multiplied by the original Steinmetz equation. The waveform coefficient Steinmetz equation for any arbitrary excitation voltage is given by [2.24]

$$P = K_{FWC}k\,f^{\alpha}B_m^{\beta}. \tag{2.12}$$

2.2.2.2 Microstructures of the Material-Based Models

In microstructure-based models, the core loss is obtained from the waveforms of B and H, which is as follows:

$$P=\frac{1}{\rho T}\int_T H\frac{dB}{dt}dt \tag{2.13}$$

where P is core loss, T is time period, and ρ is mass density of the material. In this type of models, Jiles-Atherton (J-A) hysteresis model and Preisach model are generally utilised for predicting B from H. On the other hand, as the calculation of H from B is important in finite element analysis, inverse J-A and inverse Preisach models, which are

based on their original J-A and Preisach models respectively, are also utilised for core loss prediction.

2.2.2.2.1 Preisach Model

The magnetic material in Preisach model is considered as a set of magnetic dipoles [2.25], and each magnetic dipole is assumed as a rectangular elementary shape as shown in Fig. 2.8(a) where two switching magnetic field strengths, denoted by α and β, are considered in the increasing and decreasing magnetic trajectories, respectively. Fig. 2.8(b) shows the Preisach diagram, where S is the triangular region on the (α, β) plane for $H_{sat} \geq \alpha \geq \beta \geq -H_{sat}$, and S^+ and S^- are regions of positive and negative switched dipoles, respectively. If the applied magnetic field strength is H, the output magnetisation M, and the corresponding magnetic flux density B can be calculated by (2.14) and (2.15) [2.26], [2.27] as follows, respectively:

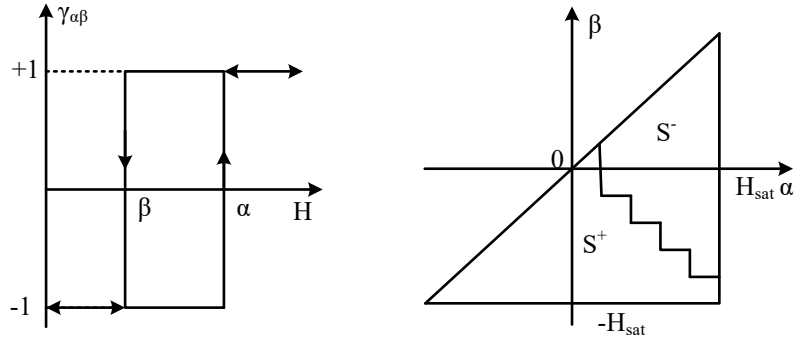

Fig. 2.8. (a) Rectangular hysteresis model of magnetic dipoles [2.28], and (b) Preisach diagram [2.28].

$$M(H) = \int_S \mu(\alpha, \beta)\gamma_{\alpha\beta}(H)\,d\alpha\,d\beta \tag{2.14}$$

$$B = \mu_0[H + M(H)] \tag{2.15}$$

where $\mu(\alpha, \beta)$ is the distribution function of the magnetic dipoles, $\gamma_{\alpha\beta}$ the Preisach operator which is 1 on S^+ and -1 on S^-, and S the triangular region on the (α, β) plane for $H_{sat} \geq \alpha \geq \beta \geq -H_{sat}$ as shown in Fig. 2.8(b). Using the Preisach diagram, the magnetisation is firstly calculated, and the magnetic flux density is then calculated from magnetisation and magnetic field strength.

The main challenge of the Preisach model is to find out the distribution function which is generally obtained from experimental data. For identification of the distribution function, the first order reversible curve or limiting loop are generally utilised. In addition, some analytical approximations such as power series approximation, Gaussian distribution and product models are also used for identification of Preisach model parameters. The normal Preisach model does not consider the internal interaction magnetisation which can be considered by introducing a feedback coefficient [2.29]–[2.34]. The Preisach model considering the magnetisation dependent Preisach distribution function is known as moving Preisach model. However, both the normal and moving Preisach models consider only the irreversible magnetisation component. The generalised Preisach model, on the other hand, takes into account both the irreversible and reversible magnetisation components, as well as the magnetisation dependent component with a feedback coefficient [2.35]–[2.37]. Thus, the generalised Preisach model provides better result than the normal and moving Preisach models.

The inverse Preisach model [2.38] can also be derived from the original normal Prisach model, where the magnetic field strength H can be obtained by

$$H\left(t+\Delta t\right)=H\left(t\right)+\frac{\Delta B}{dB/dH} \tag{2.16}$$

with

$$\frac{dB}{dH}=\mu_0+\mu_0\frac{dM}{dH} \tag{2.17}$$

where dM/dH can be calculated by performing the first derivative of (2.14) with respect to H. The details of the both Preisach and inverse Preisach models are also discussed in Chapter 3.

2.2.2.2.2 J-A Model

In J-A model [2.39], the magnetisation M is considered as the sum of irreversible M_{irr} and reversible magnetisation M_{rev} components, which is as follows:

$$M=M_{irr}+M_{rev} \tag{2.18}$$

where, M_{rev} is calculated from the anhystertic magnetisation M_{an} and irreversible magnetisation M_{irr}. According to J-A model, the equations related to the calculation of M_{rev}, and M_{irr}, for a given H are as follows:

$$M_{irr} = M_{an} - k\delta \frac{dM_{irr}}{dH_e} \tag{2.19}$$

$$M_{rev} = c\left(M_{an} - M_{irr}\right) \tag{2.20}$$

where k and c are the model parameters, M_{an} the anhysteretic magnetisation, H_e the effective magnetic field strength, and δ the directional parameter which is +1 for $dH/dt > 0$ and -1 for $dH/dt < 0$. The anhysteretic magnetisation and the effective magnetic field strength can be expressed as follows:

$$M_{an} = M_s \left[\coth \frac{H_e}{a} - \frac{a}{H_e} \right] \tag{2.21}$$

$$H_e = H + \alpha M \tag{2.22}$$

where M_s is the saturation magnetisation, M the total magnetisation, H the applied magnetic field strength, H_e the effective magnetic field strength, and a and α are the model parameters. In the J-A model, the magnetisation in the next time step is calculated from its present magnetisation and its derivative with respective to the magnetic field strength (dM/dH) [2.40]. According to the J-A model, dM/dH can be obtained as follows [2.39]:

$$\frac{dM}{dH} = \left(1-c\right)\frac{M_{an} - M_{irr}}{k\delta - \alpha\left(M_{an} - M_{irr}\right)} + c\frac{dM_{an}}{dH} \tag{2.23}$$

Using the above-mentioned expressions of M_{irr}, M_{rev}, M_{an}, and H_e, the total magnetisation susceptibility (dM/dH) can also be obtained by (2.24), which is expressed as follows [2.41]:

$$\frac{dM}{dH} = \frac{(1-\mathrm{c})\frac{dM_{irr}}{dH_e} + c\frac{dM_{an}}{dH_e}}{1-\alpha(1-\mathrm{c})\frac{dM_{irr}}{dH_e} - \alpha c\frac{dM_{an}}{dH_e}} \tag{2.24}$$

where dM_{irr}/dH_e and dM_{an}/dH_e can be obtained using (2.19) and (2.21), respectively. From (2.19), the dM_{irr}/dH_e can be written as:

$$\frac{dM_{irr}}{dH_e} = \frac{\left(M_{an} - M_{irr}\right)}{k\delta} \tag{2.25}$$

It was considered in [2.39] and [2.42] that domain wall displacement does not exist if $(M_{an} - M_{irr})dH_e < 0$, and in that case, dM_{irr}/dH_e becomes zero. Therefore, (2.25) can be updated as follows [2.42]−[2.44]:

$$\frac{dM_{irr}}{dH_e} = \frac{\delta_M \left(M_{an} - M_{irr}\right)}{k\delta} \tag{2.26}$$

where δ_M is 1 if $(M_{an} - M_{irr})dH_e > 0$, and 0 if $(M_{an} - M_{irr})dH_e \leq 0$.

However, it is reported in [2.45] and [2.46] that the pinning parameter (k) of the J-A model changes with the magnetic induction levels. Therefore, k is considered as the function of H in [2.45] and [2.46], which improves the accuracy of the model. It is also observed in [2.47]–[2.49] that at low magnetic induction levels, the high discrepancy in both the iron loss and B calculations is obtained. To reduce this discrepancy, a scaling factor is included in (2.25) so that it limits the rate of irreversible magnetisation at the low induction levels. According to [2.49], (2.25) can been modified as follows:

$$\frac{dM_{irr}}{dH_e} = \frac{\left(M_{an} - RM_{irr}\right)}{k\delta} \tag{2.27}$$

where R is the scaling factor which can be expressed by the magnetic field strength or magnetic flux density depending on the input of the J-A model. Recently, the authors of [2.50] considered both the pining coefficient k and scaling factor R as functions of

magnetic field strength for inner loops. Therefore, for inner loops especially at low magnetic induction levels, the relative error in the calculation of iron loss reduces.

Identification of the parameters is also important in the J-A model. Initially few equations corresponding to the model parameters are developed using model equations and a large *B-H* loop of a magnetic material [2.51], [2.39], [2.41]. Those equations are solved numerically to acquire the J-A model parameters. In the last few decades, different optimisation techniques were considered to obtain the J-A model parameters where an error criterion is generally set as an objective function [2.43], [2.46], [2.52], [2.53], [2.54]. An error criterion, which is based on the root mean square of the difference between measured and calculated magnetic flux density, is generally used in the optimisation methods that can be expressed as follows [2.45]:

$$\varepsilon_S = \sqrt{\sum_i^N \frac{\left(B_{meai} - B_{cali}\right)^2}{N}} \tag{2.28}$$

where ε_s is the root mean square of error, N the number of samples per period of the magnetic flux density, B_{meai} the measure magnetic flux density, and B_{cali} the calculated magnetic flux density. After calculating the model parameters, the iron loss of the corresponding magnetic core is calculated using (2.13).

In the inverse J-A model [2.40], the static magnetic field strength is calculated from the magnetic flux density. In the model, the M is firstly calculated, and H is then calculated from M and B, which are as follows

$$M\left(t+\Delta t\right) = M\left(t\right) + \frac{dM}{dB}\Delta B \tag{2.29}$$

$$H\left(t+\Delta t\right) = \frac{B\left(t+\Delta t\right)}{\mu_0} - M\left(t+\Delta t\right) \tag{2.30}$$

with

$$\frac{dM}{dB}=\frac{(1-c)\frac{dM_{irr}}{dB_e}+\frac{c}{\mu_0}\frac{dM_{an}}{dH_e}}{1+\mu_0(1-\alpha)(1-c)\frac{dM_{irr}}{dB_e}+c(1-\alpha)\frac{dM_{an}}{dH_e}} \tag{2.31}$$

$$\frac{dM_{irr}}{dB_e}=\frac{M_{an}(t)-M_{irr}(t)}{\mu_0 k\delta} \tag{2.32}$$

$$\frac{dM_{an}}{dH_e}=\frac{M_s}{a}\left\{1-\coth^2\frac{H_e}{a}+\left(\frac{a}{H_e}\right)^2\right\} \tag{2.33}$$

where B_e is the effective magnetic flux density.

The above-mentioned J-A and Preisach models are generally used for static hysteresis loss modelling. With the increase of the frequency, the dynamic losses such as eddy current and excess losses are also responsible for core loss. The loss separation method is generally used for modelling total core loss. The incorporation of eddy current and excess losses into the Preisach and J-A models are discussed in Chapters 3 and 4, respectively.

2.3 Measurement of 2-D Core Loss

As the 1-D measurement system considers only alternating magnetic field, the method cannot be used to characterise the magnetic core under the rotating magnetic field. Two-dimensional (2-D) measurement methods are generally utilised for estimation of the core losses in the presence of the rotating magnetic field. The pattern of the rotational hysteresis loss is quite different from that of alternating hysteresis loss. The typical patterns of rotational and conventional alternating hysteresis losses of a magnetic material are shown in Figs. 2.9 and 2.10, respectively. Alternating hysteresis loss always increases with the magnetic flux density whereas the rotational hysteresis loss near to the saturation region decreases and even becomes zero at saturation magnetic flux density. However, in the presence of the rotating magnetic field, a torque is induced in the magnetic material which can be written as follows [2.37]:

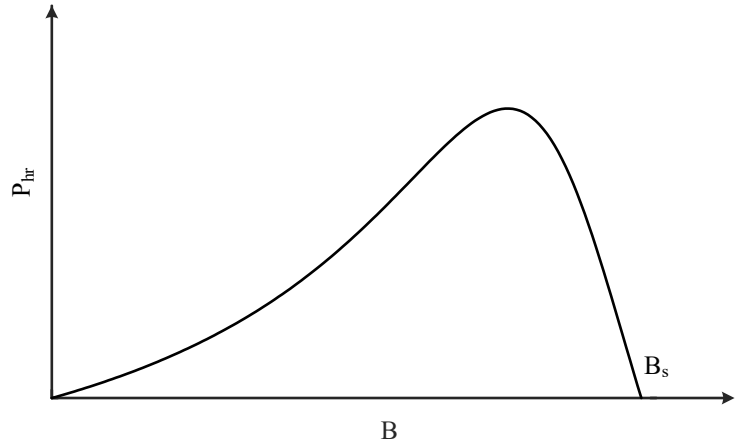

Fig. 2.9. The typical pattern of the rotational hysteresis loss of a magnetic material [2.37].

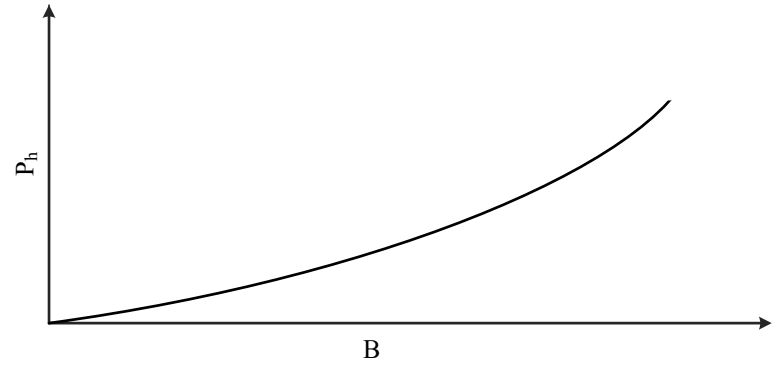

Fig. 2.10. The typical pattern of the alternating hysteresis loss of a magnetic material.

$$T_r = \mu_0 \left|\mathbf{M} \times \mathbf{H}\right| = \mu_0 MH \sin\delta \tag{2.34}$$

where T_r is the torque, and **M** and **H** are the magnetisation vector and magnetic field strength vector, δ is the angle between **M** and **H**, and M and H are the magnitudes of **M** and **H** vectors, respectively. For circular rotation of magnetic field, the angular speed of the magnetic flux density vector at a fixed frequency is constant, and then the hysteresis rotational loss directly depends on the average induced torque in the magnetic material.

With the low applied magnetic field, the magnetisation is generated due to the change of orientation and size of the magnetic domain as similar to the alternating magnetisation. Consequently, domain wall movement occurs due to the applied magnetics field strength. Moreover, due to the pinning of domain walls by defect sites in magnetic material, there exists an opposite force which resists the change of magnetisation which is indicated by the angle between **M** and **H** as shown in Fig. 2.11 [2.37]. In the medium magnetic field strength, the annihilation and recreation of magnetic domain walls occur, which increases

the rotational hysteresis loss as extra energy is required for annihilation and recreation of magnetic domain wall. In this region, smaller magnetic domains convert into large magnetic domain. At the point near the saturation region, there exists only few large magnetic domains, and consequently the opposite force reduces and the angle between **M** and **H** also reduces. At highly saturated magnetisation, there exist only one large domain and the opposite force becomes almost zero, and the corresponding δ becomes zero, as shown in Fig. 2.12 [2.37]. Thus, the hysteresis loss will be zero in that case.

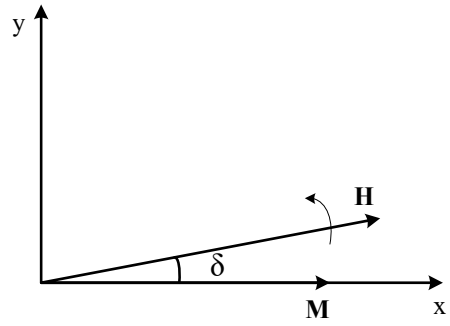

Fig. 2.11. Induced torque angle due to the rotational magnetic field at general magnetic flux density [2.37].

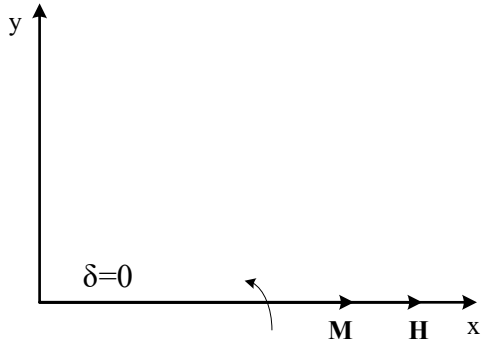

Fig. 2.12. Induced torque angle due to the rotational magnetic field at saturation magnetic flux density [2.37].

In [2.55], the rotational loss was calculated from measured induced torque in the specimen. In the last hundred years, different rotational core loss measurement methods such as thermometric method, field-metric method, and watt-metric method were developed [2.55]−[2.61]. The field metric technique is generally used to measure the core loss as the magnetic field in the specimen can be easily controlled by a feedback system.

In this method, the **B** and **H** are firstly calculated, and the core loss is then calculated from **B** and **H** which is as follows [2.37].

$$P_t = \frac{1}{T\rho}\int_0^T \left(H_x \frac{dB_x}{dt} + H_y \frac{dB_y}{dt} \right) dt \tag{2.35}$$

where P_t is the total rotating core loss, H_x and H_y are the components of **H** in their corresponding directions, and B_x and B_y are the components of **B** in their corresponding directions.

2.3.1 Calculation of H Components

The conventional **H**-sensing method, as shown in Fig. 2.13, is generally used to detect the **H** components. In this method, two search coils are placed very close to the specimen, and the voltages induced across the coils are measured. The **H** components are then calculated from the measured voltages which is given below [2.37]:

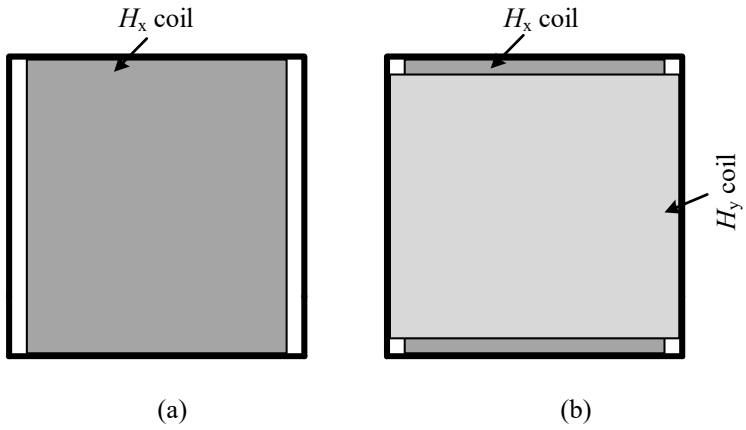

Fig. 2.13. (a) **H** coil in one dimensional configuration and (b) **H** coils in two-dimensional configuration [2.37].

$$H_i = \frac{1}{\mu_0 \mathrm{K_{Hi}}} \int v_{Hi} dt \qquad i = x, y \tag{2.36}$$

where $\mathrm{K_{Hi}}$ indicates coefficients calculated by calibration of the coils [2.37] and μ_0 indicates the permeability of air. The coils are wound either separately on a thin structure,

as shown in Fig. 2.13 (a), or wound in the same structure with opposite direction, as shown in Fig. 2.13 (b).

Two coils arrangement [2.62] for each search coil, as shown in Fig. 2.14, is also used to find high accuracy value of **H** components. The component of **H** is then calculated by

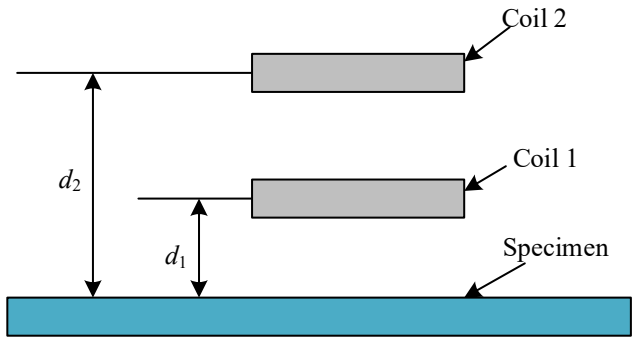

Fig. 2.14. The arrangement of two coil method for measurement of **H** components [2.62].

$$H = \frac{d_2 H_1 - d_1 H_2}{d_2 - d_1} \tag{2.37}$$

where d_1 and d_2 indicate distances of the coils from the specimen as shown in Fig. 2.14, and H_1 and H_2 indicate magnetic field strengths of coil 1 and coil 2, respectively.

The Hall element is also used to measure the **H** [2.63]. A Hall element is a semiconductor plate where constant current passes through two ends as shown in Fig 2.15. A voltage induced in the opposite edges of the plate is measured, and the magnetic field strength can be then calculated as follows:

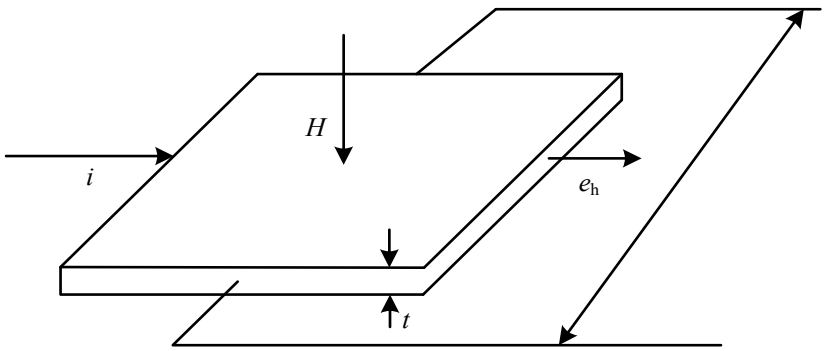

Fig. 2.15. A typical Hall element which uses the Hall effect [2.37].

$$H = \frac{e_h t_h}{R_h i} \tag{2.38}$$

where e_h is the induced voltage, t_h the thickness of the plate, R_h Hall constant of the plate, and i the current flowing through the plate.

2.3.2 Calculation of B Components

The search coils are used for measuring the components of the **B**. For uniform **B** in the specimen, the search coils are wound over the specimen, as shown in Fig. 2.16 (a). On the other hand, for non-uniform **B**, the search coils are wound at the middle of the specimen as shown in Fig. 2.16 (b), because the magnetic flux density in the middle region is generally considered as uniform. The components of **B** are then calculated from voltage induced in the coils under the rotating magnetic field which are as follows [2.37]:

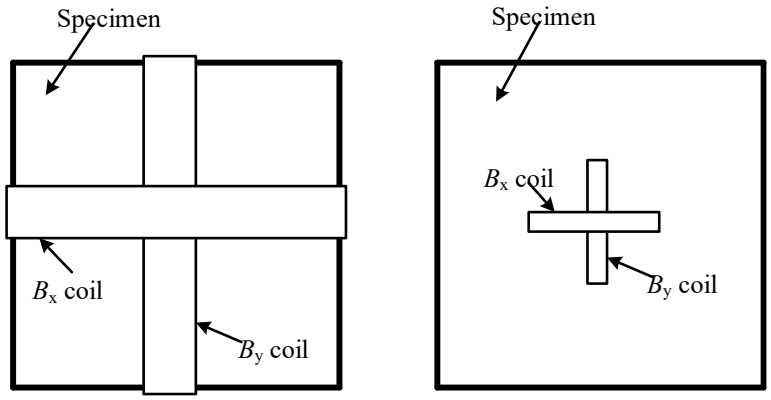

Fig. 2.16. Searching coil arrangement for (a) uniform **B**, and (b) nonuniform **B** [2.37].

$$B_i = \frac{1}{\mathrm{K_{Bi}}} \int v_{Bi} dt \qquad i = x, y \tag{2.39}$$

where $K_{Bi}=N_{Bi}A_{ci}$ are the coefficients of **B**-sensors, N_{Bi} are the number of turns in the sensing coils, and v_{Bi} are the induced voltage on sensing coils and A_{ci} cross-sectional area of the specimen.

In [2.64] and [2.65], another method for measurement of **B** was reported where two needles of voltage measurement devices are placed at the two points of the specimen as shown in Fig. 2.17. The induced voltage between two points is measured, and the components of **B** are then calculated from the measured voltages.

$$B_i = \frac{2}{bd}\int v_{Bi}dt \qquad i = x, y \tag{2.40}$$

where b indicates distance between two points and d indicates the thickness of the specimen.

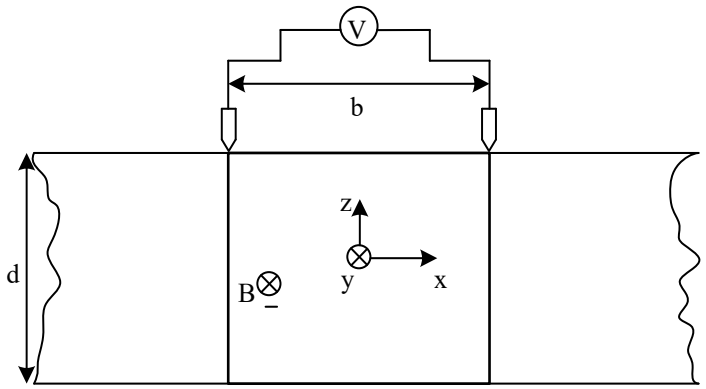

Fig. 2.17. Measurement of **B** component using B tips [2.65].

2.3.3 Apparatuses of 2-D Measurement System

Depending on the variation of the sample structures such as disk type sample, cross and strip sample, square sample, and large sheet sample, different types of testing devices were proposed by different researchers for measuring the 2-D core loss [2.56], [2.57], [2.59], [2.66]−[2.74]. Some of the testers are discussed in this subsection.

At the preliminary stage of the 2-D measurement system, disk samples were utilised for investigation of the magnetic properties. The testing system was developed by Brailsford in 1938 [2.59]. Torque-metric method was used for measuring the rotational losses. Depending on the rotational direction of the applied magnetic field, the disk sample could rotate in both clockwise and anticlockwise directions. Fixed disk sample-based testing device was later developed by Fiorillo and Reitto [2.67]. In this case, both thermo-metric

and field-metric methods can be used for measuring the loss. The demerits of the disk sample-based testing system are that the induced **B** in the sample is not uniform, and the feedback system cannot be utilised.

The above-mentioned problems of disk sample tester can be reduced by cross sample-based testing device which was reported in [2.56]. In the cross-sample based testing device, a feedback system is utilised to decrease the nonlinear effect of magnetic material. The core loss in this case is measured by the field-metric method. Later, the cross sample-based testing system was fully computerised, which was developed by Brix, Hempel, and Schroeder [2.69].

Square sample-based tester produces more uniform magnetic field in the specimen than the disk and cross sample-based testers. The square sample-based tester was first developed by Brix, Hempel, and Schulte [2.65]. In this system, field-metric method is exploited to measure the **H** and **B** as well as the rotational loss. Later, different square sample-based testers were reported by different researchers [2.70]−[2.72]. The block diagram of a square sample tester is shown in Fig. 2.18. The tester consists of two set of coils, where one set is for one axis and each set has two coils connected in series. The magnetic material sample with **B** and **H** sensors is placed in the middle of the tester as shown in Fig. 2.18. An analog feedback system is also utilised in the testing system to control the shape of the output voltage.

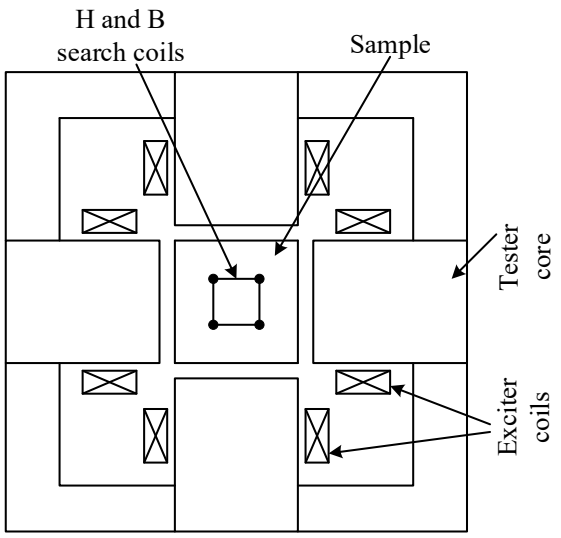

Fig. 2.18. Block diagram of a square specimen tester [2.73].

Another testing device based on the large sheet sample, as shown in Fig. 2.19, was reported in [2.57], [2.74]. The field-metric and watt-metric methods are used in this tester. The main problem of the tester is that **B** cannot reach up to the saturation magnetic flux density due to the high leakage and stray magnetic fluxes.

The modellings of rotational core loss under both circular and elliptical rotating magnetic field are discussed in Chapter 5.

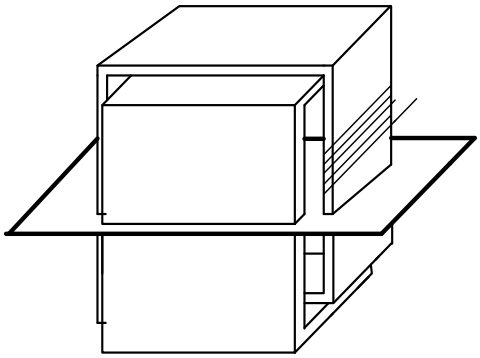

Fig. 2.19. Large sheet sample-based tester for rotational core loss measurement [2.57].

2.4 Design of the MFT

Recently solid-state transformers (SST) are getting attentions in the field of power electronics, where MFTs and HFTs are generally utilised in order to achieve high power density. The optimal design processes are generally used to design the MFTs and HFTs. In the optimisation techniques, core geometry and number of turns, B_m, and current density are generally considered as design variables. In addition, the researchers have also counted unusual design constraints such as the ripple voltages [2.75], the isolation requirement [2.76]−[2.78], thermal models [2.79], type of heuristic optimisation technique [2.80], Litz wire modelling for leakage inductance [2.81], [2.82] and winding loss modelling [2.83]. The design of MFT incorporates the modellings of core loss of the magnetic material, AC resistance and leakage inductances of the windings, and temperature rise. For the prediction of core loss, the empirical models, which has been already discussed in this chapter, are generally used in the MFTs' design processes due to its simplicity. The modellings of AC resistance and leakage inductances of the windings, and temperature rise are discussed below.

2.4.1 Winding AC Resistance Modelling

Winding loss or copper loss depends on the resistance of the winding wires, and affects the performance of a transformer. On the other hand, the AC resistance of a winding increases with the increase of the excitation frequency, as shown in Fig. 2.20. Thus, the increase of operating frequency also affects the winding loss.

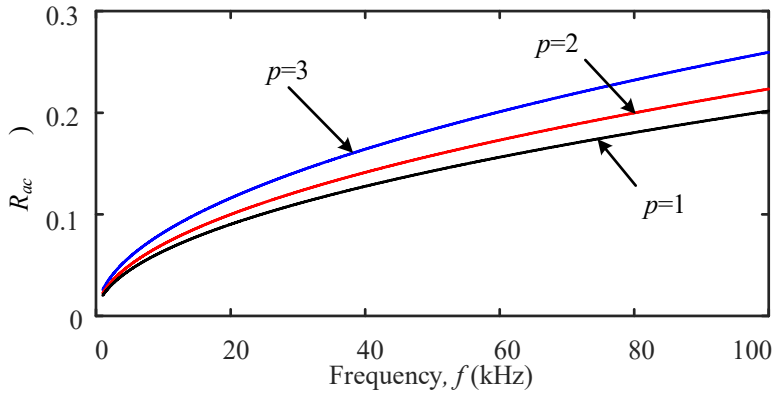

Fig. 2.20. Typical pattern of R_{ac} for different layers (p) with frequency.

Due to the skin and proximity effects, the distribution of the current across the cross section of a conductor is not uniform. This non-uniform current distribution makes a difference in the values of AC resistance from DC value. One dimensional Maxwell's equation is firstly utilised to derive the expression of leakage impedance in [2.84]. In [2.84], the round conductor is converted into rectangular shape to make the mathematics more manageable, as shown in Fig. 2.21. Dowell's expression of leakage resistance is then given by (2.41) [2.84]

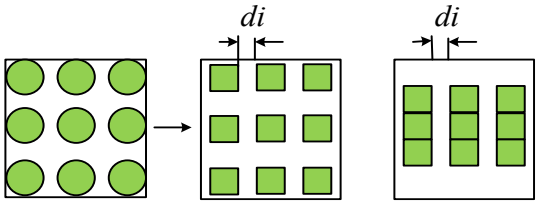

Fig. 2.21. Conversion of solid conductor from round shape to rectangular shape.

$$R_{ac} = \frac{p\rho_r N_l^2 l_t}{\eta d_t h_w}\left\{M'_w + \frac{(p^2-1)D'_w}{3}\right\} \tag{2.41}$$

where h_w is the winding breadth, ρ_r resistivity, η porosity factor, p the number of layers, N_l number of turns per layer, l_w mean turn length, d_t height of conductor, M'_w and D'_w are the real parts of M_w and D_w, respectively, which are as follows [2.84]:

$$M_w = \alpha_1 d_t \coth(\alpha_1 d_t),\ D_w = 2\alpha_1 d_t \tanh(\alpha_1 d_t / 2),\ \ \alpha_1 = \sqrt{\frac{j\omega\eta\mu_0}{\rho_r}} \tag{2.42}$$

where ω is angular frequency and μ is the permeability of the conductor. The above-mentioned AC resistance can also be expressed by the following equation [2.85]:

$$R_{ac} = R_{dc}\Delta\left[\frac{\sinh 2\Delta + \sin 2\Delta}{\cosh 2\Delta - \cos 2\Delta} + \frac{2(p^2-1)}{3}\frac{\sinh \Delta - \sin \Delta}{\cosh \Delta + \cos \Delta}\right] \tag{2.43}$$

where R_{dc} is the DC resistance of the winding, Δ is the ratio of thickness of conductor and skin depth, and p is the number of layers. The aforementioned Dowell's expression is derived using rectangular coordinates. In [2.86], cylindrical coordinates are used to derive the expression of AC resistance due to the winding's curvature on the transformers.

The Dowell's expressions of AC resistance have also some shortcomings, e.g., the effect of magnetising current is not considered and round conductor is replaced by square conductor. These shortcomings, especially second one, can be reduced by more accurate analytical methods reported in [2.87]. Accordingly, the AC resistance of a solid round conductor is given by, [2.87], [2.88]

$$R_{ac} = R_{dc}\frac{\gamma}{2}\left[\frac{ber\,\gamma\, bei'\gamma - bei\ \gamma\, ber'\gamma}{ber'^2\,\gamma + bei'^2\,\gamma} - 2\pi(2p-1)^2\frac{ber_2\,\gamma\, ber'\gamma + bei_2\,\gamma\, bei'\gamma}{ber^2\,\gamma + bei^2\,\gamma}\right] \tag{2.44}$$

where $\gamma = d_c / (\sqrt{2}\delta)$, d_c is the diameter of conductor, and δ the skin depth. In the above-mentioned methods, it is assumed that the magnetic field across the cross section of the conductor is uniform. This consideration is eliminated in [2.89], and a new expression of AC resistance is developed which is given as follows:

$$R_{ac} = R_{dc}\frac{\gamma}{2}\left[\frac{ber\,\gamma\, bei'\gamma - bei\ \gamma\, ber'\gamma}{ber'^{2}\,\gamma + bei'^{2}\,\gamma} - 2\pi\eta^{2}\left(4\frac{p^{2}-1}{3}+1\right)\frac{ber_{2}\,\gamma\, ber'\gamma - bei_{2}\,\gamma\, bei'\gamma}{ber^{2}\,\gamma + bei^{2}\,\gamma}\right] \tag{2.45}$$

Equations (2.41)− 2.45) are derived for only sinusoidal excitation. For non-sinusoidal excitation, Fourier series expansion can be utilised for determining the AC resistance. The main problem of the approach is that the method needs the determination of Fourier coefficients. The authors of [2.85] proposed a method to derive the expression of AC resistance without calculating the Fourier coefficients. The expression for AC resistance is given by [2.85]

$$R_{ac} = R_{dc}\left[1+\frac{5p^{2}-1}{45}\Delta^{4}\left(\frac{I'_{rms}}{\omega I_{rms}}\right)^{2}\right] \tag{2.46}$$

where I_{rms} is the root mean square value of current and I'_{rms} is the derivative of I_{rms}.

The above-mentioned expressions of AC resistances are used for a foil or round solid conductor. Presently, Litz wire is generally utilised to decrease the effect of eddy current and proximity effect. Litz wire consists of many strand conductors in which the diameter of each is so small that, eddy current effects decrease significantly. To model the Litz wire, the strand conductors in a wire are considered as an arrangement of $\sqrt{N_s}\times\sqrt{N_s}$, where N_s is the number of strands [2.90]. After that, the round conductor is transformed to corresponding rectangular conductor, as shown in Fig. 2.22. Next, the Dowell's expression is applied to obtain the AC resistance factor. The expression of Litz wire of a winding is given below [2.90]:

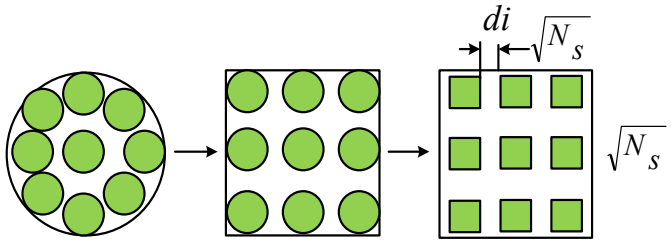

Fig. 2.22. Conversion method of a Litz wire to several layers for calculation of AC resistance [2.90].

$$R_{ac} = R_{dc}\Delta_s \left[\frac{\sinh 2\Delta_s + \sin 2\Delta_s}{\cosh 2\Delta_s - \cos 2\Delta_s} + \frac{2(N_s p^2 - 1)}{3} \frac{\sinh \Delta_s - \sin \Delta_s}{\cosh \Delta_s + \cos \Delta_s} \right] \tag{2.47}$$

where $\Delta_s = \frac{d_s}{2\delta}\sqrt{\frac{\pi d_s \sqrt{\pi N_s}}{2D_L}}$, and d_s is the diameter of a strand and D_L is the diameter of the Litz wire.

2.4.2 Leakage Inductance Modelling

Leakage inductance is another parasitic element of MFT, which also affects the performance of MFT. Similar to the AC resistance, the leakage inductance in high frequency differs from its static value, and changes with the frequency due to eddy current and proximity effects, as shown in Fig. 2.23. The analytical expressing of leakage inductance of a winding was obtained from the Dowell's expression which is as follows [2.84]:

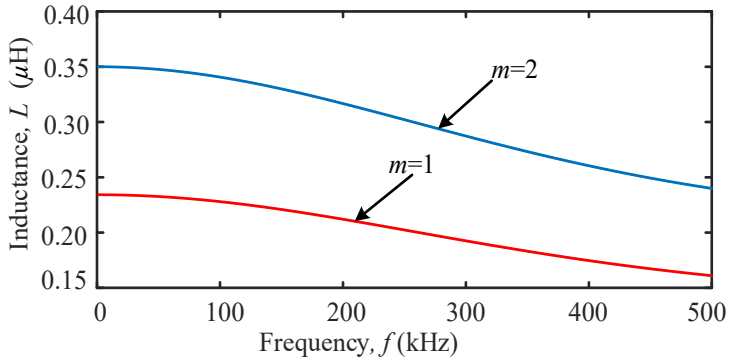

Fig. 2.23. Typical leakage inductance with frequency for turn ratios (m) 1 and 2.

$$L = \frac{\mu_0 p^3 N_l^2 d_t l_w}{3h_w} \left[\frac{3M_w'' + (p^2 - 1)D_w''}{p^2 \left| \alpha_1^2 d_t^2 \right|} \right] \tag{2.48}$$

where M_w'' and D_w'' are the imaginary parts of M_w and D_w, respectively. In [2.84], the total leakage inductance is obtained from the stored magnetic energy. The simplified equation of the total leakage inductance with considering one turn per layer and equal conductor thickness in the windings is obtained from the sum of all stored magnetic energies which is given below [2.91]:

$$L_{lk} = \frac{\mu_0 l_t n_p}{6h_{win}} \left[\frac{n_p^2 (k_1 + 2k_2)(m+1)}{\gamma \sinh^2(\gamma t_p)} + \frac{(k_1 - 4k_2)(m+1)}{2n\gamma \sinh^2(\gamma t_p)} + \left\{ 2n_p^2 + 2mn_p^2 + \frac{1}{m} + 1 \right\} t_{iso} \right] \quad (2.49)$$

where, $k_1 = \sinh(2\gamma t_p) - 2\gamma t_p$, $k_2 = \gamma t_p \cosh(\gamma t_p) - \sinh(\gamma t_p)$, n_p is the number of layers in the primary winding, m the turn ratio, t_p the primary conductor thickness, t_{iso} insulation thickness and h_{win} core window height.

2.4.3 Temperature Rise

The temperature rise is one of the major constraints in the MFT design process. Since the whole power losses are dissipated as heat, the temperature of the transformer rises which affects the performance and safety of the device. The amount of increased temperature due to the total loss is obtained by the following equation [2.92]:

$$\Delta T = P_T R_{th} \quad (2.50)$$

where ΔT is the temperature rise, R_{th} the thermal resistance, and P_T the transformer total loss. Compared to the theoretical methods, empirical models are simple and easy to incorporate into the MFT design. Moreover, empirical models may provide almost the same accuracy as the theoretical models. In [2.92], it is reported the following empirical expression to predict R_{th},

$$R_{th} \approx \frac{0.0457}{\sqrt{V_c}} \quad (2.51)$$

where V_c is the volume of the core. Another temperature rise empirical model is used in the design of the MFT which is as follows [2.93]:

$$\Delta T = 450 \left(\frac{P_T}{K_{st} (A_c A_w)^{0.5}} \right)^{0.826} \quad (2.52)$$

where P_T is the total loss in W, K_{st} a constant related to the structure of the core, and A_c and A_w are the cross-sectional areas of core and core-window, respectively. Since one of the MFT design constraints is the thermal limit, the transformer must operate below the

maximum permissible temperature rise, i.e., $P_{total}\ R_{th} \leq \Delta T_{max}$, where ΔT_{max} is the maximum permissible temperature rise.

2.5 Conclusion

In the above-mentioned discussion, it can be concluded that the magnetisation processes in a magnetic material under alternating and rotating magnetic fields are quite different, and the corresponding measurement methods and modellings of core loss are also different. In this study, electrical method is used for measurements of core loss, and the corresponding B and H, under alternating magnetic field excitation. For modelling the alternating magnetic properties, three common models such as empirical, Preisach and J-A model are exploited to model the selected magnetic material. On the other hand, the square specimen tester is selected to measure the vectorial magnetic properties of the selected magnetic material under 2-D rotational magnetic field excitation. From the literature, it is observed that the design of an MFT is associated with various mathematical expressions of different parameters, and an optimization technique is then exploited to obtain the required design specifications using those expressions. In the subsequent chapters of this thesis, measurement and modellings of magnetic properties of the selected amorphous magnetic material under alternating and 2-D rotating magnetic field excitations, and optimal design of an MFT are presented.

References

[2.1] S. Zurek, Two-dimensional magnetization problems in electrical steels, *PhD Dissertation*, Cardiff School of Engineering, Cardiff University, Wales, United Kingdom, March 2005.

[2.2] D. Jiles, Introduction to magnetism and Magnetic Materials, Chapman & Hall, London, UK, 1991.

[2.3] B. Zhu, Non-linear, irreversible magnetization processes in magnetic materials: instrumentation, measurements, modeling and application, PhD Dissertation, Electrical engineering, Iowa State University, Iowa, USA, 2001.

[2.4] C. Kittel, "Physical theory of ferromagnetic domains," *Rev. Mod. Phys*., vol. 21, no. 4, pp. 541-583, Oct. 1949.

[2.5] F. Brailsford, Magnetic materials, Methuen & Co. Ltd., London, UK, 1954.

[2.6] Y. Azzouz, A. Mouillet, and F. Z. Rebbani, "Measuring iron loss with a no-load torque rotating field device," *IEEE Trans. Magn*., vol. 43, no. 11, pp. 3999–4003, Nov. 2007.

[2.7] D. K. Conroy, G. F. Pierce, and P. R. Troyk, "Measurement techniques for the design of high-frequency SMPS transformer," *in Proc. 3rd Annu. Meeting Appl. Power Electron. Conf. Expo.*, New Orleans, LA, USA, Feb. 1–5, 1988, pp. 341–351.

[2.8] R. Linkous, A. W. Kelley, and K. C. Armstrong, "An improved calorimeter for measuring the core loss of magnetic materials," *in Proc. 15th Annu. IEEE Applied Power Electron. Conf. Exp.*, New Orleans, LA, Feb. 6–10, 2000, vol. 2, pp. 633–639.

[2.9] M. Mu, "High frequency magnetic core loss study," *PhD Thesis Dissertation*, Virginia Polytechnic Institute and State University, USA, 2013.

[2.10] Y. Han and Y. F. Liu, "A practical transformer core loss measurement scheme for high-frequency power converter," *IEEE Trans. Ind. Electron.*, vol. 55, no. 2, pp. 941–948, Feb. 2008.

[2.11] M. Mu, F. C. Lee, Q. Li, D. Gilham, and K. D. T. Ngo, "A high frequency core loss measurement method for arbitrary excitations," *in Proc. IEEE 26th Annu. Appl. Power Electron. Conf. Expo*., Fort Worth, TX, pp. 157–162, Mar. 6–11, 2011.

[2.12] S. Y. R. Hui, J. G. Zhu, and V. S. Ramsden, "A generalized dynamic circuit model of magnetic cores for low- and high-frequency applications. II. Circuit model formulation and implementation," *IEEE Trans. Power Electron.*, vol. 11, no. 2, pp. 251–259, Mar. 1996.

[2.13] P. Kis, M. Kuczmann, J. Fuzi, and A. Ivanyi, "Hysteresis measurement in LabView," *Pysica B: Cond. Matt.*, vol. 343, no. 1–4, pp. 357–363, Jan. 2004.

[2.14] Y. Han, W. Eberle, and Y. F. Liu, "New measurement methods to characterize transformer core loss and copper loss in high frequency switching mode power supplies," *in Proc. IEEE 35th Annu. Power Electron. Spec. Conf.*, Aachen, Germany, vol.2, pp. 1695–1701, Jun. 20–25, 2004.

[2.15] M. Mu, Q. Li, D. J. Gilham, F. C. Lee, and K. D. T. Ngo, "New core loss measurement method for high-frequency magnetic materials," *IEEE Trans. Power Electron*., vol. 29, no. 8, pp. 4374–4381, Aug. 2014.

[2.16] M. Mu, Q. Li, D. Gilham, F. C. Lee, and K. D. T. Ngo, "New core loss measurement method for high frequency magnetic materials," *in Proc. IEEE Energy Conv. Cong. Expo.*, Atlanta, GA, pp. 4384–4389, Sept. 12–16, 2010.

[2.17] E. Agheb and H. K. Hoidalen, "Modification of empirical core loss calculation methods including flux distribution," *IET Electric Power Appl.*, vol. 7, no. 5, pp. 381–390, May 2013.

[2.18] S. A. Mousavi, G. Engdahl, and E Agheb, "Investigation of GIC effects on core losses in single phase power transformers," *Arch. Elect. Engg.*, vol. 60, no.1, pp. 35–47, 2011.

[2.19] C. P. Steinmetz, "On the law of hysteresis," *Trans. Ame. Ins. Elect. Engr.*, no. 1, pp. 1–64, Jan. 1892.

[2.20] J. Reinert, A. Brockmeyer, and R. W. A. A. De Doncker, "Calculation of losses in ferro- and ferrimagnetic materials based on the modified Steinmetz equation," *IEEE Trans. Ind. Appl*, vol. 37, no. 4, pp. 1055–1061, Jul.-Aug. 2001.

[2.21] J. Li, T. Abdallah, and C. R. Sullivan, "Improved calculation of core loss with nonsinusoidal waveforms," *in Proc. IEEE Ind. Appl Conf. 36th IAS Annu Meeting*, Chicago, IL, USA, Sep. 30–04 Aug. 2001, vol. 4, pp. 2203–2210.

[2.22] K. Venkatachalam, C. R. Sullivan, T. Abdallah, and H. Tacca, "Accurate prediction of ferrite core loss with nonsinusoidal waveforms using only Steinmetz parameters," *in Proc. IEEE Workshop Comp. Power Electron.*, Mayaguez, Puerto Rico, USA, pp. 36–41, Jun. 3–4, 2002.

[2.23] A. Van den Bossche, V. C. Valchev, and G. B. Georgiev, "Measurement and loss model of ferrites with non-sinusoidal waveforms," *in Proc. IEEE 35th Annu. Power Electron. Spec. Conf.*, Aachen, Germany, vol. 6, pp. 4814–4818, Jun. 20–25, 2004.

[2.24] W. Shen, F. Wang, D. Boroyevich, and C. W. Tipton, "Loss characterization and calculation of nanocrystalline cores for high-frequency magnetics applications," *IEEE Trans. Power Electron*, vol. 23, no. 1, pp. 475–484, Jan. 2008.

[2.25] L. R. Dupré, R. V. Keer, J. A. A. Melkebeek, “Evaluation of magnetostrictive effects in soft magnetic materials using the Preisach theory,” *J. Magn. Magn. Mater.,* vol. 254–255, pp. 121–123, Jan. 2003.

[2.26] S. Y. R. Hui and J. Zhu, “Numerical modelling and simulation of hysteresis effects in magnetic cores using transmission-line modelling and the Preisach theory,” *IEE Proc. – Elect. Pow. Appls*., vol. 142, no. 1, pp. 57–62, 1995.

[2.27] S. R. Naidu, “Simulation of the hysteresis phenomenon using Preisach's theory,” *IEE Proc. A Phy. Sci. Mea. Inst. Man. Edu.,* vol. 137, no. 2, pp. 73–79, 1990.

[2.28] J. G. Zhu, S. Y. R. Hui, and V. S. Ramsden, “A dynamic equivalent circuit model for solid magnetic cores for high switching frequency operations,” *IEEE Trans. Power Electron*., vol. 10, no. 6, pp. 791–795, Nov. 1995.

[2.29] G. Kadar and E. D. Torre, “Hysteresis modeling: I. Non-congruency,” *IEEE Trans. Magn.,* vol. 23, no. 5, pp. 2820–2822, Sep. 1987.

[2.30] E. D. Torre, “Existence of magnetization-dependent Preisach models,” *IEEE Trans. Magn.,* vol. 27, no. 4, pp. 3697–3699, Jul. 1991.

[2.31] J. Oti, F. Vajda, and E. D. Torre, “Identification of parameters in a moving model,” *J. Appl. Phys*., vol. 69, no. 8, pp. 4826–4828, 1991.

[2.32] F. Vajda and E. Della Torre, “Efficient numerical implementation of complete-moving-hysteresis models,” *IEEE Trans. Magn.,* vol. 29, no. 2, pp. 1532–1537, Mar. 1993.

[2.33] I. D. Mayergoyz, Mathematical Models of Hysteresis*,* Springer-Verlag, New York, 1991.

[2.34] Z. Szabó, J. Füzi, “Implementation and identification of Preisach type hysteresis models with Everett Function in closed form,” *J. Magn. Magn. Mater*., vol. 406, pp. 251–258, May 2016.

[2.35] D. Atherton, B. Szpunar, J. Szpunar, “A new approach to Preisach diagrams,” *IEEE Trans. Magn.,* vol. 23, no. 3, pp. 1856–1865, May 1987.

[2.36] I. D. Mayergoyz and G. Friedman, “Generalized Preisach model of hysteresis,” *IEEE Trans. Magn*., vol. 24, no. 1, pp. 212–217, Jan. 1988.

[2.37] J. G. Zhu, Numerical modelling of magnetic materials for computer aided design of electromagnetic devices, *Ph.D. Dissertation*, School of Electrical Engineering, University of Technology Sydney, Australia, July 1994.

[2.38] E. Fallah and J. S. Moghani, “A new approach for finite-element modeling of hysteresis and dynamic effects,” *IEEE Trans. Magn.,* vol. 42, no. 11, pp. 3674–3681, Nov. 2006.

[2.39] D. C. Jiles, J. B. Thoelke, and M. K. Devine, “Numerical determination of hysteresis parameters for the modeling of magnetic properties using the theory of ferromagnetic hysteresis,” *IEEE Trans. Magn.*, vol. 28, no. 1, pp. 27–35, Jan. 1992.

[2.40] N. Sadowski, N. J. Batistela, J. P. A. Bastos, and M. Lajoie-Mazenc, “An inverse Jiles-Atherton model to take into account hysteresis in time-stepping finite-element calculations,” *IEEE Trans. Magn.*, vol. 38, no. 2, pp. 797–800, Mar. 2002.

[2.41] J. P. A. Bastosa and N. Sadowski, Electromagnetic modeling by finite element methods, Boca Raton, FL: CRC Press, 438–455, 2003.

[2.42] A. J. Bergqvist, “A simple vector generalization of the Jiles-Atherton model of hysteresis,” *IEEE Trans. Magn.*, vol. 32, no. 5, pp. 4213–4215, Sep. 1996.

[2.43] P. Kis, and A. Iványi, “Parameter identification of Jiles–Atherton model with nonlinear least-square method,” *Phy. B: Cond. Mat*., vol. 343, nos. 1–4, pp. 59-64, Jan. 2004.

[2.44] W. Li I. H. Kim, S. M. Jang, and C. S. Koh, “Hysteresis modeling for electrical steel sheets using improved vector Jiles-Atherton hysteresis model,” *IEEE Trans. Magn.*, vol. 47, no. 10, pp. 3821–3824, Oct. 2011.

[2.45] M. Toman, G. Stumberger, and D. Dolinar, “Parameter identification of the Jiles–Atherton hysteresis model using differential evolution,” *IEEE Trans. Magn.*, vol. 44, no. 6, pp. 1098–1101, Jun. 2008.

[2.46] P. R. Wilson, J. N. Ross, and A. D. Brown, “Optimizing the Jiles-Atherton model of hysteresis by a genetic algorithm,” *IEEE Trans. Magn.*, vol. 37, no. 2, pp. 989–993, Mar. 2001.

[2.47] K. H. Carpenter, “A differential equation approach to minor loops in the Jiles-Atherton hysteresis model,” *IEEE Trans. Magn.*, vol. 27, no. 6, pp. 4404–4406, Nov. 1991.

[2.48] D. Lederer, H. Igarashi, A. Kost, and T. Honma, “On the parameter identification and application of the Jiles-Atherton hysteresis model for numerical modelling of measured characteristics,” *IEEE Trans. Magn.*, vol. 35, no. 3, pp. 1211–1214, May 1999.

[2.49] J. V. Leite, A. Benabou, and N. Sadowski, “Accurate minor loops calculation with a modified Jiles-Atherton hysteresis model,” *COMPEL-Int. J. Comput. Math. Elect. Electron. Eng*., vol. 28, no. 3, pp. 741–749, 2009.

[2.50] S. Hussain and D. A. Lowther, “The Modified Jiles–Atherton Model for the accurate prediction of iron losses,” *IEEE Trans. Magn.*, vol. 53, no. 6, Jun. 2017, Art no. 7300504.

[2.51] D. C. Jiles, and J. B. Thoelke, “Theory of ferromagnetic hysteresis: determination of model parameters from experimental hysteresis loops,” *IEEE Trans. Magn.*, vol. 25, no. 5, pp. 3928–3930, Sep. 1989.

[2.52] Y. Li, J. Zhu, Yongjian Li, H. Wang, and L. Zhu, “Modeling dynamic magnetostriction of amorphous core materials based on Jiles–Atherton theory for finite element simulations,” *J. Magn. Magn. Mater*., vol.529, Jul. 2021, Art. 167854.

[2.53] D. Zhang, M. Jia, Y. Liu, Z. Ren, and C. Koh, “Comprehensive improvement of temperature-dependent Jiles–Atherton model utilizing variable model parameters,” *IEEE Trans. Magn.*, vol. 54, no. 3, Mar. 2018, Art no. 7300504.

[2.54] J. V. Leite, N. Sadowski, P. Kuo-Peng, N. J. Batistela, and J. P. A. Bastos, “The inverse Jiles-Atherton model parameters identification,” *IEEE Trans.Magn.*, vol. 39, no. 3, pp. 1397–1400, May 2003.

[2.55] F. G. Baily, “The hysteresis of iron and steel in a rotating magnetic field,” *Phil. Trans. Royal Soc. A*, pp. 715–746, 1896.

[2.56] A. Basak and A. J. Moses, “Influence of stress on rotational loss in silicon iron,” *Proc. IEE,* vol.125, no.2, pp. 165–168, Feb. 1978.

[2.57] J. Sievert, H. Ahlers, M. Enokizono, S. Kauke, L. Rahf, and J. Xu, “The measurement of rotational power loss in electrical sheet steel using a vertical yoke system,” *J Mag. Magn. Mat*., vol. 112, no. 1–3, pp. 91–94, Jul. 1992.

[2.58] A. Kaplan, “Magnetic core losses resulting from a rotating flux,” *J. Appl. Phys*., vol. 32, no.3, pp370s–371s, Mar. 1961.

[2.59] F. Brailsford, “Rotational hysteresis loss in electrical sheet steels,” *J. Inst. Elect. Engrs.*, vol. 83, no. 502, pp. 566–575, Oct. 1938.

[2.60] M. Enokizono, T. Todaka, T. Sashikata, J.D. Sievert, and H. Ahlers, “Magnetic field analysis of rotational loss tester with vertical yoke,” *J Mag. Magn. Mat*., vol. 112, no. 1–3, pp. 81–84, July 1992.

[2.61] M. Enokizono, T. Suzuki, and J. D. Sievert, “Measurement of iron loss using rotational magnetic loss measurement apparatus,” *IEEE Trans. J. Magn. Jap.,* vol. 6, no. 6, pp. 508–514, Jun. 1991.

[2.62] T. Nakata, Y. Kawase, and M. Nakano, “Improvement of measuring accuracy of magnetic field strength in single sheet testers by using two H coils,” *IEEE Trans. Magn.*, vol. 23, no. 5, pp. 2596–2598, Sept. 1987.

[2.63] P. Flanders, “A hall sensing magnetometer for measuring magnetization, anisotropy, rotational loss and time effects,” *IEEE Trans. Magn.,* vol. 21, no. 5, pp. 1584–1589, Sep. 1985.

[2.64] E. Werner, Austria Patent no. 19115, 1949.

[2.65] W. Brix, K. Hempel, and F. Schulte, “Improved method for the investigation of the rotational magnetization process in electrical steel sheets,” *IEEE Trans. Magn.*, vol. 20, no. 5, pp. 1708–1710, Sep. 1984.

[2.66] P.J. Flanders, “The rotating-sample magnetometer”, *J. Appl. Phys.*, vol. 38, no. 3, pp. 1293–1294, Ma. 1967.

[2.67] F. Fiorillo and A. M. Rietto, “Extended induction range analysis of rotational losses in soft magnetic materials,” *IEEE Trans. Magn.*, vol. 24, no. 2, pp. 1960–1962, Mar. 1988.

[2.68] A. Moses and B. Thomas, “Measurement of rotating flux in silicon iron laminations,” *IEEE Trans. Magn.*, vol. 9, no. 4, pp. 651–654, Dec. 1973.

[2.69] W. Brix, K. Hempel, and W. Schroeder, “Method for the measurement of rotational power loss and related properties in electrical steel sheets,” *IEEE Trans. Magn.*, vol. 18, no. 6, pp. 1469–1471, Nov. 1982.

[2.70] M. Enokizono, T. Suzuki, and J. D. Sievert, “Measurement of dynamic magnetostriction under rotating magnetic field,” *IEEE Trans. Magn.*, vol. 26, no. 5, pp. 2067–2069, Sept. 1990.

[2.71] M. Enokizono, T. Suzuki, J. Sievert and J. Xu, “Rotational power loss of silicon steel sheet,” *IEEE Trans. Magn.*, vol. 26, no. 5, pp. 2562–2564, Sept. 1990.

[2.72] J. G. Zhu and V. S. Ramsden, “Two dimensional measurement of magnetic field and core loss using a square specimen tester,” *IEEE Trans. Magn.*, vol. 29, no. 6, pp. 2995–2997, Nov. 1993.

[2.73] Y. Guo, J. G. Zhu, J. Zhong, H. Lu, and J. X. Jin, “Measurement and modeling of rotational core losses of soft magnetic materials used in electrical machines: a review,” *IEEE Trans. Magn.*, vol. 44, no. 2, pp. 279–291, Feb. 2008.

[2.74] J. Sievert, “Studies on the measurement of two dimensional magnetic phenomena in electrical sheet steel at PTB,” 1st Int. Workshop on Magnetic properties of Electrical sheet steel under two-dimensional Excitation, Proceedings of the 93th PTB Seminar, Braunschweig, Germany, pp. 102-116, 1992.

[2.75] P. Huang, *et al*., “Optimal design and implementation of high-voltage high-power silicon steel core medium-frequency transformer,” *IEEE Trans. Ind. Electron.*, vol. 64, no. 6, pp. 4391–4401, Jun. 2017.

[2.76] G. Ortiz, J. Biela, and J. W. Kolar, “Optimized design of medium frequency transformers with high isolation requirements,” *IECON 2010 - 36th Ann.l Conf. IEEE Ind.l Electron. Society*, Glendale, AZ, 2010, pp. 631–638.

[2.77] M. Jaritz, S. Blume, and J. Biela, “Design procedure of a 14.4 kV, 100 kHz transformer with a high isolation voltage 115 kV),” *IEEE Trans. Dielec. Elect. Ins.*, vol. 24, no. 4, pp. 2094–2104, 2017.

[2.78] S. Zhao, Q. Li, and F. C. Lee, “High frequency transformer design for modular power conversion from medium voltage ac to 400V dc,” *2017 IEEE Appl. Power Electron. Conf. Exp. (APEC)*, Tampa, FL, 2017, pp. 2894–2901.

[2.79] M. Leibl, G. Ortiz, and J. W. Kolar, “Design and experimental analysis of a medium-frequency transformer for solid-state transformer applications,” *IEEE J. Emerg. Select. Top. Power Electron.*, vol. 5, no. 1, pp. 110–123, Mar. 2017.

[2.80] L. Zhang, D. Zhang, H. Shui, Y. Yuan, Q. Pei, and J. Zhu, “Optimisation design of medium frequency transformer for the offshore dc grid based on multi-objective genetic algorithm,” *IET Power Electron.*, vol. 10, no. 15, pp. 2157–2162, Dec. 2017.

[2.81] E. L. Barrios, A. Ursúa, L. Marroyo, and P. Sanchis, “Analytical design methodology for litz-wired high-frequency power transformers,” *IEEE Trans. Ind. Electron.*, vol. 62, no. 4, pp. 2103–2113, Apr. 2015.

[2.82] E. L. Barrios, A. Urtasun, A. Ursúa, L. Marroyo, and P. Sanchis, “High-frequency power transformers with foil windings: maximum interleaving and optimal design,” *IEEE Trans. Power Electron.*, vol. 30, no. 10, pp. 5712–5723, Oct. 2015.

[2.83] M. A. Bahmani, T. Thiringer, and M. Kharezy, “Design methodology and optimization of a medium-frequency transformer for high-power dc–dc applications,” *IEEE Trans. Ind. Appl.*, vol. 52, no. 5, pp. 4225–4233, Sept.-Oct. 2016.

[2.84] P. L. Dowell, “Effects of eddy currents in transformer windings,” *in Proc. Inst. Elec. Engr.*, vol. 113, no. 8, pp. 1387–1394, Aug. 1966.

[2.85] W. G. Hurley, E. Gath, and J. G. Breslin, “Optimizing the ac resistance of multilayer transformer windings with arbitrary current waveforms,” *IEEE Trans. Power Electron*, vol. 15, no. 2, pp. 369–376, Mar 2000.

[2.86] M. P. Perry, “Multiple layer series connected winding design for minimum losses,” *IEEE Trans. Power App. Systems*, vol. PAS-98, no. 1, pp. 116–123, Jan. 1979.

[2.87] J. A. Ferreira, “Appropriate modelling of conductive losses in the design of magnetic components,” *in Proc. 21st Annual IEEE Conf. Power Electron. Spec.*, San Antonio, TX, USA, pp. 780–785, 1990.

[2.88] J. A. Ferreira, “Analytical computation of AC resistance of round and rectangular Litz wire windings,” *in Proc.-B IEE Electric Power Appl.*, vol. 139, no. 1, pp. 21–25, Jan. 1992.

[2.89] M. Bartoli, N. Noferi, A. Reatti, and M. K. Kazimierczuk, “Modeling winding losses in high frequency power inductors,” *World Sc. J. Circ., Syst. Comp.*, *Special Issue Power Electronics*, part II, vol. 5, pp. 607–626, Dec. 1996.

[2.90] W. J. Gu and R. Liu, “A study of volume and weight vs. frequency for high-frequency transformers,” *in Proc. IEEE Power Electrn. Spec. Conf.*, Seattle, USA, pp. 1123–1129, Jun. 20–24, 1993.

[2.91] Z. Ouyang, J. Zhang, and W. G. Hurley, “Calculation of leakage inductance for high-frequency transformers,” *IEEE Trans. Power Electron*, vol. 30, no. 10, pp. 5769–5775, Oct. 2015.

[2.92] E. L. Barrios, A. Ursúa, L. Marroyo, and P. Sanchis, “Analytical design methodology for Litz-wired high-frequency power transformers,” *IEEE Trans. Ind. Electron*., vol. 62, no. 4, pp. 2103–2113, Apr. 2015.

[2.93] C. W. T. McLyman, Transformer and Inductor Design Handbook, Third Edition, Revised and Expanded, Kg. Magnetic, Inc. California, USA.

Chapter 3 Modelling of Amorphous Magnetic Material Using Empirical and Preisach Models

3.1 Introduction

Characterisation of magnetic core materials is very important for design of electromagnetic devices such as transformer. It has already been discussed in Chapter 2 that empirical, Preisach and J-A models are generally utilised to characterise a magnetic material. In this chapter, empirical and Preisach models are implemented to characterise the selected amorphous magnetic material, whereas J-A model is implemented in the next chapter.

Empirical method is firstly implemented to model the magnetic material. Empirical method is generally based on the original Steinmetz equation which is generally utilised for sinusoidal excitation [3.1]. The advantages of the empirical method are that it can be easily implemented in the design process of electromagnetic devices, and it requires less computational time and memory resources than those of other models. In contrast, the empirical method cannot be directly implemented into FEM and the model does not provide the actual magnetic properties [3.2].

On the other hand, Preisach or inverse Preisch model is one of the tools for characterisation of magnetic material which can predict core loss by tracing explicitly the magnetisation trajectory of magnetic flux density versus magnetic field strength. Thus, the method can be directly incorporated with FEM as the prediction of H from B can be calculated using inverse Preisach model. The Preisach model generally requires some experimental data to find out the magnetic distribution functions [3.3]−[3.5]. The Preisach magnetic distribution functions are generally based on the first, second or higher order transition curves, or limiting loop that is a low frequency large B-H loop of the magnetic material [3.3]−[3.8]. It is normally expected that the experimental data are obtained from manufacturers or simple experimental process. Since the determination of any order transition curves is more difficult than that of the limiting loop [3.6], in this thesis the limiting loop-based distribution function is considered. In this chapter, Preisach model is

also exploited for the numerical characterisation of the selected magnetic material (Amorphous 1k101 [3.9] which is also known as j1k101).

In the last decade, different Fe-based amorphous magnetic materials such as Metglas 2605S3A and 2605SA1 were characterised by using the empirical models [3.10]. The empirical models often generate high error if the loss is predicted at a point (frequency and magnetic flux density) far from those used for calculating the Steinmetz parameters. In addition, they cannot predict the trajectories of magnetic flux density from its magnetic field strength or its vice versa. However, the harmonic contents due to the non-sinusoidal excitations obtained by power electronic converters, would generate significant core losses due to the presence of minor loops [3.11]. The empirical methods cannot cope with the minor loops in the non-sinusoidal magnetisation process. The abovementioned problems can be solved by using Preisach model.

When magnetic field strength is applied on a magnetic material, the material is subjected to the magnetisation process, and a magnetic field is generated as output. Therefore, it can be said that the magnetisation depends on the magnetic field strength. It is also investigated that the magnetisation process is also affected by the internal magnetisation of elementary magnetic diploes which makes the process as magnetisation dependent.

There are different types of Preisach models in the literature such as normal Preisach model, moving Preisach model and generalised Preisach model. The normal Preisach model deals with only magnetic field strength as input, where the effect of internal magnetisation is not considered in the magnetisation process. On the other hand, the moving Preisach model [3.12]–[3.16] deals with a magnetisation dependent process, where the input is considered as sum of a feedback magnetisation based magnetic field strength, which is product of a feedback coefficient and the output magnetisation, and the applied magnetic field strength. Although this feedback coefficient changes with the magnitude of magnetic flux density and magnetic field strength, a constant feedback coefficient was used in [3.14]. In the magnetisation process of a ferro-magnetic material, there exists two magnetisation components: reversible and irreversible magnetisation components [3.17]. However, both the normal and moving Preisach models consider only the irreversible magnetisation component. The generalised Preisach model, on the other

hand, considers both the irreversible and reversible magnetisation components, as well as the magnetisation dependent component with a feedback coefficient [3.6], [3.18], [3.19].

The classical Preisach model or normal Preisach model is generally used for predicting the hysteresis loss where the Preisach function is a static function of magnetic field strength. For prediction of dynamic hysteresis loss (a combination of hysteresis, eddy current and excess losses), dynamic Preisach models are used where the Preisach function considers not only the magnetic field strength but also the rate of change of magnetic flux density with respect to time [3.3], [3.20]. Thus, the inclusion of dynamic effect is necessary to include with the static Preisach model for its practical application.

For design and performance analysis of electromagnetic devices and systems, the finite element method is commonly employed to calculate the magnetic field distribution by using the vector magnetic potential, which requires the prediction of magnetic field strength from the magnetic flux density in each finite element. Since the normal Preisach models predict magnetic flux density from magnetic field strength, an inverse Preisach is required for the prediction of magnetic field strength from the magnetic flux density. In [3.21], a dynamic inverse Preisach model was proposed, in which the inverse Preisach function is obtained by curve fitting the first order polynomial function of static inverse Preisach function and the rate of change of magnetic flux density with time. In [3.22], another inverse Preisach method was proposed based on the recursive procedure which has high computational burden. In [3.23], a normal inverse Preisach model was presented by using the normal Preisach function to find out the magnetic field strength from the magnetic flux density. The advantage of normal inverse method in [3.23] is that it does not require any iteration and extra curve fitting, and thus the computational cost becomes low. However, none of the above mentioned inverse Preisach models consider the reversible magnetisation and feedback coefficient in the magnetisation process. In addition, to the best knowledge of the author of this thesis, no investigation has been reported in the literature on the effects of minor loops on characterisation process using the inverse Preisach models. Neither the normal or inverse Preisach models has been used to characterise the selected Fe-based amorphous magnetic material (amorphous 1k101 [3.9]).

In this chapter, firstly original Steinmetz equation based empirical model is utilised to model the selected Fe-based amorphous magnetic material. Later, a limiting loop based Preisach and inverse Preisach models are used to characterise the magnetic material. In addition, a new technique to find out the feedback coefficient of the generalised Preisach model whose value varies with the magnitude of magnetic flux density has been also proposed in this chapter. In addition, development of a generalised inverse Preisach model based on the generalised Preisach model by incorporating the reversible magnetisation and magnetisation dependent hysteresis effects is proposed in this chapter. Moreover, the effect of variable squareness, which indicates the proportion of reversible magnetisation in the magnetisation process, is studied in this chapter. The chapter also includes the investigation of the effects of minor loops by using the proposed inverse Preisach model.

3.2 Empirical Model

Original Steinmetz equation, which is normally exploited for sinusoidal excitation, is used as empirical model in this study. For sinusoidal excitation, the original Steinmetz equation can be expressed as [3.1], [3.24]:

$$P = kf^{\alpha} B_m^{\beta} \tag{3.1}$$

where k, α and β are the Steinmetz parameters which are calculated using curve fitting of measured data. The core losses at various magnetic flux densities and sinusoidal frequencies are firstly calculated, and the obtained losses are then curve-fitted by general reduced gradient GRG) of Excel's Solver [3.25]. In the GRG technique, an error (*Err*) is needed to be set which can be defined as follows [3.25]:

$$Err = \sum_{i}^{n} \frac{\left(P_{mi} - P_{si}\right)^2}{P_{mi}} \tag{3.2}$$

where P_{mi} and P_{si} are the measured and calculated core loss data, and n is the total number of observational measured data. However, the experimental process for the measurement

of core losses at various magnetic flux densities and frequencies are discussed in Section 3.7 of this chapter.

3.3 Preisach Model

3.3.1 Normal Preisach Model

In the normal Preisach model, a magnetic material is considered as a set of magnetic dipoles [3.26], and each of which has rectangular elementary shapes, as shown in Fig. 3.1(a). Fig. 3.1(b) shows the Preisach diagram, where S is the triangular region on the (α, β) plane for $H_{sat} \geq \alpha \geq \beta \geq -H_{sat}$, and S^+ and S^- are regions of positive and negative switched dipoles. If the applied magnetic field strength is H, the output magnetisation M and the corresponding magnetic flux density B can be calculated by (3.3) and (3.4) [3.6], [3.27], [3.28] as follows, respectively:

$$M(H) = \iint_S \mu(\alpha, \beta)\gamma_{\alpha\beta}(H)\,d\alpha\,d\beta \tag{3.3}$$

$$B = \mu_0[H + M(H)] \tag{3.4}$$

where $\mu(\alpha, \beta)$ is the distribution function of the magnetic dipoles, $\gamma_{\alpha\beta}$ the Preisach operator which is 1 on S^+ and -1 on S^-, and S the triangular region on the (α, β) plane for $H_{sat} \geq \alpha \geq \beta \geq -H_{sat}$ as shown in Fig. 3.1(b).

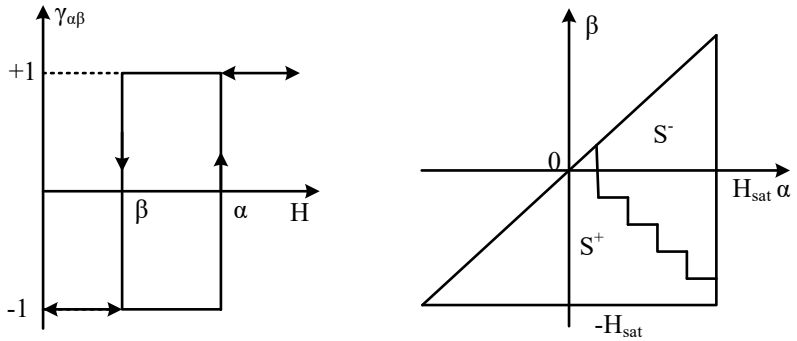

Fig. 3.1. (a) Rectangular hysteresis model of magnetic dipoles [3.6], [3.29], and (b) Preisach diagram [3.6], [3.29].

From the Preisach diagram shown in Fig. 3.1(b), the downward and upward magnetisations for a given magnetic field strength can be expressed as

$$M(H) = M(H_n) - 2T(H_n, H) \qquad \text{(Downward)} \tag{3.5}$$

$$M(H) = M(H_n) + 2T(H, H_n) \qquad \text{(Upward)} \tag{3.6}$$

where H_n represents the magnetic field strength at the last reversal point, and $T(\alpha, \beta)$ is a function of the upward and downward magnetisation trajectories. $T(\alpha, \beta)$ can be calculated from a data table of a limiting hysteresis loop, which is a large loop of B (magnetic flux density) and H (magnetic field strength) of a given magnetic core measured at a very low frequency (e.g. not more than 1 Hz). The expression of $T(\alpha, \beta)$ is as follows [3.6], [3.27], [3.28]:

$$T(\alpha, \beta) = \frac{M_u(\alpha) - M_d(\beta)}{2} + F(\alpha)F(-\beta) \tag{3.7}$$

where $M_d(\alpha)$ and $M_u(\beta)$ are the downward and upward magnetisations of the limiting loop, and $F(\alpha)$ can be determined by

$$F(\alpha) = \frac{M_d(\alpha) - M_u(\alpha)}{2\sqrt{M_d(\alpha)}} \quad \text{when } \alpha \geq 0 \tag{3.8}$$

$$F(\alpha) = \sqrt{M_d(-\alpha)} \qquad \text{when } \alpha < 0. \tag{3.9}$$

$F(-\beta)$ can also be calculated using (3.8) and (3.9) depending on the value of β.

In the same way, the initial magnetisation can be expressed as

$$M(H) = T(H, -H)\,. \tag{3.10}$$

3.3.2 Generalised Preisach Model

In the generalised Preisach model, the irreversible component of magnetisation is obtained by using the normal Preisach model. On the other hand, the reversible component is proportional to the difference between the anhysteretic magnetisation and

irreversible magnetisation components [3.6]. To make the magnetisation dependent Preisach function, a magnetisation feedback is added in the Preisach model. The combination of applied magnetic field strength and feedback magnetic field strength is generally known as effective magnetic field strength [3.30]. Therefore, the magnetisation of a magnetic material, and the corresponding reversible magnetisation and effective magnetic field strength at a given magnetic field strength can be written as [3.6], [3.30]:

$$M(H) = M_{irr}(H_e) + M_{rev}(H_e) \tag{3.11}$$

$$M_{rev}(H_e) = c\{M_{an}(H_e) - M_{irr}(H_e)\} \tag{3.12}$$

$$H_e = H + KM \tag{3.13}$$

where M_{irr} is the irreversible magnetisation, M_{rev} the reversible magnetisation, M_{an} the anhysteric magnetisation, H_e the effective magnetic field strength, K the feedback coefficient, and c a constant.

Substituting (3.12) into (3.11), one obtains

$$M(H) = \mathrm{S}M_{irr}(H_e) + (1-\mathrm{S})M_{an}(H_e) \tag{3.14}$$

where S=1–c is known as the squareness of the elementary loop which can be calculated using the initial susceptibilities of normal magnetisation and anhysteretic magnetisation [3.6]. Since there is a feedback coefficient in the generalised Preisach models, an iterative process is needed to calculate the magnetisation at each point of the applied magnetic field strength.

3.4 Inverse Preisach Model

3.4.1 Normal Inverse Preisach Model

The normal inverse Preisach model, which is based on the above-mentioned normal Preisach model, calculates the magnetic field strength from the magnetic flux density [3.23]. The prediction of the magnetic field strength for the next time step can be obtained by (3.15) [3.30]:

$$H(t+\Delta t) = H(t) + \frac{\Delta B}{dB/dH} \tag{3.15}$$

where ΔB is the change of magnetic flux density between two successive discrete times, Δt the time step, and dB/dH the derivative of magnetic flux density B with respect to magnetic field strength H.

Taking the first order derivatives of both sides of (3.4) with respective to H, one obtains

$$\frac{dB}{dH} = \mu_0 + \mu_0 \frac{dM}{dH} \tag{3.16}$$

where dM/dH can be obtained from the limiting loop and the magnetic flux density.

Since the corresponding upward and downward magnetisations are known for a given limiting loop, the derivatives of the upward and downward magnetisations, dM_d/dH and dM_u/dH, of the limiting loop with respect to H can also be obtained. Consequently, the first order derivatives of upward and downward magnetisations with respect to H can be calculated from (3.5) and (3.6) by

$$\frac{dM}{dH} = -2\frac{dT(H_n, H)}{dH} \quad \text{For downward trajectory} \tag{3.17}$$

$$\frac{dM}{dH} = 2\frac{dT(H, H_n)}{dH} \quad \text{For upward trajectory} \tag{3.18}$$

where $dT(H_n, H)/dH$ and $dT(H, H_n)/dH$ can be calculated from (3.7) which are as follows:

$$\frac{dT(H_n, H)}{dH} = -\frac{1}{2}\frac{dM_d}{dH} - F(H_n)\frac{dF(-H)}{dH} \tag{3.19}$$

$$\frac{dT(H, H_n)}{dH} = \frac{1}{2}\frac{dM_u}{dH} + F(-H_n)\frac{dF(H)}{dH}. \tag{3.20}$$

Similarly, for the initial magnetisation, dM/dH can be obtained from (3.10) and (3.7) by

$$\frac{dM}{dH} = \frac{dT(H,-H)}{dH} = \frac{1}{2}\frac{dM_u(H)}{dH} + \frac{1}{2}\frac{dM_d(-H)}{dH} + 2F(H)\frac{dF(H)}{dH} \tag{3.21}$$

where $dF(H)/dH$ can be obtained from (3.8) and (3.9) by

$$\frac{dF(H)}{dH} = \frac{1}{4\sqrt{M_d(H)}}\frac{dM_d}{dH}\left\{1+\frac{M_u}{M_d}\right\} - \frac{1}{2\sqrt{M_d(H)}}\frac{dM_u}{dH} \qquad \text{for } H \geq 0 \tag{3.22}$$

$$\frac{dF(H)}{dH} = -\frac{1}{2\sqrt{M_d(-H)}}\frac{dM_d(-H)}{dH} \qquad \text{for } H < 0. \tag{3.23}$$

3.4.2 Proposed Inverse Preisach Model

The inverse Preisach model proposed in this chapter is based on the generalised Priesach model presented in Section 3.3.2. In this approach the effective magnetic field strength is mainly concerned in the model instead of conventional magnetic field strength. While the magnetic field strength is calculated by (3.15) similar to the normal inverse Preisach model, the proposed inverse Preisach model is different from the normal inverse Preisach in the way to calculate dB/dH in (3.15). The first order derivative of the effective field strength with respect to the applied magnetic field strength (dH_e/dH) can be obtained from (3.13) by

$$\frac{dH_e}{dH} = 1 + K\frac{dM}{dH} \tag{3.24}$$

with

$$\frac{dM}{dH} = \frac{dM}{dH_e}\frac{dH_e}{dH}. \tag{3.25}$$

Substituting (3.24) into (3.25), one obtains

$$\frac{dM}{dH} = \frac{\dfrac{dM}{dH_e}}{1 - K\dfrac{dM}{dH_e}}. \tag{3.26}$$

The first order derivative of magnetisation with respect to the effective magnetic field strength (dM/dH_e) can be obtained from (3.14) by

$$\frac{dM}{dH_e} = \mathrm{S}\frac{dM_{irr}}{dH_e} + (1-\mathrm{S})\frac{dM_{an}}{dH_e} \tag{3.27}$$

where dM_{irr}/dH_e can be calculated by using the normal inverse Preisach model and dM_{an}/dH_e can be obtained from the anhysteretic curve.

Substituting (3.26) into (3.16), one obtains

$$\frac{dB}{dH} = \mu_0 + \mu_0 \frac{\dfrac{dM}{dH_e}}{1 - K\dfrac{dM}{dH_e}} \tag{3.28}$$

It is worth noting that the proposed inverse Preisach model does not require an iteration process although the generalised Preisach model does.

3.5 Implementation of Preisach Models

This section presents the implementation of the normal and generalised Preisach models, which require only the limiting loop data, and need the magnetic field strength as the input. Fig. 3.2 shows the measured limiting loop of the selected Fe-based amorphous magnetic material, where the left and right trajectories are the downward and upward trajectories of the limiting loop, and the remanence and coercive force are 0.81 T and 10.8 A/m, respectively. Taking advantages of the symmetry, only the left half of the limiting loop is stored in the form of a look up table.

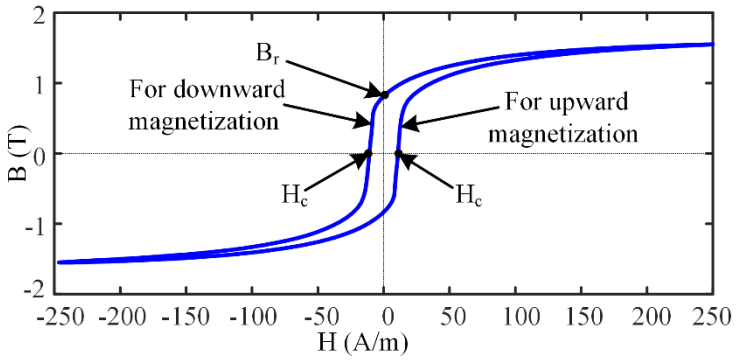

Fig. 3.2. Limiting loop of the Fe-based amorphous magnetic material.

3.5.1 Implementation of Normal Preisach Model

In the normal Preisach model, the initial magnetisation at a given magnetic field strength is calculated by (3.10) and (3.7). After reaching the first reversible point, the operating point is at the downward trajectory as shown in Fig. 3.3. For the downward and upward trajectories, the magnetisations at a given magnetic field strength are calculated by (3.5) and (3.6), respectively. The magnetisation and the corresponding magnetic field strength at the last reversible point are stored as they are required in (3.5) and (3.6) to calculate magnetisation. The process is repeated until it reaches the final time t_f. Finally, the corresponding magnetic flux density B can be obtained by (3.4).

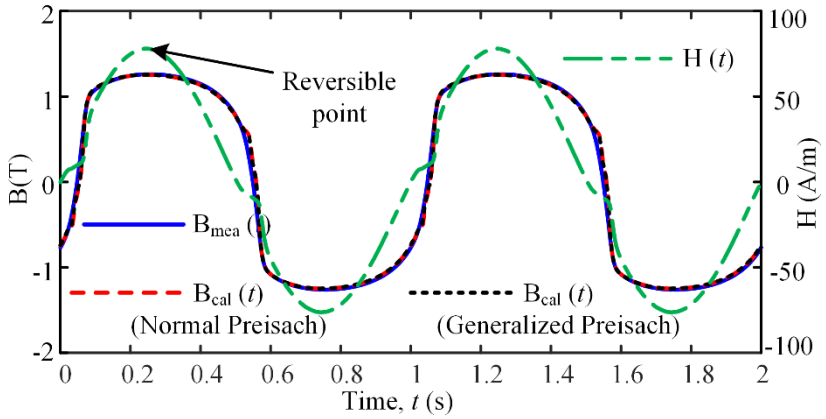

Fig. 3.3. Applied magnetic field strength and corresponding measured and calculated magnetic flux densities.

3.5.2 Implementation of Generalised Preisach Model

To implement the generalised Preisach model, the anhysteretic magnetisation curve, squareness and feedback coefficient are required to be identified for a given magnetic material. The identification of the anhysteretic curve, squareness and feedback coefficient are explained below.

3.5.2.1 Identification of Anhysteretic Magnetisation Curve

The anhysteretic magnetisation curve indicates the ideal magnetisation curve with no iron loss. The anhysteretic magnetisation curve plays important role during inclusion of reversible magnetisation with the total magnetisation. The anhysteretic magnetisation curve can be obtained by both experimental and simulation-based methods. In this study, simulation-based method is utilised to find out the anhysteretic magnetisation curve. The authors of [3.18] proposed a method for identification of anhysteretic magnetisation curve where the normal Preisach model is exploited to determine the anhysteretic magnetisation. In this process, an AC magnetic field strength is superimposed on a DC magnetic field strength at each point [3.6], [3.18], and the amplitude of AC magnetic field strength is set to decay gradually from the maximum to zero for simulating the demagnetisation process. The decay from the peak to zero magnetic field strength is done by finite number of steps. The reduction of AC magnetic field strength is done by two ways: one is at reversible point after downward magnetisation, as shown Fig. 3.4(a), and the other at reversible point after upward magnetisation, as shown Fig. 3.4(b). The magnetisation processes for both cases at H_{DC} point are shown in Figs. 3.5(a) and (b).

From Fig. 3.5, it is observed that for both reduction processes, the anhysteretic magnetisation point is not the same. Thus, two anhysteretic magnetisation curves are obtained from two types of reduction: the first one is upper and the second one lower anhysteretic magnetisation curves. The average of them is finally considered as the resultant anhysteretic magnetisation curve. For both ways of reduction of AC magnetic field strength, each step reduction is carried by $(H_{sat}-H_{DC})/N_{st}$, where H_{DC} is the DC magnetic field strength where the anhysteretic magnetisation value is calculated, and N_{st} is the number of steps. The resultant anhysteretic magnetisation and its derivative of the Fe-based amorphous material sample are shown in Fig. 3.6.

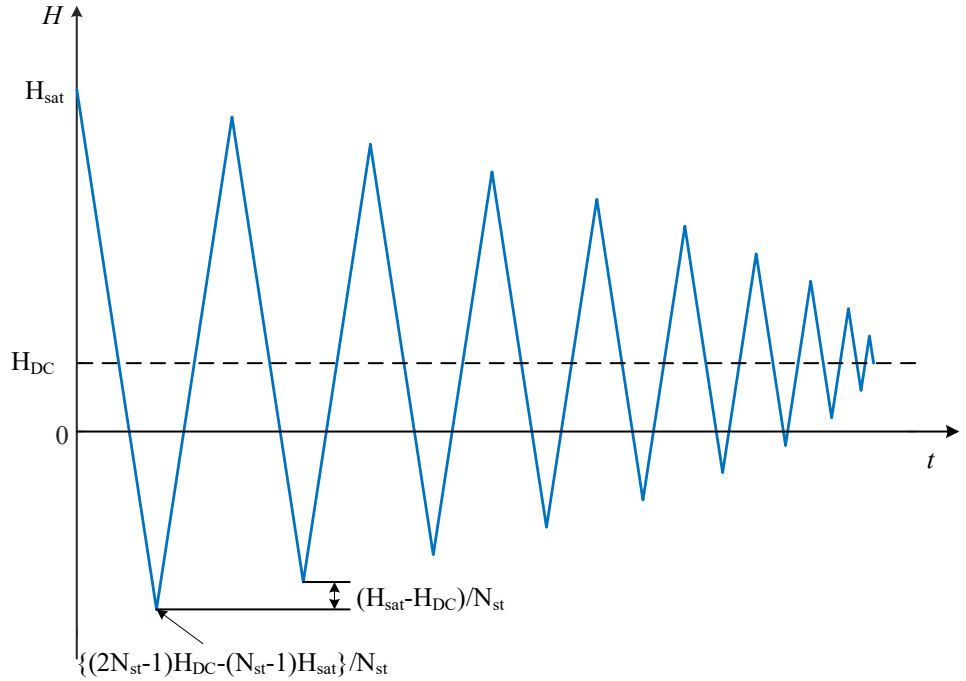

(a)

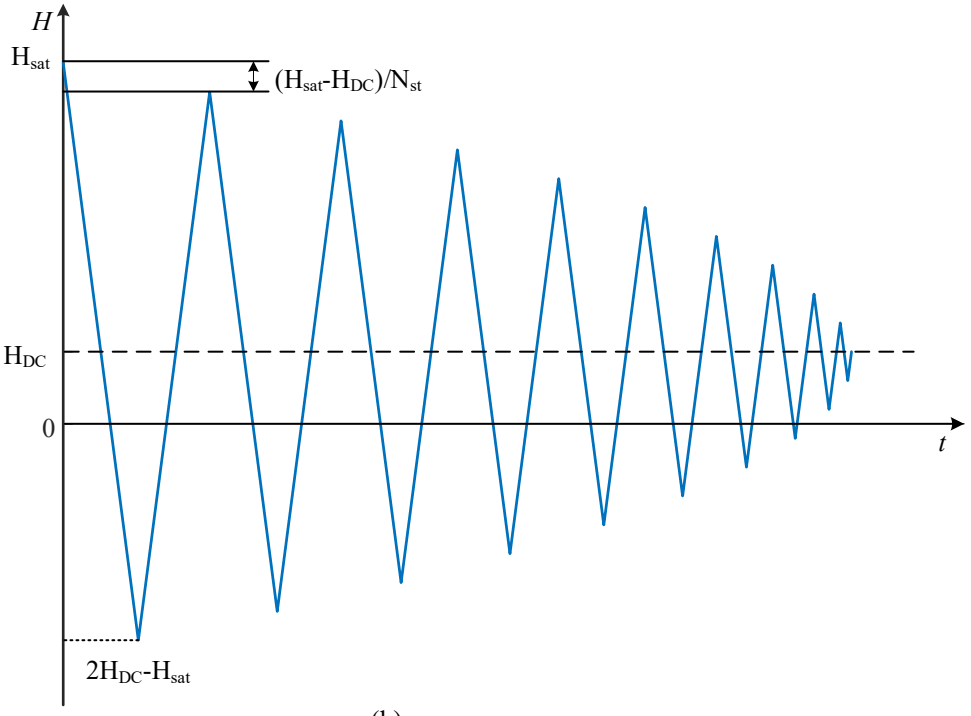

(b)

Fig. 3.4. Excitation magnetic field strength for prediction of anhysteretic magnetisation using normal Preisach model: (a) upper value of anhysteretic magnetisation, and (b) lower value of anhysteretic magnetisation [3.6].

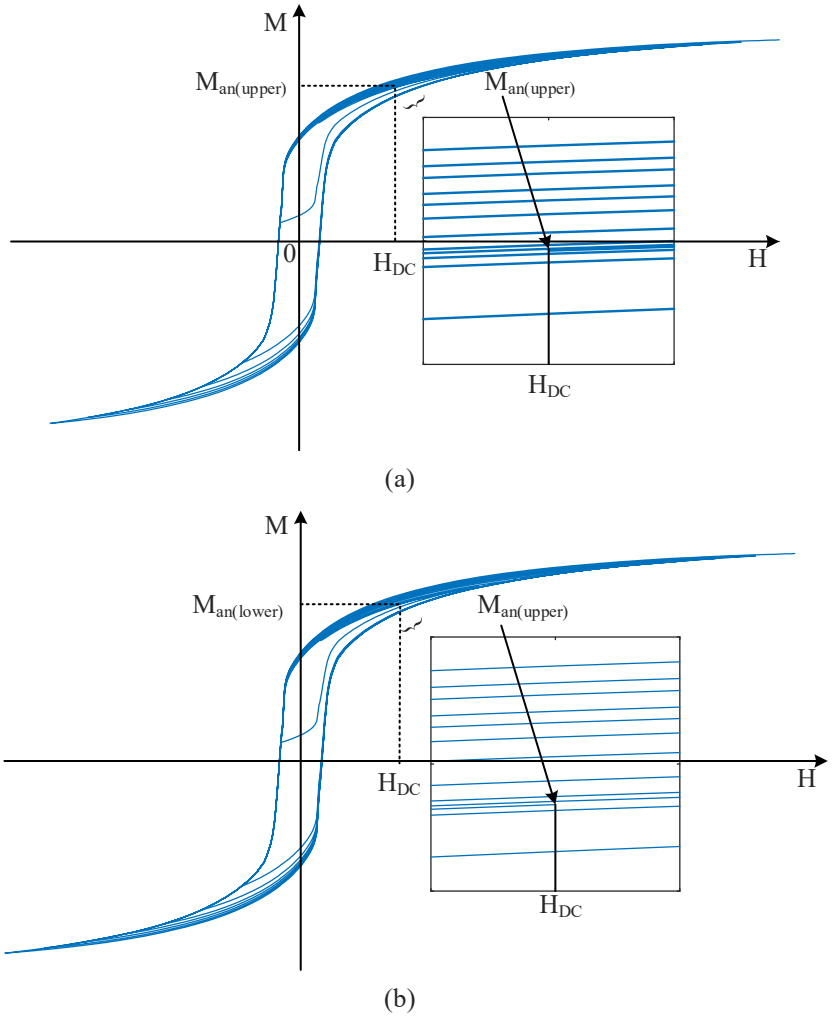

Fig. 3.5. Magnetisation processes for anhysteretic magnetisation using normal Preisach model: (a) upper value of anhysteretic magnetisation, and (b) lower value of anhysteretic magnetisation.

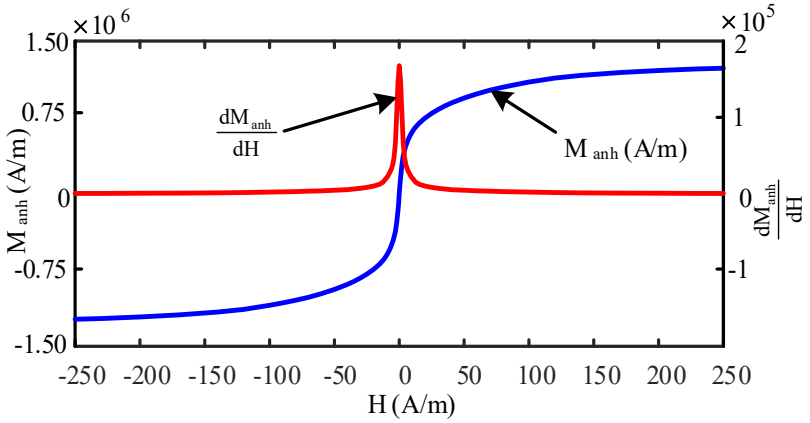

Fig. 3.6. Anhysteretic magnetisation curve of the Fe-based amorphous magnetic material calculated by the normal Preisach model and its derivative with respect to magnetic field strength *H*.

3.5.2.2 Identification of Squareness

The squareness, S, can be calculated as follows [3.6]:

$$S = 1 - \frac{\chi_{io}}{\chi_{anho}} \tag{3.29}$$

where χ_{io} and χ_{anho} are the initial susceptibilities of the normal and anhysteretic magnetisation curves, respectively.

3.5.2.3 Identification of Feedback Coefficient

According to [3.14], the magnetisation feedback coefficient K can be calculated by

$$K = \frac{M_e - M}{\chi M} \tag{3.30}$$

where M and M_e are the magnetisations calculated by the normal Preisach model and measured by experiment respectively, and χ is the susceptibility of a major loop at a given magnetic field strength. Fig. 3.7 illustrates the feedback coefficient values for the upward magnetisation of the Fe-based amorphous magnetic material at different magnetic flux density values. From Fig. 3.7, the following three observations can be made:

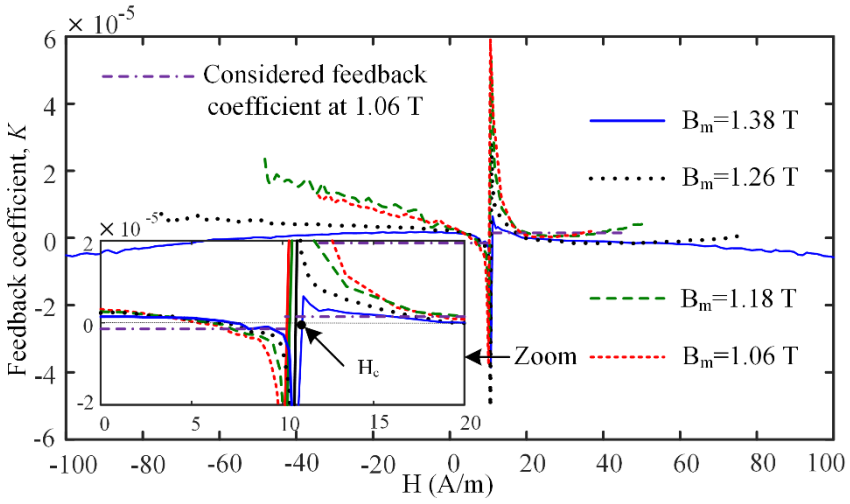

Fig. 3.7. Feedback coefficient for the upward magnetisation of the Fe-based amorphous magnetic material at different magnetic flux density magnitudes.

(i) The feedback coefficient of the upward magnetisation changes with both the magnitudes of magnetic flux density and magnetic field strength;

(ii) Near to the coercive force, the feedback coefficient jumps to the opposite direction and then decreases exponentially with the magnetic field strength; and

(iii) The value of feedback coefficient decreases with the increase of flux density magnitude.

Moreover, it is reported in [3.14] that the higher the standard deviation of dM/dH, the higher error is likely in the calculated results, and the standard deviation of dM/dH in the region near the coercive forces is higher than that of the rest part of *B-H* loop. Accordingly, from Fig. 3.8, it can be observed that at the vicinity of coercive forces, the discrepancy between the simulated and measured *B-H* loops is higher than the other part of the loop. To reduce the discrepancy, a new technique based on the above-mentioned observations is proposed to identify the feedback coefficient. On the upward trajectory, K is taken as a positive value for $H \geq H_c$ and a negative value for $H < H_c$. At the same time, the value of K decreases with the magnitude of magnetic flux density. The values of K at different magnitudes of magnetic flux density (B_{m}) are calculated in such a way that the hysteresis loss is minimised without distorting the *B-H* loop, and then the values of K are curve fitted by an exponential function. From the data set of K and B_{m}, linear interpolation can also be used instead of curve fitting technique to find out the K at any point of B_{m} in its specific range. Fig. 3.9 shows the feedback coefficient of upward trajectory for $H \geq H_c$ obtained by curve fitting. The feedback coefficients of upward and downward trajectories of Fe-based amorphous magnetic material can be expressed by

$$K = \begin{cases} a_1 e^{-b_1 B_m} + c_1 & H \geq H_c \\ -(a_1 e^{-b_1 B_m} + c_1) & H < H_c \end{cases} \quad \text{(Upward)} \tag{3.31}$$

$$K = \begin{cases} -(a_1 e^{-b_1 B_m} + c_1) & H \geq -H_c \\ (a_1 e^{-b_1 B_m} + c_1) & H < -H_c \end{cases} \quad \text{(Downward)} \tag{3.32}$$

where a_1=1.40113×10^{-4}, b_1=4.71577, and c_1=2.95626×10^{-7}, respectively. The generalised Preisach model with the proposed feedback coefficient can effectively reduce the discrepancy between the simulated and experimental results, as shown in Fig. 3.8. If the maximum magnetic flux density is unknown before implementing the model, the feedback coefficient can be calculated from the peak magnetic field strength as magnetic field strength is used as input in Preisach model. Thus, the feedback coefficient can also be presented as a function of H_m. Fig. 3.10 shows the feedback coefficient of upward magnetisation of Preisach model with H_m for $H \geq H_c$.

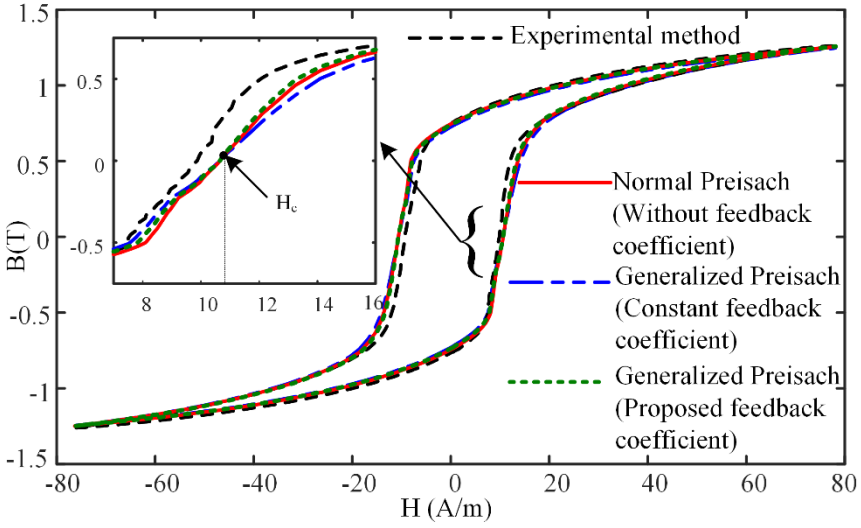

Fig. 3.8. Comparison of the *B-H* loops predicted by using constant feedback coefficient, proposed feedback coefficient, and no-feedback coefficient with the experimental result.

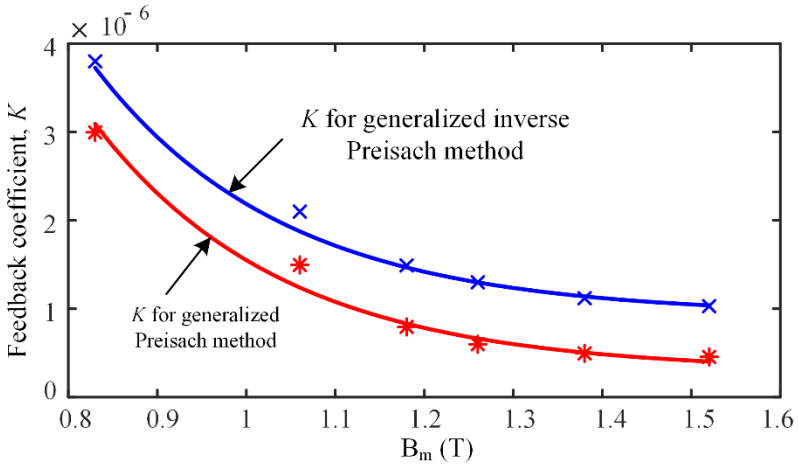

Fig. 3.9. The feedback coefficient of upward magnetisation with the change of B_m for $H \geq H_c$.

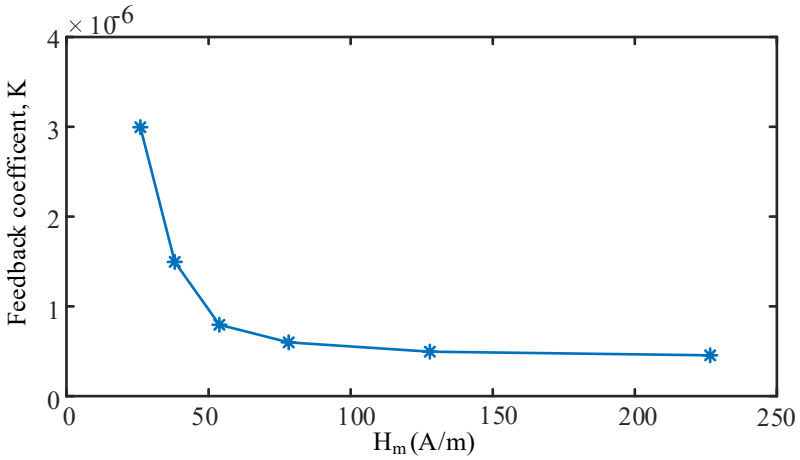

Fig. 3.10. The feedback coefficient of upward magnetisation with the change of H_m for $H \geq H_c$.

To implement the generalised Preisach model, magnetisation is calculated by (3.14), where the first term is calculated by the normal Preisach model and the value of squareness, and the rest is calculated from the anhysteretic magnetisation and squareness. The resultant magnetisation is calculated iteratively until the error between two successive results meets a pre-specified convergence criterion. To increase the convergence rate, a suitable acceleration factor or relaxation coefficient, g, is used, and magnetisation in each iteration is updated as follows [3.6]:

$$M_o' = M_o + g\left(M - M_o\right) \tag{3.33}$$

where M_o', M and M_o are the updated, current and previous magnetisations, respectively.

On the other hand, minor loops occur due to the incremental H and B, and hence the applied H contains local reversible points. To extract the simulated magnetic flux density using the Preisach model, the local reversible points must be popped out if the operating magnetic field strength outstrips the last reversible point in the previous opposite trajectory [3.6]. Consequently, the minor loop is wiped out and does not affect the next step magnetisation process. Fig. 3.11 shows an applied magnetic field strength which contains two pairs of local reversible points (b, c, e and f). The general magnetisation process is carried out up to the popping out point, P. When the operating magnetic field strength exceeds the value of magnetic field strength at point P, which is equal to the magnetic field strength at point b, the last reversible magnetic field strength H_{cc} (magnetic

field strength at point *c*) is replaced by H_a (magnetic field strength at reversible point *a*) in the magnetisation process. As a result, the minor loop is completed, and the magnetisation process proceeds onto the major *B*-*H* loop. Due to the minor loops, the loss in the core increases.

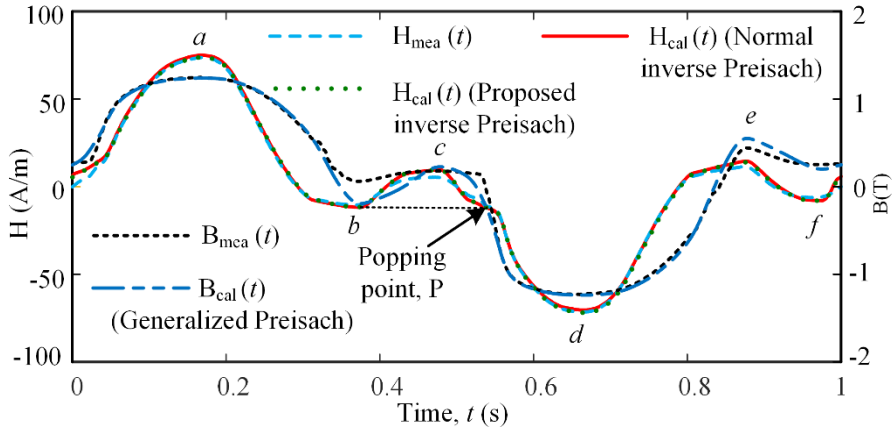

Fig. 3.11. Calculated and measured magnetic field strengths and magnetic flux densities for minor loops.

3.6 Implementation of Inverse Preisach Models

3.6.1 Implementation of the Normal Inverse Preisach Model

The normal inverse Preisach model also uses the limiting loop as the input data. The corresponding derivatives of upward and downward magnetisations with respect to the magnetic field strength *H* are then calculated. The derivative of Preisach function can be calculated in two ways: the first one is to use the derivatives obtained by (3.22) or (3.23) depending on the sign of *H*, and the other is to calculate it numerically using the data table of Preisach function.

On the initial magnetisation curve, the derivative of magnetisation with respect to *H* (*dM*/*dH*) is calculated by (3.21), and *H*(*t*) is then calculated by (3.15) and (3.16). Similar to the normal Preisach model, the process continues until it reaches the first reversible point. The magnetic field strength at a reversible point and its corresponding magnetisation is stored in a stack. After that the derivative of magnetisation with respect to *H* is calculated by (3.17) and (3.19) for the downward trajectory. Similarly, (3.18) and (3.20) can be used to calculate the derivative of magnetisation with respect to *H* on the

upward trajectory. The magnetic field strength is then calculated from dM/dH by (3.15) and (3.16). The process is repeated until it reaches the final time step.

3.6.2 Implementation of Generalised Inverse Preisach Model

Due to consideration of the reversible magnetisation and feedback coefficient in the proposed generalised inverse Preisach model, the calculation of dB/dH, as shown in (3.28), becomes different from the normal inverse Preisach model. The dM/dH_e in (3.28) is calculated by (3.27) which requires the calculation of dM_{irr}/dH_e, squareness, and data table of dM_{an}/dH_e. The other process is then done in a way similar to the normal inverse Preisach model. The normal inverse Preisach model produces higher error than the normal Preisach model, as listed in Tables 3.2 and 3.3 (Section 3.8.2.), since $H(t)$ is calculated by (3.15) which is a successive approximation procedure neglecting the higher order derivative terms. Therefore, the feedback coefficient for the generalised inverse Preisach model is considered slightly higher than the generalised Preisach model as shown in Fig. 3.9 to compensate the excess error. The value of c_1 in (3.31) and (3.32) increases from 2.95626×10^{-7} to 9.305626×10^{-7} for the generalised inverse Preisach model, and the other values of parameters are considered as the same as those in the generalised Preisach model. The flow chart of the generalised inverse Preisach model is shown in Fig. 3.12.

Similar to the Preisach model, the generalised or normal inverse Preisach model requires modification during wiping out of minor loops. When the magnetic flux density outstrips the popping point, as shown in Fig. 3.11, the local reversible magnetic field strength is replaced by the global reversible magnetic field strength. After wiping out the minor loop, the rest process is carried out on the major loop. Since the feedback coefficient is calculated from a major loop, the feedback coefficient of generalised inverse model in this case is only applied on the major loop.

In the abovementioned generalised inverse Preisach model, the squareness is considered as constant, and measured based on the limiting loop. It has been already discussed in Chapter 2 that the contribution of reversible magnetisation in the total magnetisation is variable where its contribution is initially high and later it decreases. Thus, the squareness can be considered as variable with the magnetic field. Therefore, the generalised inverse Preisach model can also be carried out using the variable squareness. For simplicity, in

this approach constant feedback coefficient is used in this case. An optimisation technique is used for identification of the squareness and feedback coefficient instead of the aforementioned techniques.

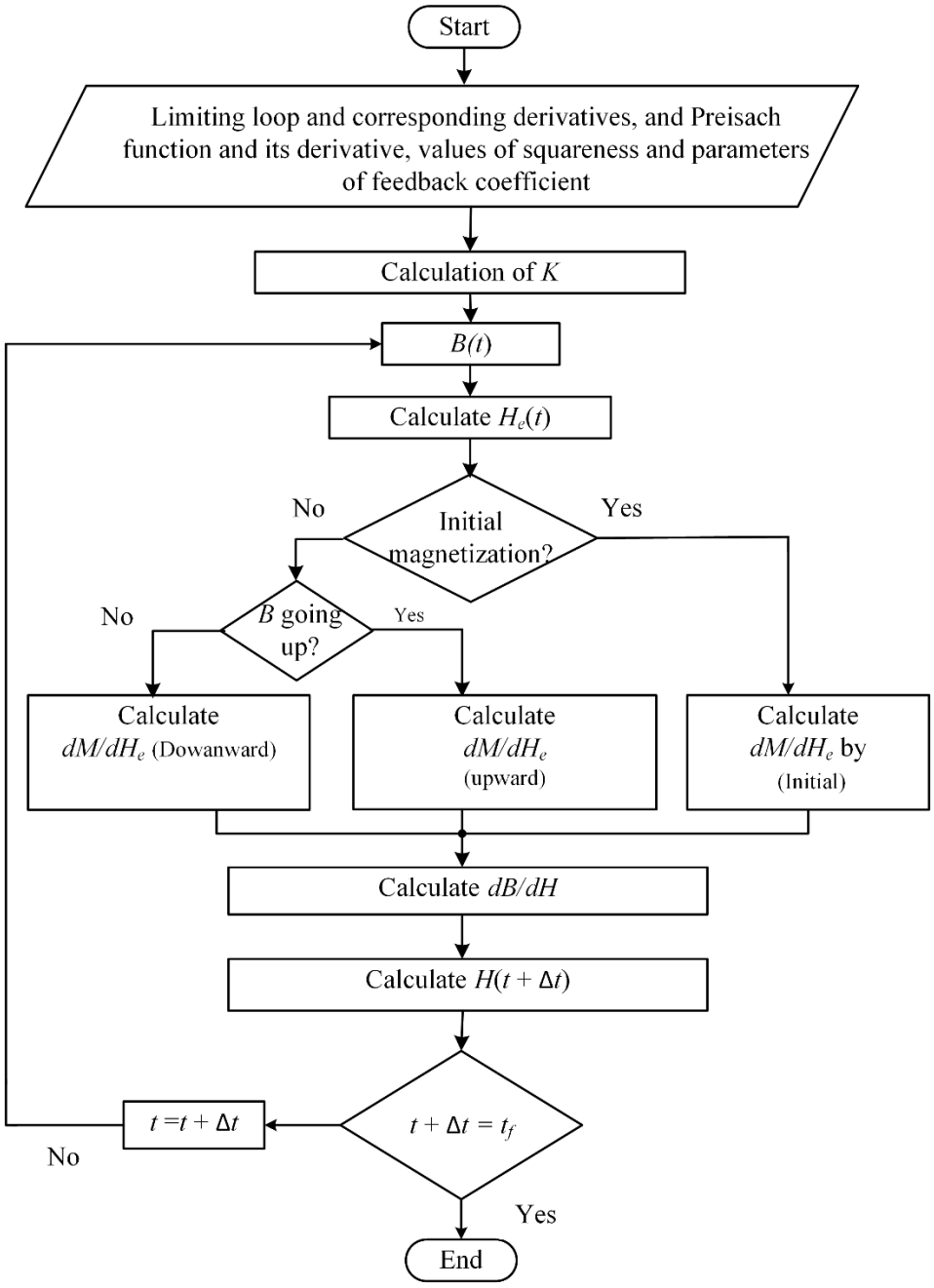

Fig. 3.12 Flow chart of the proposed inverse Preisach model.

In the optimisation technique, the relative iron loss error, and root mean square of error between measured and calculated magnetic field strength are considered as the objective functions where both errors are required to be minimum. Since both error criteria do not

often become minimum simultaneously, a set of errors will be obtained from the optimisation process, and their corresponding feedback coefficient and squareness are stored. From this set, the required feedback and squareness can be selected so that both errors remain within certain levels. The equations of relative loss error and root mean square of error are given below:

$$\varepsilon_{\mathrm{r}} = \left| \frac{P_{\mathrm{mea}} - P_{\mathrm{cal}}}{P_{\mathrm{mea}}} \right| \times 100\% \tag{3.34}$$

$$\varepsilon_{\mathrm{s}} = \frac{1}{\max\left(H_{\mathrm{meai}}\right)} \sqrt{\sum_{i}^{N} \frac{\left(H_{\mathrm{meai}} - H_{\mathrm{i}}\right)^2}{N}} \times 100\% \tag{3.35}$$

where ε_{r} is the relative core loss error, ε_{s} the root mean square error between measured and calculated H, P_{mea} is the measured core loss, P_{cal} is the calculated core loss, N the number of samples per cycle, and H_{meai} and H_{i} the measured and calculated magnetic field strength, respectively. The calculated squareness with the change of peak magnetic flux density is shown in Fig. 3.13(a). Then, the calculated squareness and feedback coefficient can be exploited for implementation of the generalised inverse Preisach model. In the same way, the optimisation technique can also be applied for calculation of squareness and feedback coefficient of the generalised Preisach model. In this case, the squareness depends on the peak magnetic field strength which is shown in Fig. 3.13(b).

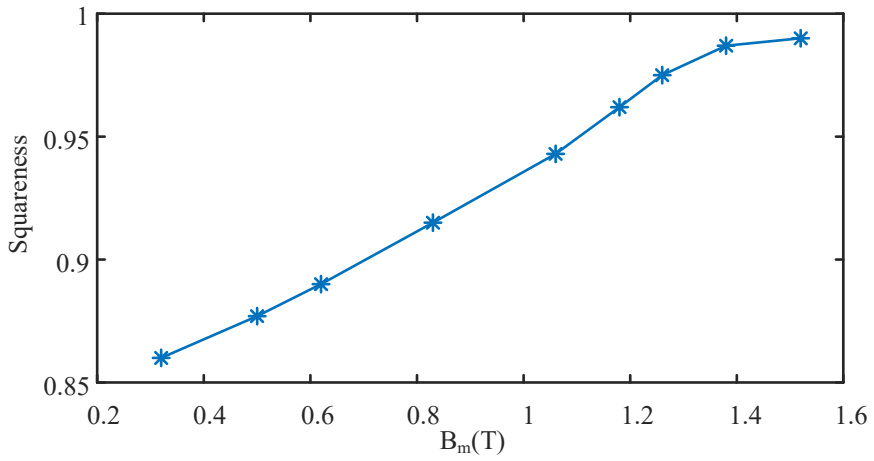

(a)

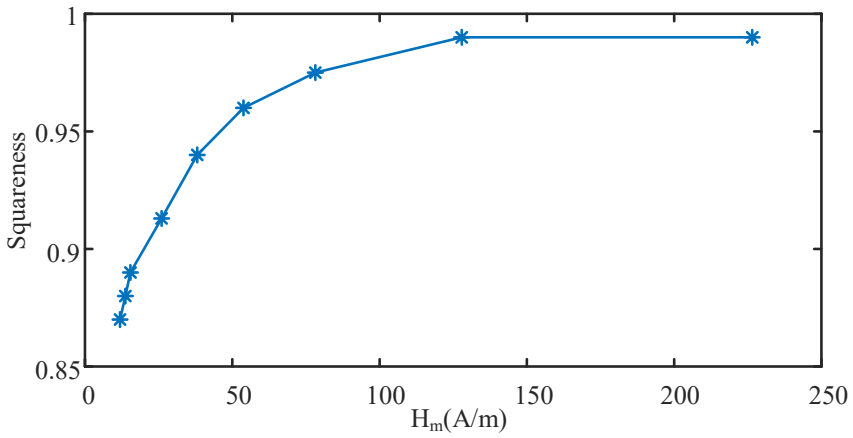

(b)

Fig. 3.13. Variable squarenesses for inverse and direct Preisach model with: (a) maximum magnetic flux density, and (b) maximum magnetic field strength, respectively.

However, variable squareness with constant feedback based generalised inverse Preisach model is only studied for static hysteresis model. For consideration of dynamic core loss and minor loop, the early mentioned variable feedback coefficient with constant squareness based generalised inverse model is mainly considered in this chapter.

3.7 Dynamic Hysteresis Effects

The abovementioned Preisach and inverse Preisach models can only predict the static hysteresis loss. If the excitation frequency increases, the other core loss components, such as the eddy current and excess losses, which are also known as dynamic losses, have to be considered for calculating the total core loss. According to the Domain model, the eddy current losses are produced by micro-eddy currents induced at the vicinity of moving domain walls [3.6], [3.31]. Since the ribbon of amorphous magnetic material is very thin, the total eddy current loss is significantly smaller than those in silicon steel sheets. For simplicity, in the low and medium frequency range, the eddy current paths can be considered as global, which is known as the classical eddy current model [3.6], [3.31]. Thus, according to the classical model, the magnetic field strength due to the eddy current can be obtained by [3.30]

$$H_{eddy} = \frac{\sigma d^2}{12}\frac{\Delta B}{\Delta t} \tag{3.36}$$

where σ and d are the conductivity and thickness of the amorphous ribbon, respectively, and ΔB is the change of magnetic flux density between two successive discrete time steps. Similarly, the magnetic field strength corresponding to the excess loss can be expressed as follows [3.30], [3.23]:

$$H_{exc} = \sqrt{\sigma G V_0 A_l}\,\frac{\Delta B}{\Delta t^{0.5}\left|\Delta B\right|^{0.5}} = K_{exc}\,\frac{\Delta B}{\Delta t^{0.5}\left|\Delta B\right|^{0.5}} \tag{3.37}$$

where A_l is the cross-sectional area of the ribbon, G and V_0 are constant coefficients depending on the material metallurgical properties, and K_{exc} is equal to the square root of the product of A_l, G, V_0 and σ.

3.7.1 Identification of Dynamic Coefficients

While the eddy loss parameters (σ and d) can be easily obtained from measurement or the data sheet provided by manufactures, the measurement of excess loss parameters, A_l, G, and V_0 are very difficult to be found out**.** Instead, K_{exc}, which is the square root of the product of A_l, G, V_0 and σ, can be calculated directly using curve fitting technique. In the curve fitting technique, the measured core losses per unit volume per cycle under sinusoidal excitations of different frequencies (starting form 1 Hz or less than 1 Hz) at the same magnetic flux density is curve-fitted. According to loss separation approach, the total loss, which is the sum of hysteresis, eddy and excess losses, can be expressed by using following equation [3.23]:

$$P_t = P_h + \frac{\sigma \pi^2 d^2}{6} B_m^2 f^2 + 8.76 K_{exc} B_m^{1.5} f^{1.5} \tag{3.38}$$

where P_t is the total core loss per unit volume, and the first, second and third terms on the right-hand side are the hysteresis (P_h), eddy current and excess losses per unit volume, respectively. Fig. 3.14 shows the curve fitting of the measured core losses per cycle (P_t/f) with f for two different maximum magnetic flux densities. The separation of the hysteresis and eddy and excess losses from the total loss is also observed in Fig. 3.14. From the Fig. 3.14, it is also observed that the effect of eddy current is smaller than those of the

hysteresis and excess losses. However, both eddy current and excess losses per cycle increases with frequency.

To achieve high accuracy K_{exc}, the procedure can be repeated for different magnetic flux densities, and the average K_{exc} is finally considered.

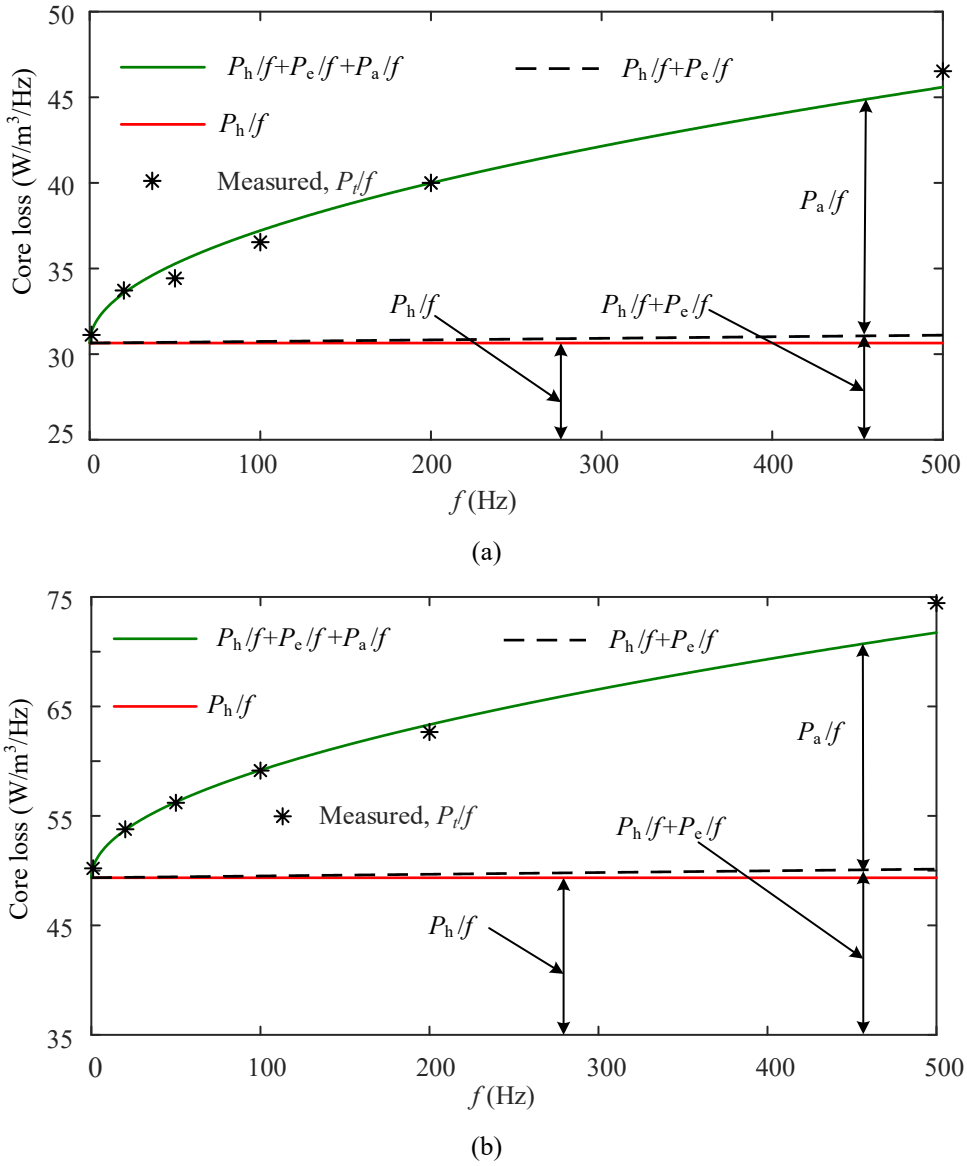

Fig. 3.14. Curve fitting of the measured core loss data with frequency for different maximum magnetic flux densities, e.g. (a) 1.08 T, and (b) 1.41 T.

3.7.2 Incorporation of Dynamic Hysteresis with Inverse Preisach Model

To incorporate the dynamic effects into the generalised inverse Preisach model, the magnetic field strength related to the static hysteresis loss is firstly calculated by the generalised inverse Preisach model, and the magnetic field strengths corresponding to the eddy current and excess losses are then calculated by (3.36) and (3.37), respectively. The total magnetic field strength is finally obtained by summing up all these components of magnetic field strength.

3.8 Experimental Verification

This section presents the experimental verification of different existing and proposed models. In addition, comparisons among different models are also presented in this section.

3.8.1 Experimental Testing Method

Fig. 3.15 shows a test platform for measuring the hysteresis effects of the Fe-based amorphous material sample, where the testing set up is based on [3.32] and [3.33]. The ring core sample of the selected amorphous magnetic material, which is obtained from Guangzhou Amorphous Electronic Technology Co. Ltd., China [3.34], is wound with two coils of equal number of turns, known as the excitation and search coils, respectively. Table 3.1 lists the different dimensions of core sample and number of turns of the coils. The Labview software is utilised for excitation source and data acquisition. A power amplifier is utilised to control both the excitation voltage and power levels. The excitation current is obtained by measuring the voltage drop (v_R) across a resistor of 1 , which is connected in series with the excitation coil. Similarly, the magnetic flux density is derived by measuring the induced electromotive force (*emf*) in the search coil. The measured data are stored in XLS files and processed by a MATLAB program.

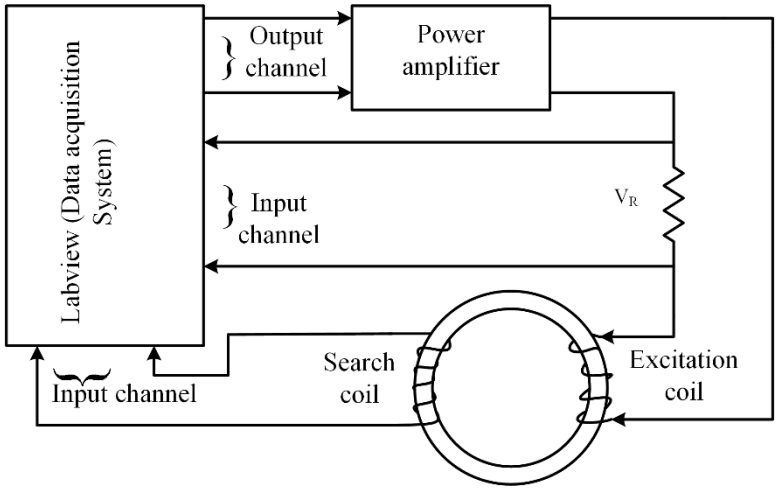

Fig. 3.15. Block diagram of the experimental set up for measuring *B*-*H* loops of magnetic materials.

Table 3.1

Different parameters of the tested core

Parameters	**Values**
Material name	Fe-based amorphous (1k101) [3.9], [3.34]
Core type	Toroidal
Thickness (mm)	0.023 ~ 0.026
Height (mm)	30
Outer diameter (mm)	63
Inner diameter (mm)	45
Stacking factor	0.80
Mass density (kg/m3)	7180
Resistivity μ . cm	130
Number of turns of coils	24/24

The magnetic field strength is obtained from the excitation current as follows [3.6]:

$$H(t) = \frac{N_{ex} i_{ex}(t)}{l_m} \tag{3.39}$$

where i_{ex} is the excitation current, l_m the mean length of magnetic core, and N_{ex} the number of turns of excitation coil.

The magnetic flux density is calculated by integrating the induced *emf* in the search coil with respect to time which is as follows:

$$B(t) = \frac{1}{N_s A_c} \int v_s(t) dt \tag{3.40}$$

where A_c is the effective cross-sectional area of magnetic core, v_s the induced *emf*, and N_s the number of turns of search coil.

Finally, the core loss per unit volume (P) can be calculated by

$$P = \frac{1}{T} \int_T H \frac{dB}{dt} dt \tag{3.41}$$

The unit of the abovementioned equation of the total core loss is W/m^3. If the unit is replaced by W/kg, the right side of (3.41) needs to be divided by the mass density of the magnetic material.

For minor loops, a voltage of 1 Hz fundamental sinusoidal component with a third harmonic component is used as the excitation voltage [3.6]. A proportional integral controller is also integrated with the experimental set up to control the size and position of the minor loops. Fig. 3.16 shows an experimental *B*-*H* loop which contains two minor loops on a major loop.

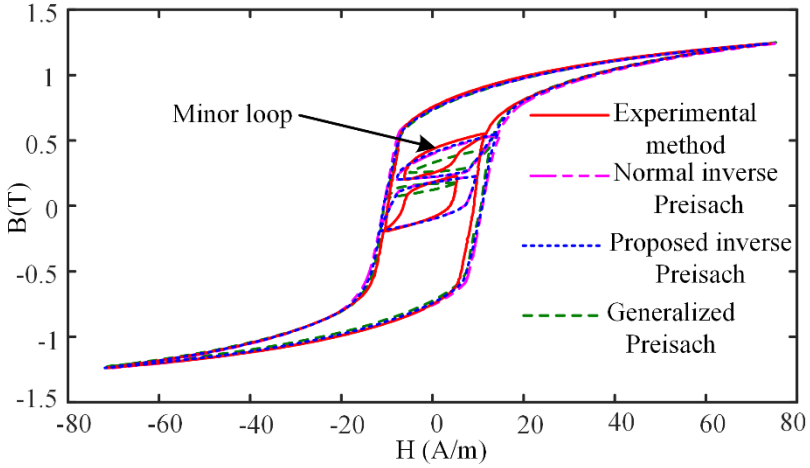

Fig. 3.16. Comparison among measured and calculated *B*-*H* loops for minor loops over a major loop.

3.8.2 Verification of Simulated Results

For verification of the empirical model, the calculated core losses are compared with the experimentally measured core losses as shown in Fig. 3.17. From the figure, it is observed that the mismatch between measured and calculated losses at initial and ending areas of considered frequency range is higher than that obtained at middle of the frequency range.

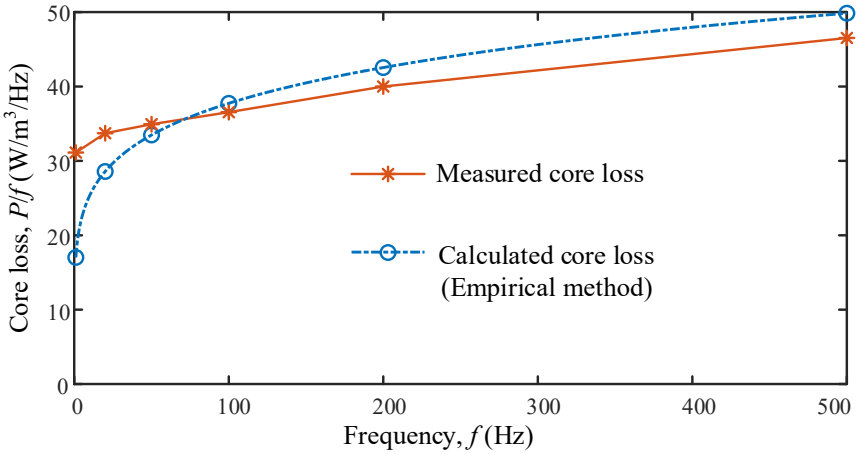

Fig. 3.17. Comparison between measured and calculated power losses per cycle at 1.08 T.

For verification of the Preisach model, the waveform of magnetic flux density is firstly calculated from a given magnetic field strength waveform as shown in Fig. 3.3 (Section 3.5.1). From the figure, it is seen that there is a good agreement between calculated and measured magnetic flux densities. The hysteresis losses at different magnetic flux densities are firstly calculated by the normal and generalised Preisach models, and then compared to the experimentally measured results which are listed in Table 3.2(a) and Table 3.2(b), where the unit of hysteresis loss in Table 3.2(a) is W/m^3/Hz, and the unit in Table 3.2(b) is W/kg/Hz. From Table 3.2, the following three important observations can be made:

(i) The calculated and measured losses are very close to each other although the discrepancy increases at a low magnetic flux density since the magnetic coercive forces at low flux density are significantly smaller than that of the limiting loop.

(ii) The generalised Preisach model provides a significantly higher precision in calculating the hysteresis loss than that of the normal Preisach model, especially at low magnetic flux densities.

(iii)The hysteresis loss calculated by the proposed feedback coefficient has lower error at a low magnetic flux density than that obtained by the constant feedback coefficient. This can also be seen from Fig. 3.8 that at the vicinity of H_c, the magnetic flux density calculated by using the proposed feedback coefficient is closer to the experimental result than that obtained by using constant feedback coefficient (K= -1.29113×10^{-6}).

Table 3.2 (a)
Comparison of calculated and measured hysteresis loss (W/m^3/Hz) for Preisach models

B_m (T)	**Test**	**Normal Preisach**		**Generalised Preisach**			
				***Proposed K* (B_m)**		***Constant K***	
	P_h (W/ m^3/Hz)	P_h (W/ m^3/Hz)	*Error* (%)	P_h (W/ m^3/Hz)	*Error* (%)	P_h (W/ m^3/Hz)	*Error* (%)
0.83	21.00	28.40	35.24	26.13	24.43	27.73	32.05
1.06	31.24	33.51	7.27	32.12	2.82	32.76	4.87
1.18	37.41	38.03	1.66	37.24	-0.45	37.51	0.27
1.26	42.52	43.30	1.83	41.98	-1.27	42.48	-0.09
1.38	50.38	51.40	2.02	50.09	-0.57	50.56	0.36
1.52	63.22	66.14	4.62	64.64	2.25	65.51	3.62

Table 3.2 (b)
Comparison of calculated and measured hysteresis loss (W/kg/Hz) for Preisach models

B_m (T)	**Test**	**Normal Preisach**		**Generalised Preisach**			
				***Proposed K* (B_m)**		***Constant K***	
	P_h (W/ kg/Hz)	P_h (W/ kg/Hz)	*Error* (%)	P_h (W/ kg/Hz)	*Error* (%)	P_h (W/ kg/Hz)	*Error* (%)
0.83	0.002925	0.003955	35.24	0.003639	24.43	0.003862	32.05
1.06	0.004351	0.004667	7.27	0.004474	2.82	0.004563	4.87
1.18	0.005210	0.005297	1.66	0.005187	-0.45	0.005224	0.27
1.26	0.005922	0.006031	1.83	0.005847	-1.27	0.005916	-0.09
1.38	0.007017	0.007159	2.02	0.006976	-0.57	0.007042	0.36
1.52	0.008805	0.009212	4.62	0.009003	2.25	0.009124	3.62

Similar to Table 3.2, Table 3.3 lists a comparison of the hysteresis losses at different magnetic flux densities obtained by the normal and generalised inverse Preisach models with the measured results. The unit of hysteresis loss in Table 3.3(a) is W/m^3/Hz and the unit in Table 3.3(b) is W/kg/Hz. From Table 3.3, the following three observations can be made:

(i) The generalised inverse Preisach model with the proposed feedback coefficient shows better agreement with the measured results than the normal inverse Preisach model and generalised inverse Preisach model with constant feedback coefficient.

(ii) The error decreases with the increase of magnetic flux density.

(iii) The calculation of maximum magnetic field strengths by both inverse Preisach models are almost the same, and both are close to the measure result. For instance, the calculated maximum magnetic field strength by the normal and proposed inverse Preisach models at 1.26 T are 76.95 A/m and 75.83 A/m, respectively, whereas the measured magnetic field strength is 78.19 A/m.

Fig. 3.18 shows the comparison of hysteresis losses obtained from generalised inverse Preisach model with variable squareness and constant squareness along with the constant feedback coefficient. It is observed from Fig. 3.18 that variable squareness based generalised inverse Preisach model shows better performance than the constant squareness based generalised inverse Preisach model. It happens because the accuracy of generalised inverse Preisach model generally increases with increase of the magnetic induction levels. In the same way, with increase of squareness, the accuracy of the model increases especially in the range of 1 T to 1.4 T.

Table 3.3(a)
Comparison of calculated and measured hysteresis loss (W/m^3/Hz) for inverse Preisach models

B_m (T)	**Test**	**Normal inverse Preisach**		**Generalised inverse Preisach**			
				Proposed K		***Constant K***	
	P_h (W/ m^3/Hz)	P_h (W/ m^3/Hz)	*Error* (%)	P_h (W/ m^3/Hz)	*Error* (%)	P_h (W/ m^3/Hz)	*Error* (%)
0.83	21.00	27.21	29.57	25.12	19.62	27.16	29.33
1.06	31.24	35.76	14.47	34.03	8.93	35.75	14.44
1.18	37.41	41.54	11.04	39.61	5.88	41.50	10.93
1.26	42.52	44.88	5.55	42.89	0.87	44.71	5.15
1.38	50.38	51.09	1.41	48.72	-3.29	50.95	1.13
1.52	63.22	67.64	6.99	63.94	1.34	67.41	6.62

Table 3.3(b)
Comparison of calculated and measured hysteresis loss (W/kg/Hz) for inverse Preisach models

B_m (T)	Test	Normal inverse Preisach		Generalised inverse Preisach			
				Proposed K		***Constant K***	
	P_h (W/kg/Hz)	P_h (W/kg/Hz)	*Error* (%)	P_h (W/kg/Hz)	*Error* (%)	P_h (W/kg/Hz)	*Error* (%)
0.83	0.002925	0.003790	29.57	0.003499	19.62	0.003783	29.33
1.06	0.004351	0.004981	14.47	0.004740	8.93	0.004979	14.44
1.18	0.005210	0.005786	11.04	0.005517	5.88	0.005780	10.93
1.26	0.005922	0.006251	5.55	0.005974	0.87	0.006227	5.15
1.38	0.007017	0.007116	1.41	0.006786	-3.29	0.007096	1.13
1.52	0.008805	0.009421	6.99	0.008905	1.34	0.009389	6.62

Furthermore, the prediction accuracies of hysteresis loss of both the normal and generalised inversed Preisach models depend significantly on the number of sampling points of magnetic flux density per cycle. For instance, if the number of sampling points of magnetic flux density per cycle is increased from 500 to 1000, the error of hysteresis loss calculation at 1.18 T by generalised inversed Preisach model can be reduced from 8.50% to 5.88%.

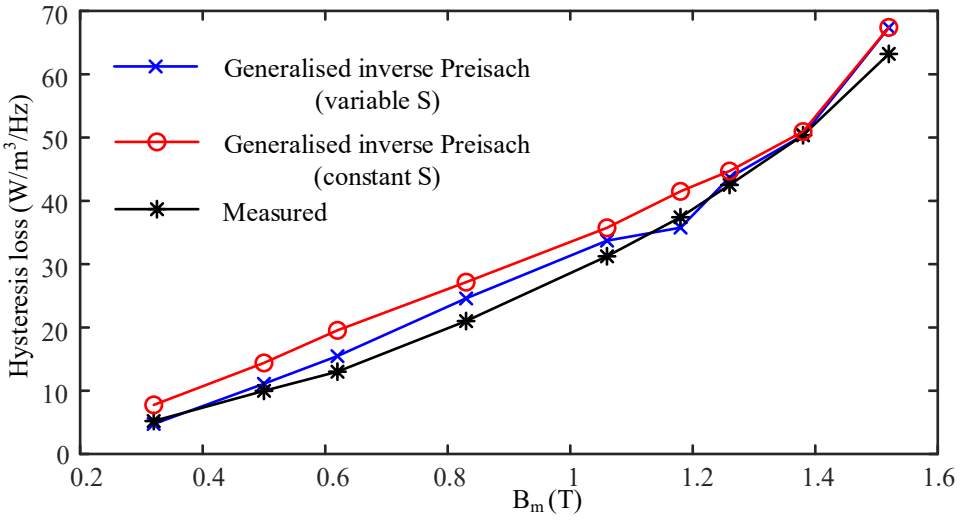

Fig. 3.18. Comparison of calculated and measured hysteresis loss using inverse Preisach models with different squareness conditions.

When the minor loops are considered on a major loop, the discrepancy between the calculated and experimental results increases slightly, as shown in Figs. 3.11 and 3.16, due to the following reasons: (i) the congruent property of the normal Preisach model,

although for the generalised Preisach model the congruent property has been relaxed [3.15]; (ii) the low incremental magnetic field strength as the discrepancy between the calculated and experimental results increases at low magnetic field strength [3.28]; (iii) further deviation occurs if the minor loops happen at the vicinity of magnetic coercive force for the reason discussed in Section 3.5.2.3. However, a significant improvement in the calculation of hysteresis loss is obtained by the proposed inverse Preisach model in comparison to the normal inverse Preisach model. Table 3.4 lists a comparison of the calculated and measured hysteresis losses with minor loops. As shown in Table 3.4, the errors in the calculation of hysteresis loss at 1.24 T by the proposed and the normal inverse Preisach models are 7.24% and 11.55%, respectively.

Table 3.4
Comparison of calculated and measured hysteresis loss with minor loops

P_h (Test) ($W/m^3/Hz$)	**Normal inverse Preisach**		**Generalised inverse Preisach**	
	P_h ($W/m^3/Hz$)	*Error*	P_h ($W/m^3/Hz$)	*Error*
46.67	52.06	11.55%	50.05	7.24%

In the case of dynamic hysteresis losses, the losses are calculated by the normal and proposed inverse Preisach models at the same magnetic flux density with different frequencies. The calculated and experimental results are then curve fitted and compared with each other, as shown in Fig. 3.19 (a) and 3.19(b), where the unit of core loss per cycle in Fig. 3.19 (a) is $W/m^3/Hz$, and the unit in Fig. 3.19 (b) is W/kg/Hz. It is observed from Fig. 3.19 that the results calculated by the proposed generalised inverse Preisach model are closer to the measured results than those by the normal inverse Preisach model. On the other hand, both inverse Preisach models show better agreement with the experimental results than those obtained by empirical model.

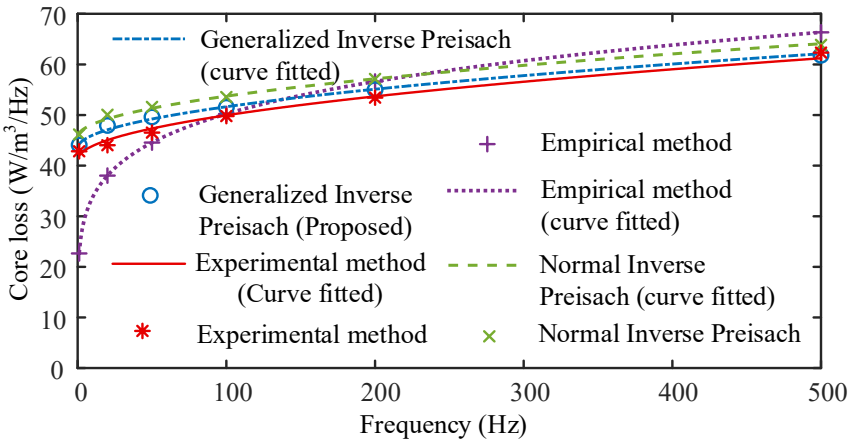

(a)

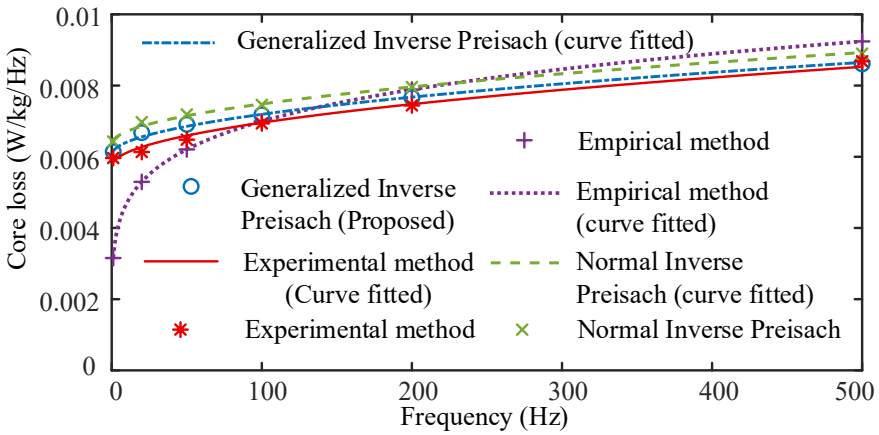

(b)

Fig. 3.19. A comparison between calculated and measured core losses versus frequency at B_m=1.29 T with two different loss units: (a) W/m^3/Hz and (b) W/kg/Hz.

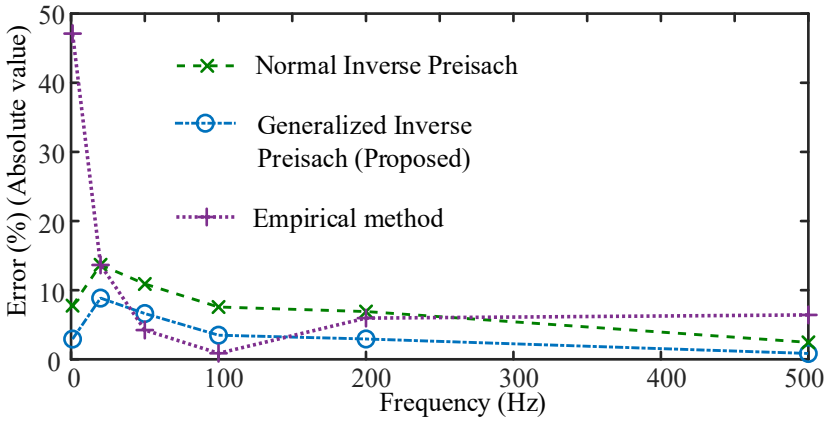

Fig. 3.20. A comparison of errors in calculation of core loss using different models.

Fig. 3.20 shows the percentage of errors for different calculated points obtained by the various models. It is observed from the figure that the accuracy of the proposed

generalised inverse Preisach model is higher than those of other two models. In addition, the percentage of error in the calculation of core loss by the proposed generalised inverse Preisach model decreases with the increase of the frequency.

The experimental and calculated *B-H* loops of the Fe-based amorphous magnetic material at 500 Hz are shown in Fig. 3.21. From the figure, it is observed that the calculated *B-H* loop by the proposed model is very close to the measured loop. However, the *B-H* loop becomes small when the excess loss is excluded from the core loss. On the other hand, when both the eddy current and excess losses are excluded, i.e. if only hysteresis loss is considered, the *B-H* loop seems similar to the loop that considers both hysteresis and eddy current losses. The reason for this similarity is that the effects of eddy current loss in the amorphous sample are not as significant as those in the conventional magnetic materials, e.g. SiFe sheets, since the thickness of the ribbon of Fe-based amorphous magnetic material sample is much thinner than those of SiFe sheets [3.35].

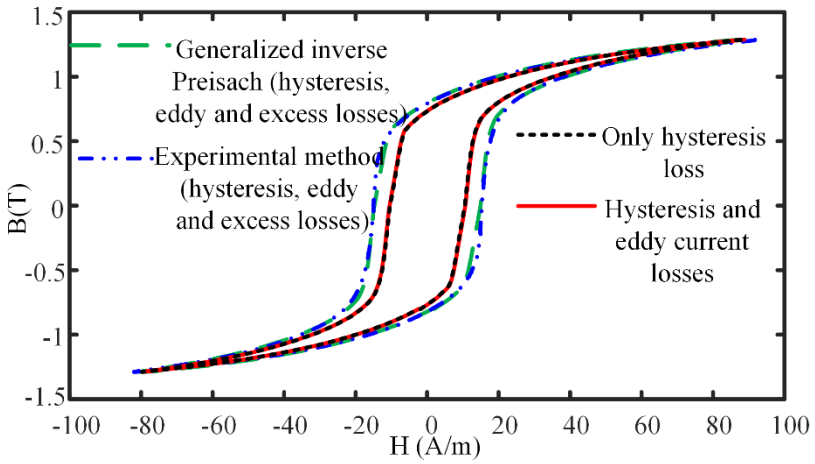

Fig. 3.21. Calculated and measured *B-H* loops at 500 Hz and 1.29 T.

3.9 Conclusion

A generalised inverse Preisach dynamic hysteresis model is proposed in this chapter for characterisation of the Fe-based amorphous magnetic materials. The proposed model incorporates the reversible magnetisation component into the Preisach elemental operator and magnetisation dependent feedback coefficient that are missing in the existing types of inverse Preisach models, and thus can accurately characterise the dynamic performance of magnetic cores of the Fe-based amorphous magnetic materials for both low and

medium frequency applications. The theoretical derivation and numerical implementation of the proposed model are presented in details based on discussions of the existing normal Presiach model, generalised Preisach model, and normal inverse Preisach model. The theoretical results of the proposed and existing inverse Preisach models are compared with the experimental measurement results. The proposed model has demonstrated higher accuracy than the normal inverse Preisach model for the cases of both major loops and major loop plus minor loops under different excitation magnitudes as well as frequencies. However, inverse Preisach models are not only capable of calculation of magnetic field strength from magnetic flux density but also provides better prediction of iron loss than empirical model.

References

[3.1] K. Venkatachalam, C. R. Sullivan, T. Abdallah, and H. Tacca, "Accurate prediction of ferrite core loss with nonsinusoidal waveforms using only Steinmetz parameters," *in Proc. IEEE Workshop Comp. Power Electron.*, Mayaguez, Puerto Rico, USA, pp. 36–41, Jun. 3–4, 2002.

[3.2] S. Hussain and D. A. Lowther, "The Modified Jiles–Atherton Model for the accurate prediction of iron losses," *IEEE Trans. Magn.*, vol. 53, no. 6, Jun. 2017, Art no. 7300504.

[3.3] I. D. Mayergoyz, Mathematical models of hysteresis, Springer-Verlag, 1991.

[3.4] I. D. Mayergoyz and G. Friedman, "The Preisach model and hysteresis energy losses," *J. Appl. Phys*., vol. 61, pp. 3910-3912, 1987.

[3.5] A. Ivanyi, Hysteresis models in electromagnetic computation, Akademiai Kiado, Budapest, Hungary, 1997.

[3.6] J. G. Zhu, Numerical modelling of magnetic materials for computer aided design of electromagnetic devices, Ph.D. Dissertation, School of Electrical Engineering, University of Technology Sydney, Australia, July 1994.

[3.7] E. D. Torre, "Magnetization calculation of fine particles," *IEEE Trans. Mag*., vol. 22, no. 5, pp. 484-489, Sep. 1986.

[3.8] Y. D. Yan and E. D. Torre, "Particle interaction in numerical micromagnetic modelling, *J. Appl. Phys*., vol. 67, pp. 5370-5372, 1990.

[3.9] Henan ZY Amorphous Technology Co. Ltd. Available: https://www.zyamorphous.com/. (Accessed: September 25, 2019).

[3.10] M. R. Islam, G. Lei, Y. Guo, and J. Zhu, "Optimal design of high-frequency magnetic links for power converters used in grid-connected renewable energy systems," *IEEE Trans. Magn*., vol. 50, no. 11, Nov. 2014, Art. 2006204.

[3.11] A. Benabou, J. V. Leite, S. Clénet, C. Simão, and N. Sadowski, "Minor loops modelling with a modified Jiles–Atherton model and comparison with the Preisach model," *J. Mag. Mag. Mats.*, vol. 320, no. 20, pp. e1034–e1038, Oct. 2008.

[3.12] G. Kadar and E. D. Torre, "Hysteresis modeling: I. Non-congruency," *IEEE Trans. Magn.*, vol. 23, no. 5, pp. 2820–2822, Sep. 1987.

[3.13] E. D. Torre, “Existence of magnetization-dependent Preisach models,” *IEEE Trans. Magn.*, vol. 27, no. 4, pp. 3697–3699, July 1991.

[3.14] J. Oti, F. Vajda, and E. D. Torre, “Identification of parameters in a moving model,” *J. appl. Phys*., vol. 69, no. 8, pp. 4826–4828, Apr. 1991.

[3.15] F. Vajda and E. Della Torre, “Efficient numerical implementation of complete-moving-hysteresis models,” *IEEE Trans. Magn.*, vol. 29, no. 2, pp. 1532–1537, Mar. 1993.

[3.16] Z. Szabó and J. Füzi, “Implementation and identification of Preisach type hysteresis models with Everett Function in closed form,” *J. Magn. Magn. Mater.* vol. 406, pp. 251–258, May 2016.

[3.17] Y. Cao, K. Xu, W. Jiang, T. Droubay, P. Ramuhalli, D. Edwards, B. R. Johnson, J. McCloy, “Hysteresis in single and polycrystalline iron thin films: major and minor loops, first order reversal curves, and Preisach modeling,” *J. Magn. Magn. Mater.* vol. 395, pp. 361–375, 2015.

[3.18] D. Atherton, B. Szpunar, and J. Szpunar, “A new approach to Preisach diagrams,” *IEEE Trans. Magn.*, vol. 23, no. 3, pp. 1856–1865, May 1987.

[3.19] I. D. Mayergoyz and G. Friedman, “Generalized Preisach model of hysteresis,” *IEEE Trans. Magn.*, vol. 24, no. 1, pp. 212–217, Jan. 1988.

[3.20] I. D. Mayergoyz, “Dynamic Preisach models of hysteresis,” *IEEE Trans. Magn.*, vol. 24, no. 6, pp. 2925–2927, Nov. 1988.

[3.21] Y. Bernard, E. Mendes, and F. Bouillault, “Dynamic hysteresis modeling based on Preisach model,” *IEEE Trans. Magn.*, vol. 38, no. 2, pp. 885–888, Mar. 2002.

[3.22] E. Cardelli, E. D. Torre, and B. Tellini, “Direct and inverse Preisach modeling of soft materials,” *IEEE Trans. Magn.*, vol. 36, no. 4, pp. 1267–1271, Jul. 2000.

[3.23] E. Fallah and J. S. Moghani, “A new approach for finite-element modeling of hysteresis and dynamic effects,” *IEEE Trans. Magn.*, vol. 42, no. 11, pp. 3674–3681, Nov. 2006.

[3.24] C. P. Steinmetz, “On the law of hysteresis,” *Trans. American Ins. Elect. Engr.*, no. 1, pp. 1–64, Jan. 1892.

[3.25] L. Evangelista, M. A. Carvalho, and P. A. P. Wendhausen, “Steinmetz coefficients’ prediction based on processing parameters of soft magnetic composites,” *IEEE Trans. Magn.*, vol. 56, no. 2, pp. 1-5, Feb. 2020, Art no. 2000205.

[3.26] L. R. Dupré, R. V. Keer, and J. A. A. Melkebeek, “Evaluation of magnetostrictive effects in soft magnetic materials using the Preisach theory,” *J. Magn. Magn. Mater.,* vol. 254–255, pp. 121–123, Jan. 2003.

[3.27] S. Y. R. Hui and J. Zhu, “Numerical modelling and simulation of hysteresis effects in magnetic cores using transmission-line modelling and the Preisach theory,” *IEE Proc. – Elect. Pow. Appls*., vol. 142, no. 1, pp. 57–62, Jan. 1995.

[3.28] S. R. Naidu, “Simulation of the hysteresis phenomenon using Preisach's theory,” *IEE Proc. A Phy. Sci. Mea. Inst. Man. Edu.,* vol. 137, no. 2, pp. 73–79, Mar. 1990.

[3.29] J. G. Zhu, S. Y. R. Hui, and V. S. Ramsden, “A dynamic equivalent circuit model for solid magnetic cores for high switching frequency operations,” *IEEE Trans. Power Electron*., vol. 10, no. 6, pp. 791–795, Nov. 1995.

[3.30] N. Sadowski, N. J. Batistela, J. P. A. Bastos, and M. Lajoie-Mazenc, “An inverse Jiles-Atherton model to take into account hysteresis in time-stepping finite-element calculations,” *IEEE Trans. Magn.*, vol. 38, no. 2, pp. 797–800, Mar. 2002.

[3.31] C. R. Boon and J. A. Robey, “Effect of domain-wall motion on power loss in grain-oriented silicon-iron sheet,” *Proc. IEE.*, vol. 115, no. 10, pp. 1535–1540, 1968.

[3.32] P. Kis, M. Kuczmann, J. Fuzi, and A. Ivanyi, “Hysteresis measurement in LabView”, *Pysica B: Cond. Matt.*, vol. 343, no. 1–4, Jan. 2004.

[3.33] S. Y. R. Hui, J. G. Zhu, and V. S. Ramsden, “A generalized dynamic circuit model of magnetic cores for low- and high-frequency applications. II. Circuit model formulation and implementation,” *IEEE Trans. Power Electron.*, vol. 11, no. 2, pp. 251–259, Mar. 1996.

[3.34] Guangzhou Amorphous Electronic Technology Co. Ltd. [Online]. Available: https://www.coilcore.com/. (Accessed: December 22, 2019)

[3.35] A. Krings, M. Cossale, A. Tenconi, J. Soulard, A. Cavagnino, and A. Boglietti, “Magnetic materials used in electrical machines: a comparison and selection guide for early machine design,” *IEEE Ind. Appl. Mag.,* vol 23, no. 6, pp. 21–28, Nov.- Dec. 2017.

Chapter 4 Modelling of Amorphous Magnetic Material Using Jiles-Atherton Model

4.1 Introduction

In the previous chapter, empirical as well as direct and inverse Preisach model are utilised to characterise the selected Fe-based amorphous magnetic material. In this chapter, another characterisation tool named J-A model is used to model the magnetic material. The J-A models [4.1]−[4.9] can also be capable to present the nonlinear properties of magnetic material, and requires less computational time and memory resources compared to Preisach model [4.1], [4.8]. Depending on whether the orientation of the applied magnetic field varies, the J-A models can be classified into the scalar J-A model and vector J-A model [4.10]. In this chapter, the scalar J-A model is considered to characterise the selected Fe-based amorphous magnetic material named amorphous 1k101 [4.11], [4.12] under the alternating magnetic excitation that varies with time in a fixed orientation.

The original J-A model consists of some equations which are mainly equations of magnetisation susceptibility with respect to the applied magnetic field strength, irreversible magnetisation susceptibility with respect to effective magnetic field strength, reversible and anhysteretic magnetisations, and the effective magnetic field strength. The J-A model equations generally need to be identified some model parameters which are pinning coefficient or loss factor k, reversibility coefficient c, domain interaction α, anhysteretic magnetisation's shape parameter a, and saturation magnetisation M_s [4.4]–[4.7]. In the original J-A model [4.4]–[4.6], all model parameters are considered as constants for the whole range of magnetic induction levels. Different researchers [4.1], [4.13] later observed that the pinning parameter or loss parameter k depends on the magnetic induction levels. After considering the loss factor as a function of B or H, the modelling of magnetic core shows higher agreement between measured and calculated waveform of B or H than that with the constant loss factor k. In the same way, it was also observed that at low magnetic induction levels, the J-A model produces more error in calculation of core loss as well as higher difference between experimental and calculated waveform of B or H than those at high magnetic induction levels [4.14]–[4.16]. The main

reason for these high discrepancies at low magnetic induction levels is that model parameters are calculated based on a large *B*-*H* loop, and consequently the rate of reversible magnetisations at low magnetic induction levels becomes larger than its actual values. To reduce the rate of the reversible magnetisation, a scaling factor, which can be a constant value or the function of *B* or *H* depending on the input of the model, is incorporated into the equation of rate of change of reversible magnetisation [4.14]–[4.16]. Therefore, both calculated iron loss and calculated *B* or *H* show better agreement with experimental results. Recently, the authors of [4.3] considered both variable loss factor *k* and variable scaling factor *R* in the J-A model which gives higher agreement between experimental and calculated results than the one in a situation where they are constant values or one of them keep constant and another is variable.

The model parameters are initially calculated by solving some equations which are based on model equations at some specific conditions on a large *B*-*H* loop of a magnetic material [4.5], [4.6], [4.17]. The problem of the initial methods is that they provide the low accuracy in the calculations of *B* or *H* and iron loss. Later different optimisation techniques [4.13], [4.15], [4.18]–[4.20] such as genetic algorithm, stimulated annealing and particle swarm optimisation are utilised to obtain the model parameters, which improve the accuracy of the J-A model. The optimisation techniques as well as other similar methods [4.1], [4.7] are actually exploited in such a way that the error becomes the minimum. The different error criteria [4.1], [4.7], [4.13], [4.19], [4.21], [4.22] such as the mean error, or mean square error or root mean square error between experimental and calculated *B* or *H* are generally used in the optimisation techniques. Among different error criteria, the root mean square is widely used to identify the model parameters. The identified model parameters are then used for calculation of *B*-*H* loop, and the iron loss is finally calculated from the calculated *B*-*H* loop. The detailed analysis of measured and calculated *B*-*H* loop shows that the minimum relative error in the iron loss calculation does not often occur simultaneously with the minimum root mean square error of calculated *B* or *H*. It is also observed that with a slight increase of root mean square of error between calculated and experimental waveform of *B* or *H*, the relative error of the calculation of iron loss reduces significantly. Therefore, in the optimisation techniques double error criteria, where one is based on the conventional root mean square of error and the other is based on the relative iron loss error, can be a good technique for high

accuracy of iron loss calculation along with satisfactory calculated waveform of B or H. In this study, Brute Force algorithm-based optimisation [4.23] is utilised to identify the model parameters. The advantages of the Brute Force optimisation method are that the method is easily executed, and does not require derivative evaluation or any sophisticated intelligent techniques.

If the root mean square error of calculated B or H slightly increases, the error in the calculation of coercive magnetic force (H_c) increases a bit. To improve the calculation of H_c as well as B or H, a scaling factor can be included in the anhysteretic magnetisation instead of its general inclusion into the equation of the rate of change of reversible magnetisation. The inclusion of the scaling factor in the anhysteretic magnetisation simultaneously reduces the rate of irreversible magnetisation and anhysteretic magnetisation, and consequently it provides better agreement between experimental and calculated results than the existing inclusion way of scaling factor.

In this chapter, the selected Fe-based amorphous magnetic material is characterised by a modified J-A model. The main contributions of the study include incorporation of an additional error criterion along with general error criterion for the identification of the J-A model parameters, and inclusion of a scaling factor in the anhysteretic magnetisation of original J-A model in order to reduce the rate of irreversible magnetisation and anhysteretic magnetisation especially at the low magnetic induction levels. Dynamic models, which signify the eddy current and excess loss models, are later incorporated with the static modified J-A model to make the model generalised. The proposed method of parameter identification and proposed modified J-A model are examined by comparing the calculated results with experimental as well as recently publish works in the literature.

4.2 Jiles-Atherton model

The implementation process of the J-A model for characterisation of magnetic materials can be divided into two parts: formulation of J-A model and identification of J-A model parameters which are discussed in the next two subsections.

4.2.1 Formulation

It is already discussed that J-A model consists of a set of equations which are given below [4.2], [4.5], [4.6], [4.17]:

$$\frac{dM_{irr}}{dH_e} = \frac{\left(M_{an} - M_{irr}\right)}{k\delta} \tag{4.1}$$

$$M_{rev} = c\left(M_{an} - M_{irr}\right) \tag{4.2}$$

$$M_{irr} = \frac{M - cM_{an}}{1-c} \tag{4.3}$$

$$M_{an} = M_s\left[\coth\frac{H_e}{a} - \frac{a}{H_e}\right] \tag{4.4}$$

$$\frac{dM}{dH} = \frac{(1-\mathrm{c})\frac{dM_{irr}}{dH_e} + c\frac{dM_{an}}{dH_e}}{1-\alpha(1-\mathrm{c})\frac{dM_{irr}}{dH_e} - \alpha c\frac{dM_{an}}{dH_e}} \tag{4.5}$$

$$H_e = H + \alpha M \tag{4.6}$$

$$M\left(t+\Delta t\right) = M\left(t\right) + \frac{dM}{dH}\Delta H \tag{4.7}$$

$$B\left(t+\Delta t\right) = \mu_0\left\{H\left(t+\Delta t\right) + M\left(t+\Delta t\right)\right\} \tag{4.8}$$

where k and c are the model parameters, M_{an} the anhysteretic magnetisation, H_e the effective magnetic field strength, M the total magnetisation and δ the directional parameter which is +1 for $dH/dt > 0$ and -1 for $dH/dt < 0$.

According to [4.6] and [4.10], it can be assumed that dM_{irr}/dH_e becomes zero in the magnetisation process if $(M_{an} - M_{irr})dH_e < 0$ as the domain wall displacement does not exist in that case. Therefore, (4.1) can be updated as follows [4.7], [4.10], [4.24]:

$$\frac{dM_{irr}}{dH_e} = \frac{\delta_M \left(M_{an} - M_{irr}\right)}{k\delta} \tag{4.9}$$

where

$$\delta_M = \begin{matrix} 1 & \left(M_{an} - M_{irr}\right)dH_e > 0 \\ 0 & \left(M_{an} - M_{irr}\right)dH_e \leq 0 \end{matrix} \tag{4.10}$$

To improve the accuracy in the calculation of B by J-A model especially at low induction levels, a scaling factor is included in (4.1) which actually reduces the rate of irreversible magnetisation. Thus, according to [4.16], (4.1) can be modified as follows:

$$\frac{dM_{irr}}{dH_e} = \frac{\left(M_{an} - RM_{irr}\right)}{k\delta} \tag{4.11}$$

where R is the scaling factor which can be a constant or a function of B or H. In addition, for further improvement of the model, the pinning parameter, k of the J-A model can also be expressed as a function of B or H depending on the input [4.1], [4.13].

4.2.2 Identification of Model Parameters

In the last few decades, different optimisation techniques, such as genetic algorithm, stimulated annealing and particle swarm optimisation, are becoming popular to identify the J-A model parameters. The optimisation techniques, which are generally used for parameter identification, consider different error criteria that need to be minimum [4.1], [4.7], [4.13], [4.19], [4.21], [4.22]. The root mean square of error, which is mainly error between measured B and calculated B, is commonly used as error criterion that can be expressed as follows [4.1]:

$$\varepsilon_s = \sqrt{\sum_{i}^{N} \frac{\left(B_{meai} - B_{cali}\right)^2}{N}} \tag{4.12}$$

where ε_s is the root mean square of error, N the number of samples per period of the magnetic flux density, B_{meai} the measured magnetic flux density, and B_{cali} the calculated magnetic flux density. The minimum root mean square of error in calculation of B or H of a B-H loop is calculated using optimisation techniques, and the corresponding J-A model parameters are selected for implementation of the model.

4.3 Proposed Model

For design of electromagnetic devices, the proper tracing of H from B or vice versa, and the corresponding iron loss calculation are necessary. The conventional identifications of J-A model parameters are mainly based on the error between experimental and calculated B or H. In the identification process, the relative error between experimental and calculated iron loss is generally ignored. The error in the calculation of the iron loss is obtained from the difference between experimental and calculated iron losses which is as follows:

$$\varepsilon_r = \left| \frac{P_{mea} - P_{cal}}{P_{mea}} \right| \times 100\% \tag{4.13}$$

where ε_r is the relative iron loss error, P_{mea} is the measured iron loss and P_{cal} is the calculated iron loss. In this chapter, the calculated P_{cal} is expressed in W/kg, which is as follows:

$$P = \frac{1}{T\rho} \int_T H \frac{dB}{dt} dt \tag{4.14}$$

where P is the iron loss (W/kg), T time period (s), and ρ the mass density (kg/m^3) of the core. If anyone wants to express the iron loss in W/m^3, the right side of (4.14) needs to be multiplied by the mass density ρ of the magnetic material.

In this study, it is investigated using experimental and calculated data using J-A model that there exist some cases where the minimum root mean square of error (ε_s) between the calculated and measured B, and the minimum relative error in the iron loss calculation do not often occur simultaneously. Therefore, the relative error of iron loss calculation sometimes increases to maintain the minimum ε_s. The existing modified J-A model reported in [4.3] is firstly exploited here where k and R are assumed as function of H. After implementing the J-A model, it is observed from Fig. 4.1(a), that the minimum ε_s at 1.26 T is 0.0347 where the relative error of iron loss calculation, ε_r is 11.701%. On the other hand, the minimum relative error of the iron loss calculation at the same magnetic induction is 0.017% where the ε_s is 0.0625. Similarly, at 0.83 T, both types of errors do not occur simultaneously as shown in Fig. 4.1(b). It is observed from the calculated results that slight increase of ε_s, such as from 0.0347 to 0.0473 at 1.26 T, significantly reduces the iron loss error such as from 11.701% to 4.512%. Therefore, in this study, both ε_s and ε_r are considered as error criteria where both are slightly higher than their minimum values, i.e. a trade-off between ε_s and ε_r is set as error criteria in the optimisation technique. To express ε_s as percentage of its maximum value, (4.12) can be updated as follows:

$$\varepsilon_S = \frac{1}{\max\left(B_{meai}\right)}\sqrt{\sum_{i}^{N}\frac{\left(B_{meai}-B_{cali}\right)^2}{N}}\times 100\%\,. \tag{4.15}$$

Since ε_s slightly increases by the proposed parameter identification method, the errors of the calculation of coercive magnetic field strength (H_c) increases as shown in Fig. 4.2. To mitigate these errors, the rate of irreversible component can be reduced especially at lower magnetic induction levels by introducing a scaling factor in the anhysteretic magnetisation as shown in (4.16) instead of the scaling factor with the irreversible component of magnetisation [4.3] as shown in (4.11). Therefore, according to the proposed anhysteretic magnetisation, the expressions of the anhysteretic magnetisation and its derivative with respective to H_e can be written as:

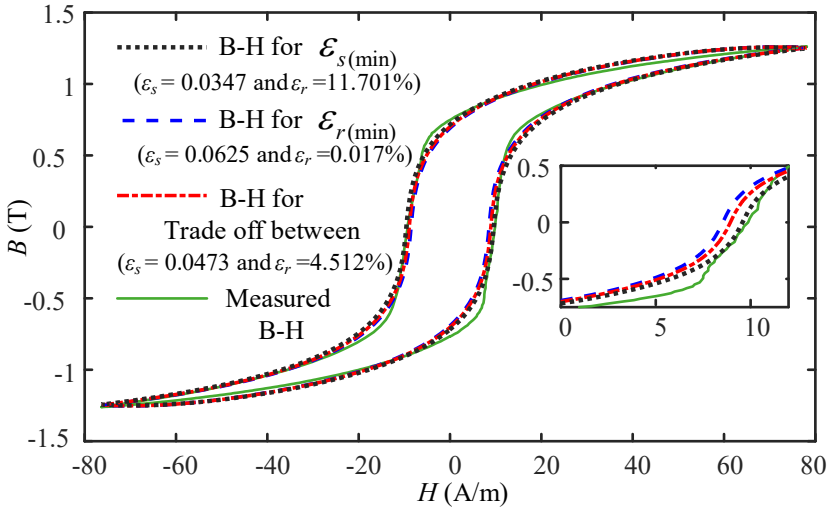

(a)

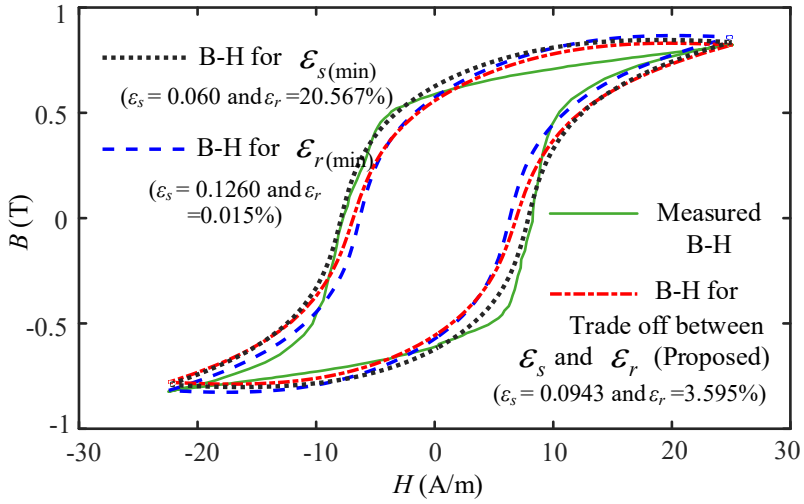

(b)

Fig. 4.1. Comparison of *B-H* loops obtained by experimental measurement and the J-A models for 1 Hz sinusoidal excitations at (a) B_m = 1.26 T and (b) B_m = 0.83 T.

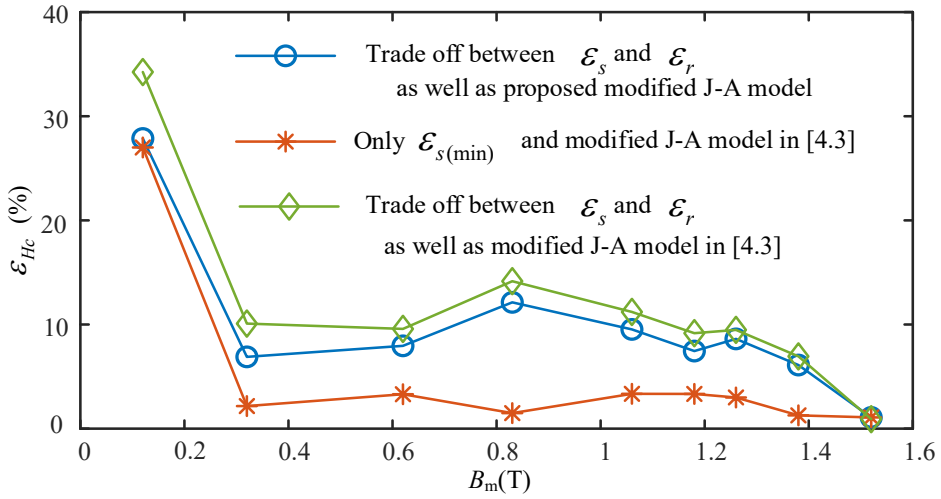

Fig. 4.2. The percentage of error in the calculation of ε_{Hc} with the change of peak magnetic flux densities.

$$M_{an} = \nu M_s \left[\coth \frac{H_e}{a} - \frac{a}{H_e} \right] \tag{4.16}$$

$$\frac{M_{an}}{dH_e} = \frac{\nu M_s}{a} \left[1 - \coth^2 \left(\frac{H_e}{a} \right) + \left(\frac{a}{H_e} \right)^2 \right] \tag{4.17}$$

where ν is the scaling factor which is the function of H or B depending on the input of J-A model. As the scaling factor is only necessary for inner B-H loops, the parameter identification for the large B-H loop is carried out with considering 1 as the value of ν. Since the domain wall displacement does not exist in a specific conditions, e.g. (M_{an} - M_{irr})dH_e < 0, the rate of irreversible magnetisation with respect to the H_e is calculated in this study by (4.9) instead of (4.11).

To identify the J-A model parameters, a large B-H loop with various inner loops are firstly experimentally measured, as the identification process is based on the measured data. The detailed experimental process is discussed in Chapter 3. Since the Brute Force optimisation technique is utilised in this study, the J-A model parameters (k, c, a, α and M_s) are swept away over their specific ranges to produce many sets of model parameters. After that J-A model is implemented using each set of model parameters to calculate B from the given H of the large measured B-H loop. The calculated and measured B-H loops are then exploited to calculate the objective functions which are: (i) $\varepsilon_r < \varepsilon_{rc}$ and ii) $\varepsilon_s < \varepsilon_{sc}$, where ε_{rc} and ε_{sc} are the minimum allowable ε_r and ε_s, and ε_r and ε_s are calculated by (4.13) and (4.15), respectively. If the values of ε_r and ε_s remain within their limits, their values and corresponding model parameters are stored otherwise rejected. When the search is completed, the required solution is selected from the stored data depending on the optimal target. After selecting the J-A model parameters for the large loop, the variables k and ν at other induction levels are calculated with considering other selected four parameters (c, a, α and M_s) as constants. In these cases, k and ν are only swept away over their ranges, and their optimum values are selected in the same way as for the large B-H loop. Fig. 4.3 shows the flow chart of the proposed method for identifying the J-A model parameters. However, instead of a single global optimum value, a set of optimal solutions known as Pareto-optimal solutions, is generally obtained in this study. Pareto-optimal solutions for calculation of k and ν at B_m=1.26 T are shown in Fig. 4.4. From the

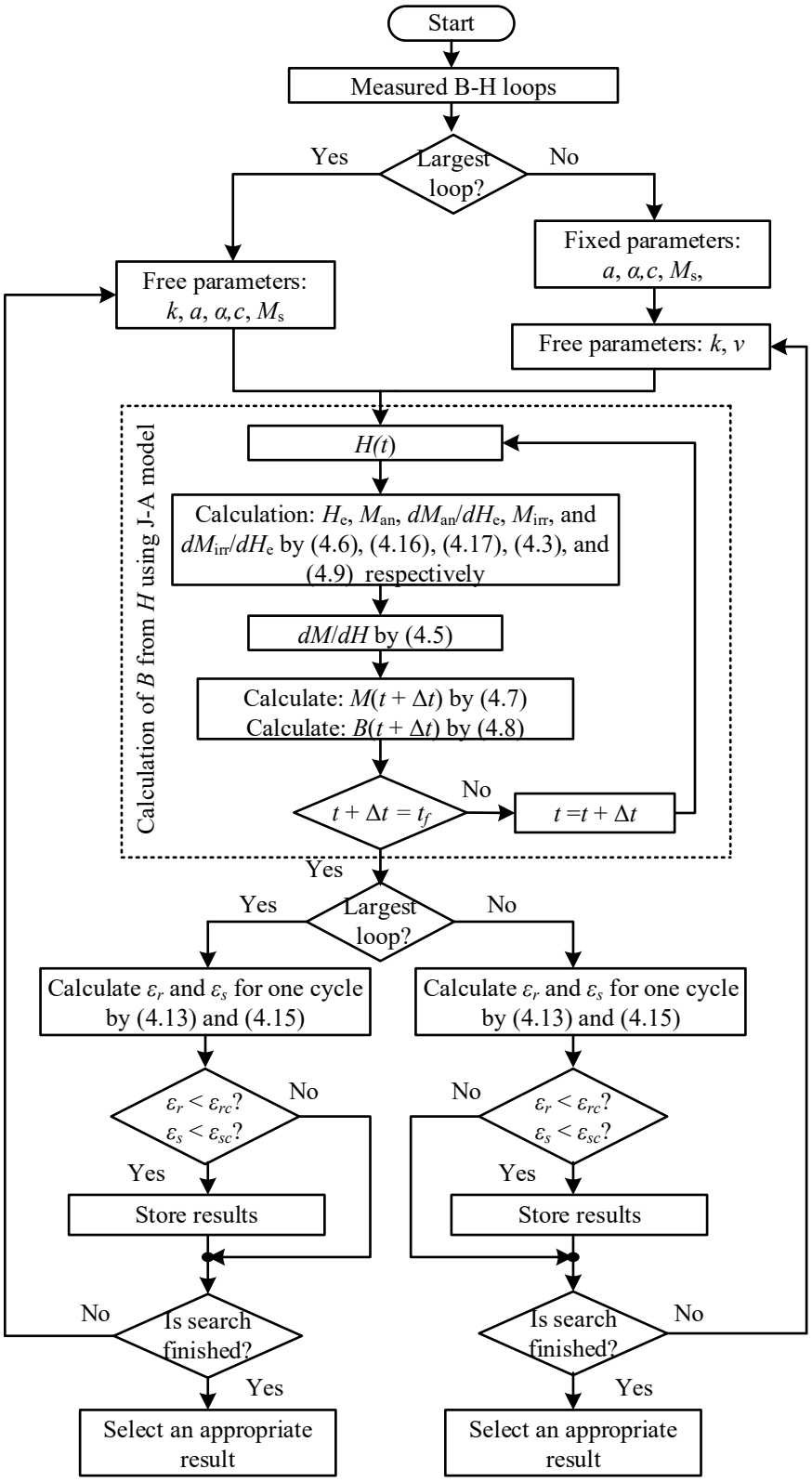

Fig. 4.3. Flow chart of the proposed method for the identifying the J-A model parameters.

figure, it is observed that minimum ε_r and ε_s do not occur at the same point where each point associates with a feasible set of k and ν that satisfy the error criteria. Thus, a point is selected in such a way that both ε_r and ε_s remain in the acceptable values, as shown in Fig. 4.4.

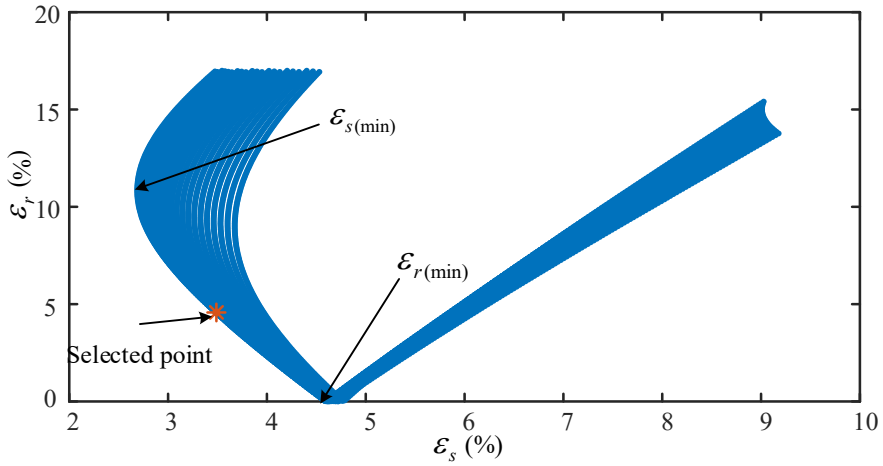

Fig. 4.4. Pareto-optimal solutions by optimisation technique to identify model parameters at 1.26 T.

The constant parameters, c, a, α, and M_s of the J-A model are considered as 0.18, 53.51A/m, 1.10×10^{-4} and 1420000 A/m, respectively. The values of k and v for the considered magnetic core are shown in Figs. 4.5 and 4.6, respectively.

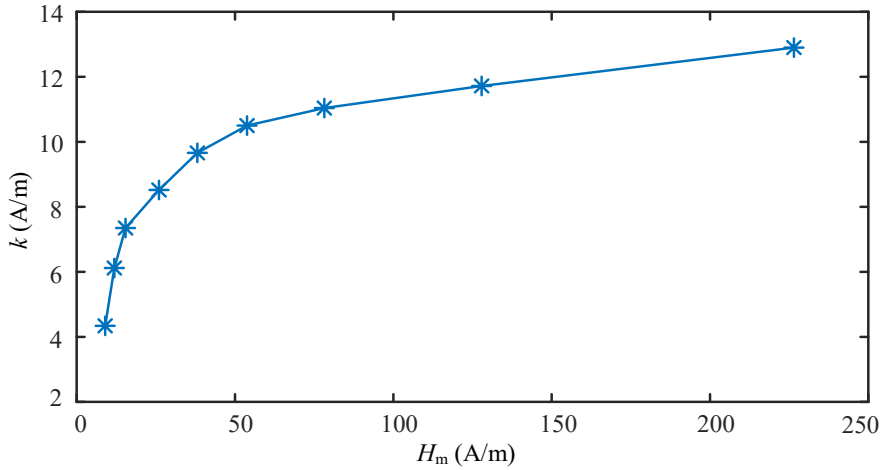

Fig. 4.5. The values of the loss factor k with the change of peak magnetic field strength, H_m.

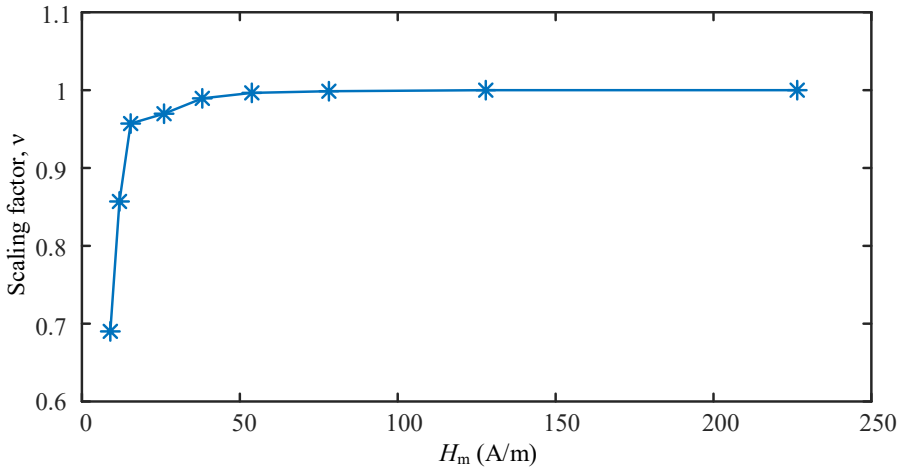

Fig. 4.6. The values of scaling factor v with the change of peak magnetic field strength, H_m.

In the above-proposed algorithm of the J-A model parameter identification, one of the important tasks is the calculation of B from H using the J-A model, as shown in Fig. 4.3. To implement the J-A model, H_e, M_{an}, dM_{an}/dH_e, M_{irr} and dM_{irr}/dH_e are firstly calculated by (4.6), (4.16), (4.17), (4.3), and (4.9), respectively. After that the calculated values of dM_{an}/dH_e and dM_{irr}/dH_e are exploited to calculate the value of dM/dH by (4.5). The value of dM/dH at any time step is used to calculate the magnetisation for the next time step by (4.7). Finally, the corresponding B for a given H is calculated by (4.8). The process is repeated until the calculation of B reaches at final time, t_f.

4.4 Inverse J-A model

For modelling of a magnetic material using finite element method, it generally requires the calculation of H from B which can be achieved by inverse J-A model. In the inverse J-A model, the calculation M at the next step is firstly carried out using its present value, its derivative with respect to B (dM/dB) and the change of B between two consequent steps [4.16]. H is then calculated from M and B. Using the modified J-A model, the change of magnetisation with respective to magnetic flux density can be defined by as follows [4.24]:

$$\frac{dM}{dB} = \frac{(1-c)\delta_M \left(M_{an} - M_{irr}\right) + k\delta c \dfrac{dM_{an}}{dH_e}}{\mu_0 \left[k\delta - (\alpha - 1)(1-c)\delta_M \left(M_{an} - M_{irr}\right) - (\alpha - 1)k\delta c \dfrac{dM_{an}}{dH_e} \right]} \tag{4.18}$$

where M_{an} in this study is calculated by (4.16) instead of conventional M_{an} as shown in (4.4), and dM_{an}/dH_e is calculated by (4.17). Similar to the proposed modified J-A model, k and v are considered as variables in the proposed modified inverse J-A model. The same values of the other constant parameters of the direct J-A model are used in the inverse J-A model. The values of k and v of the inverse J-A model are also calculated in the same way as the direct J-A model. Figs. 4.7 and 4.8 show the obtained values of k and v with the change of peak magnetic flux density, respectively.

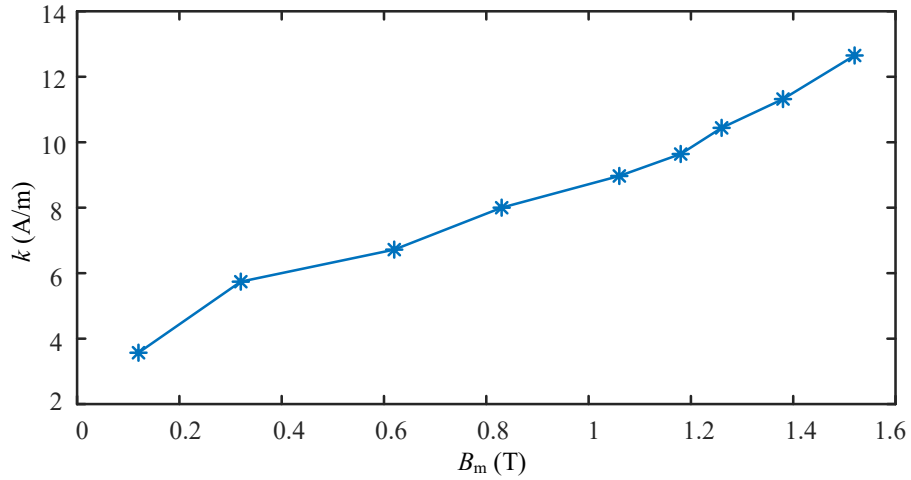

Fig. 4.7. The values of the loss factor k with the change of peak magnetic flux density, B_m.

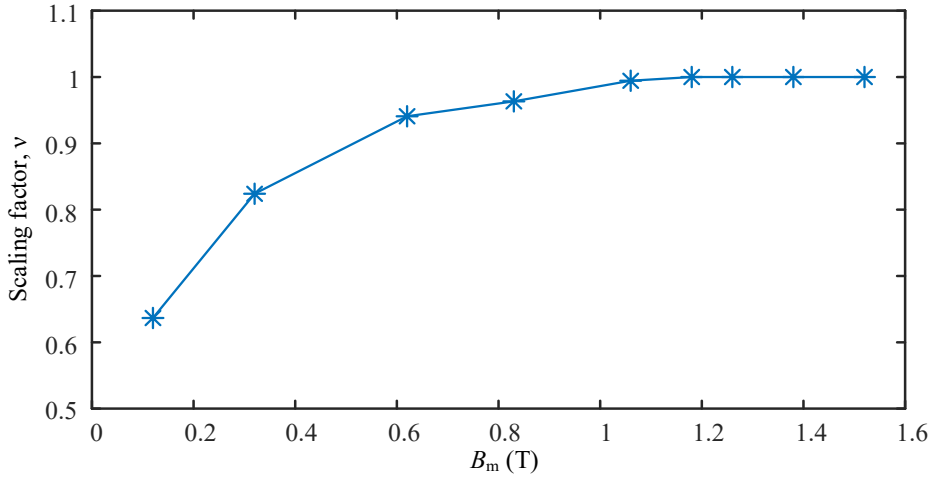

Fig. 4.8. The values of scaling factor v with the change of peak magnetic flux density, B_m.

4.5 Inclusion of Dynamic Losses

Both direct and inverse J-A models with certain model parameters can be used for any specific frequency where all types of magnetic iron losses, e.g. hysteresis loss, eddy

current and excess losses, are inherently retained. The same J-A model parameters cannot be applied if the operating frequency is changed as the *B-H* loop changes with the frequency. To make the generalised J-A model, the loss separation approach is considered where hysteresis, eddy current and excess losses are modelled separately [4.2]. The magnetic field strengths corresponding to the hysteresis and other two losses are calculated using inverse J-A model, classical eddy current and conventional excess loss models, respectively. For hysteresis loss, parameter identification of the inverse J-A model can be carried out based on the *B-H* loops at very low frequency (e.g. no more than 1 Hz) as at that low operating frequency the eddy current and excess losses are negligible. The obtained model parameters can be then used for calculating hysteresis loss and the corresponding magnetic field strength for any frequency. Therefore, the total magnetic field strength can be written as [4.2], [4.25]:

$$H_T = H + \frac{\sigma d^2}{12}\frac{\Delta B}{\Delta t} + \left(\sigma G V_0 A_l\right)^{1/2} \frac{\Delta B}{\Delta t^{0.5}\left|\Delta B\right|^{0.5}} \tag{4.19}$$

where H_T is the total magnetic field strength, d the thickness of the amorphous ribbon, σ the conductivity, Δt the time step between two samples, ΔB the change of magnetic flux density within Δt, A_l the cross-sectional area of the amorphous ribbon, and G and V_0 are constant coefficients. The $(\sigma G V_0 A_l)^{1/2}$ in (4.19) can be calculated by using curve fitting of core loss data which has been already discussed in Chapter 3. The total iron loss is then calculated by (4.14) where the total magnetic field strength is calculated by (4.19).

4.6 Results and Discussions

For experimental verification of the proposed error criteria and proposed modified J-A model, a toroidal amorphous magnetic core is also utilised in this study. The details of experimental procedure can be obtained in Chapter 3.

It has been already discussed in Section 4.3 that the minimum ε_s and minimum ε_r do not often occur simultaneously, and consequently the relative iron loss error ε_r at the minimum ε_s sometimes becomes much higher than its minimum value. Therefore, by using the proposed error criteria where two error criteria are exploited, the value of ε_r reduces significantly, as shown in Fig. 4.9. On the contrary, the proposed error criteria of

the optimisation method for parameter identification slightly increases the values of ε_s, as shown in Fig. 4.10. The proposed modified J-A model, where the scaling factor is introduced in the anhysteretic magnetisation, reduces the percentage of root mean square error ε_s, as shown in Fig. 4.10. In addition, the proposed modified J-A model reduces the error in the calculation of coercive magnetic forces, as shown in Fig. 4.2 (Section 4.3). From Fig. 4.10 it is also observed that the ε_s for the J-A models decreases significantly with the increase of the magnetic induction level. At a low magnetic induction level such as 0.12 T, the ε_s for the proposed modified J-A model is about 19.59 %. On the other hand, at high induction level such as 1.52 T, the ε_s is about 1.92 %.

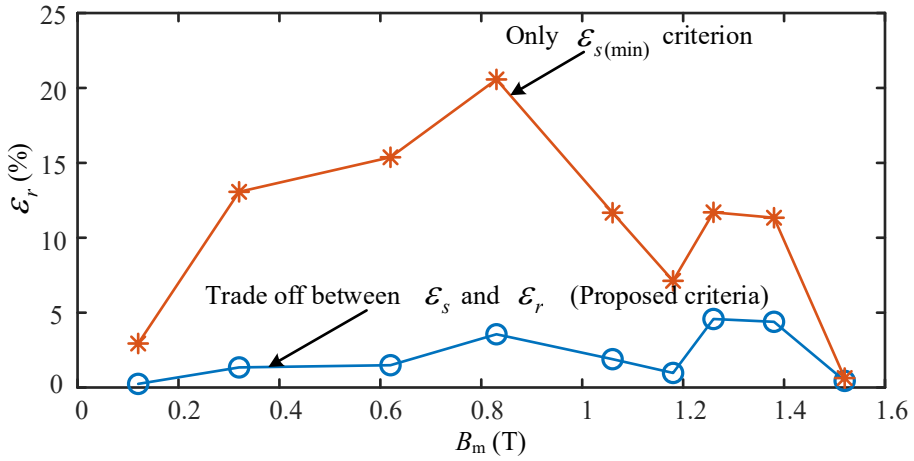

Fig. 4.9. Percentage of core loss error, ε_r with change of peak magnetic flux densities for the proposed error criterion and existing error criterion.

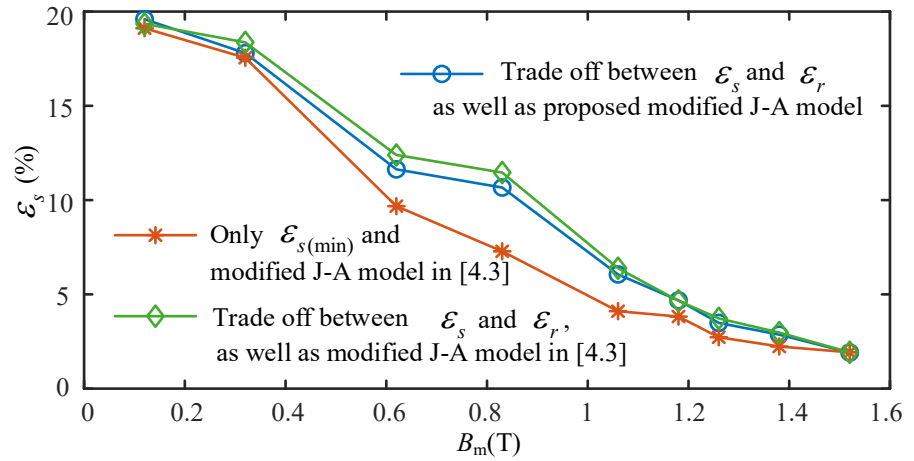

Fig. 4.10. Percentage of root mean square errors of the calculation of B at different peak magnetic flux densities at different conditions of J-A models.

In this study, the inverse J-A model is also based on the proposed error criteria and the proposed modified J-A model. As H is calculated from B by the inverse J-A model, both loss and scaling factors depend on the B_m. From Fig. 4.11, it is observed that the calculated H using the proposed modified inverse J-A model shows a good agreement with the measured H, where the correlation coefficient, r = 0.9987. For consideration of more complex signals than the conventional sinusoidal signal, the minor loops on a major B-H loop are also considered in this study. Two minor loops on a major B-H loop are experimentally obtained by applying an excitation voltage consisting of a 1 Hz fundamental sinusoidal component with a third harmonic component which can be obtained details in Chapter 3. The proposed modified inverse J-A model is then applied to calculate the B-H loop. Fig. 4.12 shows the comparison between the experimental and calculated B-H loops. From Fig. 4.12, it is observed that the calculated minor loops are slightly bigger than the calculated ones and consequently, the error in the calculated core loss (ε_r=8.31%) is slightly high. The reversible magnetisation is mainly responsible for the minor loops. Consequently, the value of reversibility coefficient c needs to be high for the minor loops. Since the constant value of c is considered for both the major and minor loops, the mismatch between calculated and measured core losses increases slightly. In this case, the correlation coefficient between the measured and calculated H is 0.9948.

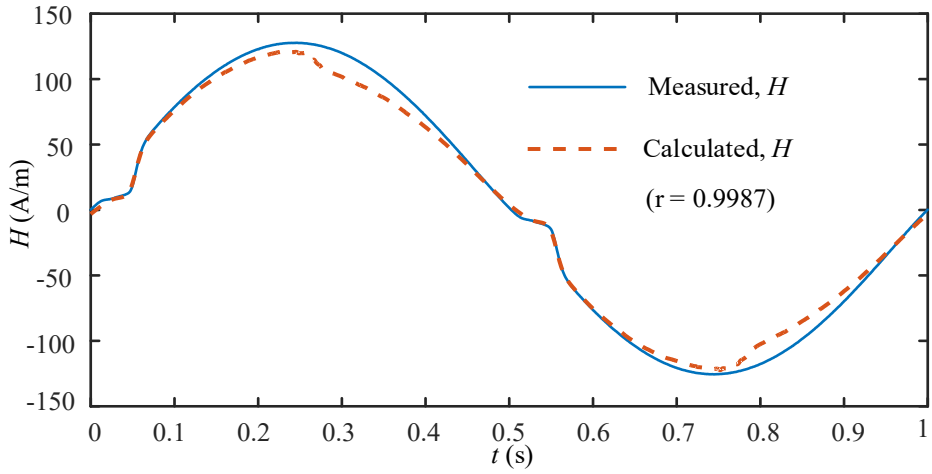

Fig. 4.11. Comparison between calculated and measured H at B_m=1.38 T and 1 Hz excitation.

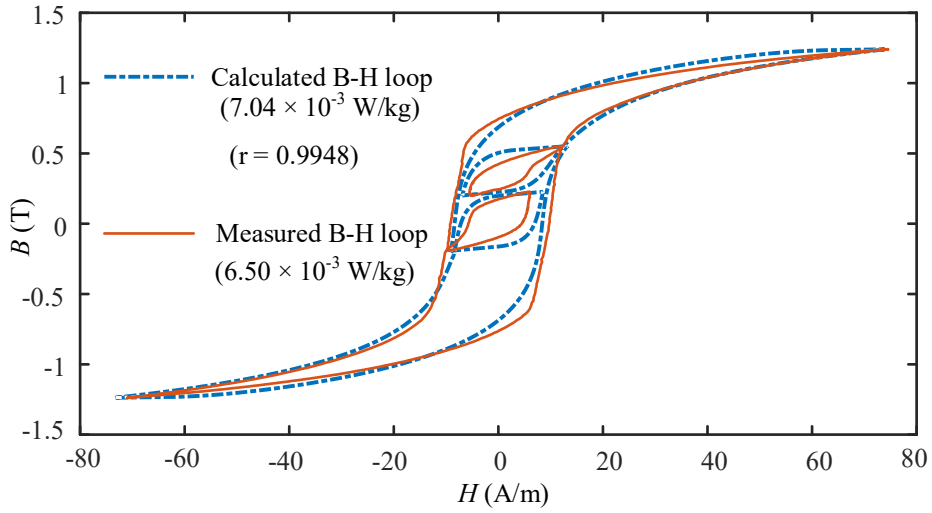

Fig. 4.12. Comparison between the calculated and measured *B-H* loops for two minor loops on a major loop.

To observe the effect of hysteresis, eddy current and excess losses on the total core loss, the core loss is measured at 1.08 T at different frequencies. After that the inverse J-A model along with eddy current and excess models is exploited, and the results are graphically presented in Fig. 4.13. It is observed from Fig. 4.13 that the hysteresis loss per cycle is almost constant with the increase of frequency. On the other hand, both the eddy current and excess losses increase with the frequency although the effect of eddy current is very small compared to the other two losses due to the very thin amorphous ribbon. It can also be seen from Fig. 4.13 that the calculated total core losses are very close to the measured ones.

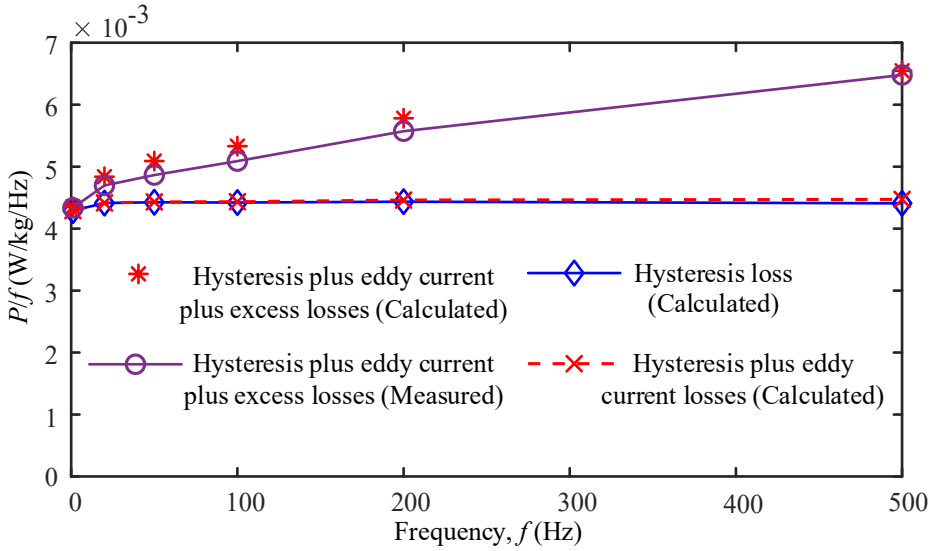

Fig. 4.13. Core loss separation at B_m=1.08 T using the proposed modified inverse J-A model.

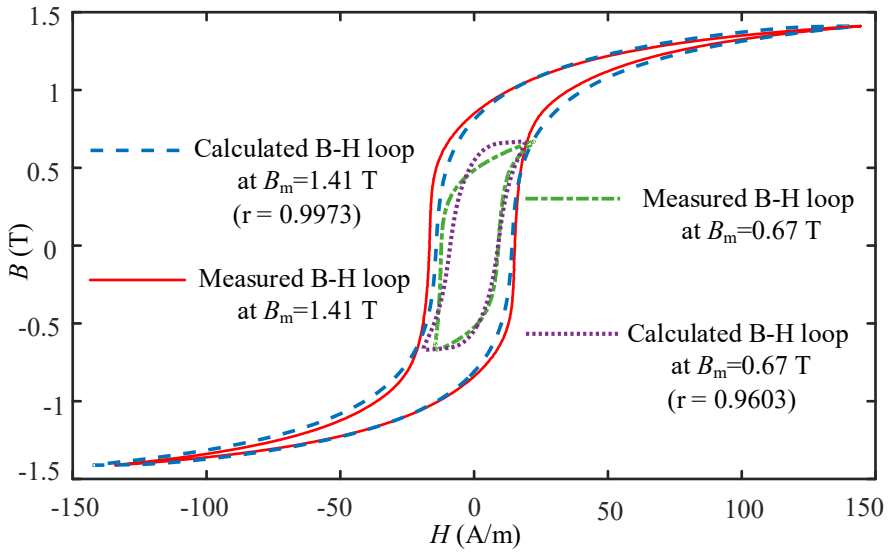

Fig. 4.14. Comparison between the measured and calculated *B-H* loops at 1.41 T and 0.67 T for 500 Hz excitations.

Fig. 4.14 shows the measured and calculated *B-H* loops with the inclusion of a dynamic core loss model in the inverse J-A model. It is observed from Fig. 4.14 that the calculated *B-H* loops under 500 Hz excitations at 1.41 T and 0.67 T are close to their measured ones where the correlation coefficients in the calculation of H are 0.9973 and 0.9603, respectively. The relative error in the iron loss calculation, ε_r for these two cases are 2.86% and 0.16%, whereas ε_s are 3.46% and 16.13%, respectively. From the figure, it is also observed that at high magnetic induction levels especially near to the saturation induction, the calculated *B-H* loop and the corresponding core loss become closer to the experimental ones than those for low magnetic induction levels. In addition, it is observed that area of *B-H* loop and the corresponding iron loss increase with increase of magnetic induction level. It is seen from Fig. 4.15 that the calculated iron loss results show a good agreement with the measured results for a whole range of magnetic induction where the correlation coefficient among their results is 0.9998.

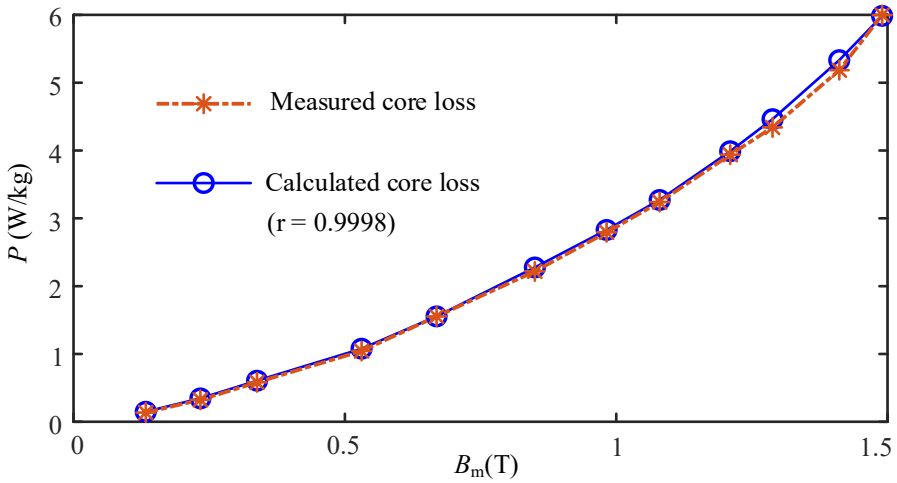

Fig. 4.15. Comparison between the measured and calculated core loss at 500 Hz with different peak magnetic flux densities.

The comparison among empirical, inverse J-A and inverse Preisach models in the calculation of core loss at 1.08 T and at 1.29 T under different frequencies is shown in Fig. 4.16. From Fig. 4.16(a), it is observed that the calculated core loss at 1.08T by inverse J-A model shows better agreement with experimentally measured results than those obtained by the generalised inverse Preisach model. On the other hand, at 1.29 T near to the saturation magnetic flux density, the performance of inverse Preisach model is slightly better than that of inverse J-A model. It is also observed from Fig. 16, for both cases of magnetic flux densities, inverse J-A model and inverse Preisach models provide better results than empirical method.

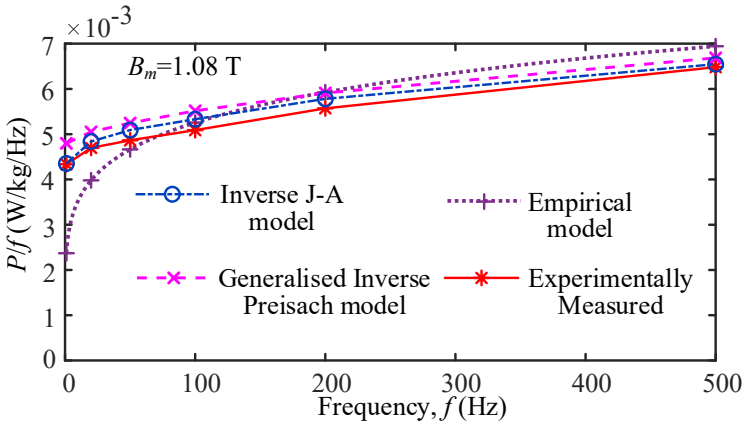

(a)

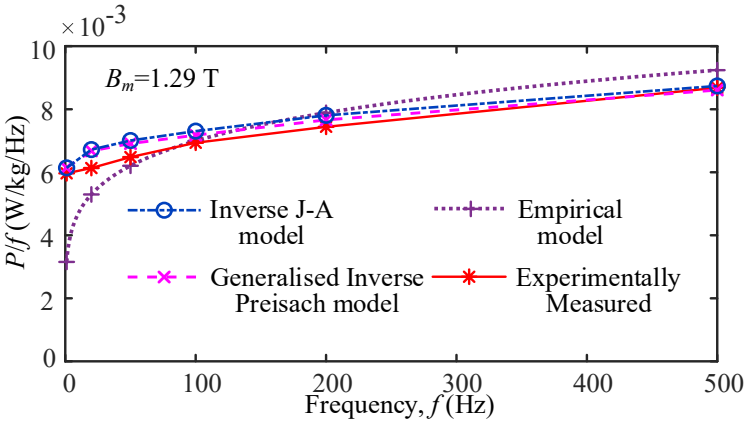

(b)

Fig. 4.16. Comparison among different core loss models at (a) B_m=1.08 T and (b) B_m=1.29 T.

4.7 Conclusion

In this chapter, two error criteria instead of conventional one error criterion are proposed in the optimization method to identify the J-A model parameters, where one is based on the conventional root mean square of error and the other is based on the relative error of iron loss. The proposed error criteria for parameter identification significantly reduce the error of iron loss calculation, e.g., at 1.26 T the iron loss error decreases to 4.512% from 11.701%. A proposed modified J-A model, where a scaling factor is incorporated with anhysteretic magnetisation, reduces the value of the root mean square of error between the measured and calculated waveforms. The proposed modified model also improves the calculation of coercive magnetic force, e.g., the error in the calculation of H_c at 0.62 T reduces from 9.58% to 7.95%. The inverse J-A model based on the proposed modified J-A model also provides good results for both sinusoidal and non-sinusoidal excitations. With the inclusion of the dynamic core loss model with the modified inverse J-A model, there exists a good agreement between calculated and measured iron losses at different frequencies and magnetic induction levels, e.g., the error of iron loss calculation under 500 Hz sinusoidal excitations at 0.67 T and 1.28 T is 0.16% and 2.86%, respectively.

Reference

[4.1] M. Toman, G. Stumberger, and D. Dolinar, "Parameter identification of the Jiles–Atherton hysteresis model using differential evolution," *IEEE Trans. Magn.*, vol. 44, no. 6, pp. 1098–1101, Jun. 2008.

[4.2] N. Sadowski, N. J. Batistela, J. P. A. Bastos, and M. Lajoie-Mazenc, “An inverse Jiles-Atherton model to take into account hysteresis in time-stepping finite-element calculations,” *IEEE Trans. Magn.*, vol. 38, no. 2, pp. 797–800, Mar. 2002.

[4.3] S. Hussain and D. A. Lowther, “The Modified Jiles–Atherton Model for the accurate prediction of iron losses,” *IEEE Trans. Magn.*, vol. 53, no. 6, Jun. 2017, Art no. 7300504.

[4.4] D. C. Jiles and D. L. Atherton, “Theory of ferromagnetic hysteresis,” *J. Magn. Magn. Mat.*, vol. 61, no. 1–2, pp. 48–60, Sep. 1986.

[4.5] D. C. Jiles and J. B. Thoelke, “Theory of ferromagnetic hysteresis: determination of model parameters from experimental hysteresis loops,” *IEEE Trans. Magn.*, vol. 25, no. 5, pp. 3928–3930, Sep. 1989.

[4.6] D. C. Jiles, J. B. Thoelke, and M. K. Devine, “Numerical determination of hysteresis parameters for the modeling of magnetic properties using the theory of ferromagnetic hysteresis,” *IEEE Trans. Magn.*, vol. 28, no. 1, pp. 27–35, Jan. 1992.

[4.7] P. Kis and A. Iványi, “Parameter identification of Jiles–Atherton model with nonlinear least-square method,” *Phy. B: Cond. Mat*., vol. 343, nos. 1–4, pp. 59-64, Jan. 2004.

[4.8] S. Rosenbaum, M. Ruderman, T. Strohla, and T. Bertram, “Use of Jiles–Atherton and Preisach Hysteresis Models for Inverse Feed-Forward Control,” *IEEE Trans. Magn.*, vol. 46, no. 12, pp. 3984–3989, Dec. 2010.

[4.9] Z. Birčáková, P. Kollár, J. Füzer, R. Bureš, and M. Fáberová, “Magnetic properties of selected Fe-based soft magnetic composites interpreted in terms of Jiles-Atherton model parameters,” *J. Magn. Magn. Mater*., volume 502, May 2020, Art. no. 166514.

[4.10] A. J. Bergqvist, “A simple vector generalization of the Jiles-Atherton model of hysteresis,” *IEEE Trans. Magn.*, vol. 32, no. 5, pp. 4213–4215, Sep. 1996.

[4.11] Henan ZY Amorphous Technology Co. Ltd. [Online]. Available: https://www.zyamorphous.com/. (Accessed 25 July 2020).

[4.12] Guangzhou Amorphous Electronic Technology Co. Ltd., Guangzhou, China. [Online]. Available: https://coilcore.en.alibaba.com/. (Accessed 22 December 2020).

[4.13] P. R. Wilson, J. N. Ross, and A. D. Brown, “Optimizing the Jiles-Atherton model of hysteresis by a genetic algorithm,” *IEEE Trans. Magn.*, vol. 37, no. 2, pp. 989–993, Mar. 2001.

[4.14] K. H. Carpenter, “A differential equation approach to minor loops in the Jiles-Atherton hysteresis model,” *IEEE Trans. Magn.*, vol. 27, no. 6, pp. 4404–4406, Nov. 1991.

[4.15] D. Lederer, H. Igarashi, A. Kost, and T. Honma, “On the parameter identification and application of the Jiles-Atherton hysteresis model for numerical modelling of measured characteristics,” *IEEE Trans. Magn.*, vol. 35, no. 3, pp. 1211–1214, May 1999.

[4.16] J. V. Leite, A. Benabou, and N. Sadowski, “Accurate minor loops calculation wit a modified Jiles-Atherton hysteresis model,” *COMPEL-Int. J. Comput. Math. Elect. Electron. Eng*., vol. 28, no. 3, pp. 741–749, 2009.

[4.17] J. P. A. Bastosa and N. Sadowski, Electromagnetic modeling by finite element methods, Boca Raton, FL: CRC Press, 2003, pp. 438–455.

[4.18] I. Podbereznaya and A. Pavlenko, “Accounting for dynamic losses in the Jiles-Atherton model of magnetic hysteresis,” *J. Magn. Magn. Mater*., volume 513, Nov. 2020, Art. 167070.

[4.19] Y. Li, J. Zhu, Yongjian Li, H. Wang, and L. Zhu, “Modeling dynamic magnetostriction of amorphous core materials based on Jiles–Atherton theory for finite element simulations,” *J. Magn. Magn. Mater*., vol.529, Jul. 2021, Art. 167854.

[4.20] F. R. Fulginei and A. Salvini, “Softcomputing for the identification of the Jiles-Atherton model parameters,” *IEEE Trans. Magn.*, vol. 41, no. 3, pp. 1100–1108, Mar. 2005.

[4.21] D. Zhang, M. Jia, Y. Liu, Z. Ren, and C. Koh, “Comprehensive improvement of temperature-dependent Jiles–Atherton model utilizing variable model parameters,” *IEEE Trans. Magn.*, vol. 54, no. 3, Mar. 2018, Art no. 7300504.

[4.22] J. V. Leite, N. Sadowski, P. Kuo-Peng, N. J. Batistela, and J. P. A. Bastos, “The inverse Jiles-Atherton model parameters identification,” *IEEE Trans.Magn.*, vol. 39, no. 3, pp. 1397–1400, May 2003.

[4.23] M. Mahoor, F. R. Salmasi, and T. A. Najafabadi, “A hierarchical smart street lighting system with Brute-Force energy optimization,” *IEEE Sens. J.* 17 (9) (2017) 2871–2879.

[4.24] W. Li, I. H. Kim, S. M. Jang, and C. S. Koh, “Hysteresis modeling for electrical steel sheets using improved vector Jiles-Atherton hysteresis model,” *IEEE Trans. Magn.*, vol. 47, no. 10, pp. 3821–3824, Oct. 2011.

[4.25] E. Fallah and J. S. Moghani, “A new approach for finite-element modeling of hysteresis and dynamic effects,” *IEEE Trans. Magn.,* vol. 42, no. 11, pp. 3674–3681, Nov. 2006.

Chapter 5 Measurement and Modelling of Core Loss Under Rotating Magnetic Field

5.1 Introduction

In the previous Chapters 3 and 4, the magnetic field is considered as alternating in which amplitudes of both magnetic flux density and magnetic field strength vary with time. On the other hand, there exist some cases, e.g., the rotating electrical machines and the T-joints of the three-phase transformers, where rotating magnetic field is mainly concerned [5.1], [5.2]. The rotating magnetic field actually varies with both time and orientation, and consequently the power loss in the magnetic core due to the rotating magnetic field is different from that caused by the alternating magnetic field. In addition, since the permeability property of magnetic material generally varies in different directions, the corresponding power dissipations may also vary, and this variation needs to be considered in the design of the electrical machines.

In the literature, different types of electrical machines were proposed where amorphous magnetic materials are used as core material [5.3]–[5.5] due to their low core loss property. In this study, the selected Fe-based amorphous magnetic material (amorphous 1k101 metal) [5.6], [5.7], is used for the investigation of the 2-D rotational core loss.

The alternating core loss measurement methods cannot be used to characterise the magnetic core under the rotating magnetic field. For estimation of the core loss in the presence of the rotating magnetic field, two-dimensional (2-D) measurement techniques are generally utilised. In 1896, the first measurement technique of the rotational core loss was developed by Baily [5.8], where the developed torque, which is imposed on the core specimen by rotational magnetic field, is firstly measured and the corresponding loss is then calculated from the measured torque. In the last hundred years, different rotational core loss measurement methods such as thermometric method, field-metric method and watt-metric method were developed [5.8]–[5.13]. In this chapter, the field metric method is used to measure the core loss, as the magnetic field in the specimen in the method can be easily controlled by a feedback system. Based on the different measurement techniques, different testing devices such as the square specimen tester (SST), disk

specimen tester and large sheet-based tester were developed [5.2], [5.8]–[5.10], [5.15]–[5.17].

In the literature, different researchers of refs. [5.18]–[5.20] investigated the 2-D core loss measurements and modellings of soft magnetic composite materials and silicon steels. The experimental investigation of 2-D vector magnetic properties of Metglas 2605 HB1 and Metglas 2650S-2 amorphous materials was experimentally investigated in [5.21] and [5.22], respectively. In those cases, the mathematical modellings are not carried out. For modelling of rotational hysteresis loss, two empirical methods are commonly utilised: one is founded on the analogical approach [5.23] and the other on alternating measured hysteresis loss data [5.24]. The analogical model of rotational hysteresis loss shows better accuracy than the model obtained from the alternating loss data. In addition, the analogical rotational hysteresis model is independent of the alternating measured hysteresis loss. The first method basically uses the torque equation of a single-phase induction motor to model the rotational hysteresis loss, as its torque-slip relation is similar to the relation between rotational hysteresis loss and magnetic flux density. In the same way, it is observed that the equation of developed mechanical power of a three-phase induction motor, which also shows similar patterns to the rotational hysteresis loss, is more simplified approach than the torque equation of the single-phase induction motor. Therefore, it is a big opportunity to use the developed mechanical power equation of a three-phase induction motor to model the rotational hysteresis loss for not only simplifying the approach but also improving the accuracy. Since the eddy current and excess losses occur simultaneously with hysteresis loss for any time changing excitation, their modellings are also included with hysteresis loss models to obtain the total loss under both circular and elliptical rotating magnetic fields. The modelling of 2-D magnetic rotational core loss of any amorphous metal has not been found in the literature.

In this chapter, the 2-D vector magnetic properties of a Fe-based amorphous magnetic material named amorphous 1k101 metal has been investigated under 2-D rotating magnetic fields. In addition, the rotational core loss separation (divided into hysteresis, eddy and excess losses) is also carried out in this chapter. Furthermore, an improved and simplified rotational hysteresis loss model is proposed in this study. Finally, the modelling of the total core loss is carried out to calculate the rotational loss. The proposed

model is verified by considerable agreement between experimental and simulation results.

5.2 2-D Core Loss Testing System

5.2.1 2-D Core Loss Tester

The square specimen tester (SST) initiated by Brix [5.14] is favourable for measuring 2-D core loss due to its flexible control system, uniform magnetic field and high accuracy. In 1993, an SST, which is utilised in this study, was developed at University of Technology Sydney (UTS), Australia [5.2], [5.25] to experimentally measure the 2-D vector magnetic properties of soft magnetic materials. The corresponding block diagram of the 2-D experimental set-up is shown in Fig. 5.1. The SST consists of yokes made of vertically laminated grain-oriented silicon steel sheets. The shapes of the yokes were constructed in such a way that the tester has four wedge type magnetic poles**.** Two sets of excitation coils are arranged on X and Y-axes magnetic poles, and each set has two coils, which are connected in series. Each coil consists of 300 turns of 1.6 mm insulated copper wire. In the middle of the tester, a square specimen of the material is placed as shown in Fig. 5.1. The rotating magnetic field is then generated around the specimen by exciting both groups of exciting coils. Labview is used for data acquisition, and generating the two channel excitation signals of 90^{o} phase difference to produce rotational magnetic fields. The rotating magnetic field generated by the tester induces magnetisation in the specimen, and the induced magnetisations are then measured by **B** and **H**-sensing coils for both axes, respectively.

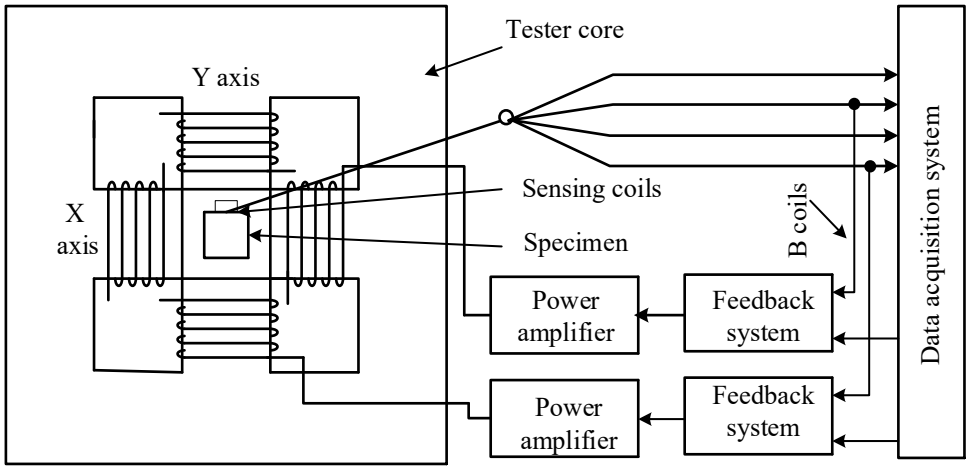

Fig. 5.1. Block diagram of 2-D square specimen testing system [5.25].

A feedback system is employed to control the shape of the induced voltage in the **B**-sensing coils. A two-channel power amplifier is used in the testing system to amplify the voltage as well as power of the output signals of the feedback system so that they can be capable to excite the coils of the tester. A photo of the 2-D rotational core loss measurement system is shown in Fig. 5.2. The specimen was cut from the AMCC-320 amorphous core [5.7] which is made of amorphous 1k101 strips, and the dimensions of the specimen are 50 mm × 50 mm × 0.86 mm. As the thickness of an amorphous strip of the core is about 25 μm which indicates that the specimen, whose thickness is 0.86 mm, consists of a stack of amorphous strips. The stacking factor of the specimen is the same as that of the core which is about 85%.

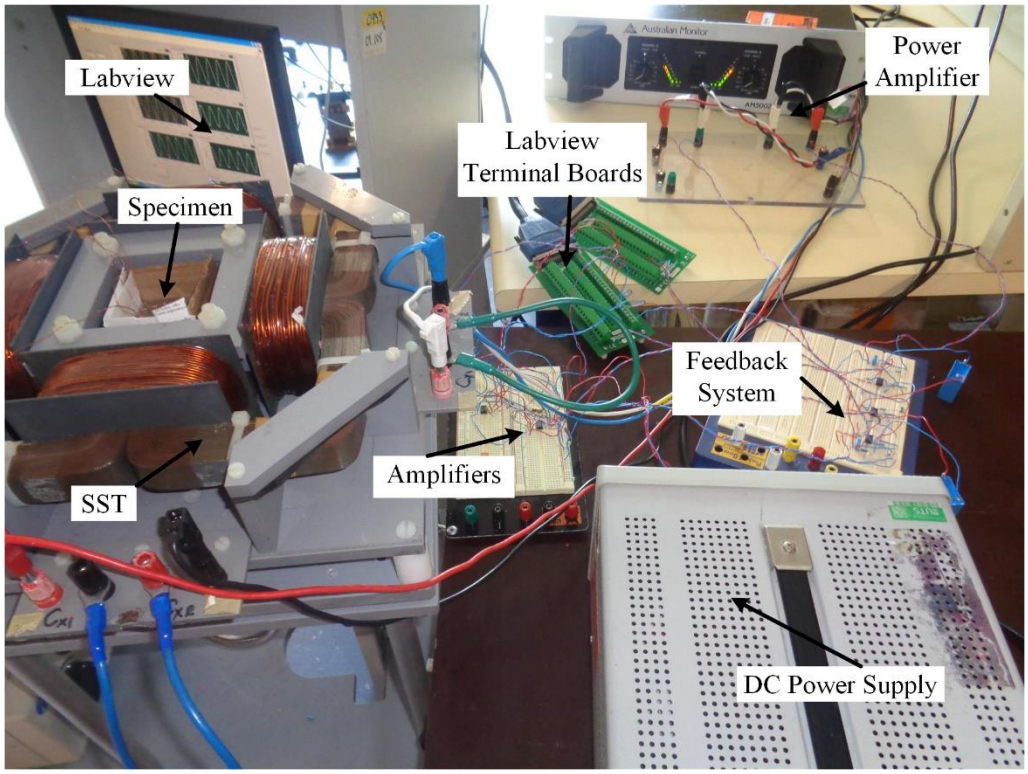

Fig. 5.2. A photo of the 2-D core loss measurement set-up.

5.2.2 Measurement Methods for B and H

Since the core loss is measured using field-metric method, the measurements of magnetic flux density and magnetic field strength are firstly required to be measured. **B** and **H** are measured from the sensing coils which are placed around specimen. The voltages induced in **H**-sensing coils are very small especially at low frequency and low magnetic flux

density. Therefore, the measured induced voltages sometimes are not smooth, and they can be easily affected by electrical interferences during measurement process. Precision operational amplifiers with high amplification factor e.g., about 100, are utilised to overcome the low voltage measurement problems. On the other hand, the low voltage problems for **B**-sensing coils are not so severe as that of **H**-sensing coils since the voltages induced in **B-**sensing coils are much higher than that of-**H** sensing coils. Nevertheless, amplifiers with low amplification factor, e.g., about 2, are also used for **B**-sensing coils to co-relate with **H**-sensing coils.

The **B**-sensing coils are wound over the middle of the specimen so that one coil is positioned in the X-axis direction and the other in the Y-axis direction. Each coil consists of 15 turns of 0.1 mm enamel insulated copper wire. The components of **B** on each axis are then calculated by the following equation, respectively.

$$B_i = \frac{1}{\mathrm{K_{Bi}}} \int v_{\mathrm{B}i} dt \qquad i = x, y \tag{5.1}$$

where $\mathrm{K_{Bi}}=\mathrm{K_s N_{Bi} F_{Bi} d_{th} d_{lw}}$ are the coefficient of B_i-sensing coils, $\mathrm{N_{Bi}}$ the number of turns of the sensing coils, $\mathrm{F_{Bi}}$ the amplification factors, $\mathrm{K_s}$ the stacking factor, $\mathrm{d_{th}}$ the thickness of the specimen, $\mathrm{d_{lw}}$ the length or width of the specimen, and $v_{\mathrm{B}i}$ the induced voltages on sensing coils.

The **H**-sensing coil of each axis consists of 153 turns of enamel insulated copper wire of 0.06 mm in diameter wound over a 0.50 mm plastic former. The components of magnetic field strength are then calculated by the following equation [5.2]:

$$H_i = \frac{1}{\mu_0 \mathrm{K_{Hi}}} \int v_{Hi} dt \qquad i = x, y \tag{5.2}$$

where μ_0 is the permeability of air, v_{Hi} is the induced voltage on the sensing coil and $\mathrm{K_{Hi}}$ is the **H**-sensing coil coefficient obtained by calibration [5.2]. For the determination of $\mathrm{K_{Hi}}$, the sensing coils are placed in the middle of a solenoid, and the voltages induced across the sensing coils and the corresponding magnetic flux density are then measured.

The orientation of each sensing coil is adjusted in such a way so that the maximum voltage is induced in each coil. The magnetic flux density is measured by a Gauss meter. There is another method for calculating the magnetic flux density in the solenoid which is calculated from the measured excitation current and solenoid's B/I ratio [5.2]. The value of K_{Hi} is then calculated by the following equation

$$K_{Hi} = \frac{V_{Hi}}{2\pi\mu_0 f H_m} \qquad i = x, y \tag{5.3}$$

where H_m is the maximum field strength, f is the excitation frequency and V_{Hi} is the peak voltage induced in the sensor. A photo for the calibration of the **H**-sensing coils is shown in Fig. 5.3. The solenoid coil is excited with different excitation currents and K_{Hi} is calculated using (5.3) for each excitation. The average value of them is then taken as the value of K_{Hi}. Tables 5.1 and 5.2 list the calibration results of the H_x and H_y-sensing coils for different excitation currents.

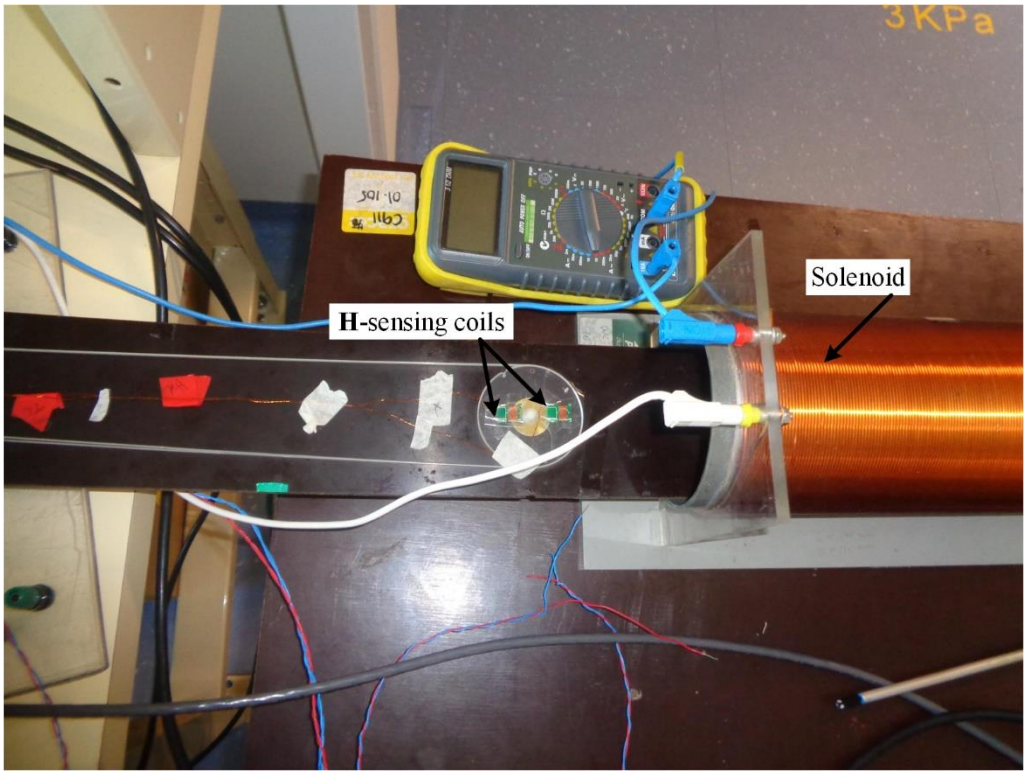

Fig. 5.3. Calibration of **H** sensing coils using a solenoid.

Table 5.1

Calibration of H_x-sensing coil

Si	I (A) (rms)	B_I (mT) (peak)	B_{GM} (mT) (peak)	H_m (A/m)	V_{Hx} (V)	K_{Hx} (m^2)
1	0.5	1.032376	1.05	835.5614973	0.0286405	0.086824124
2	1	2.064752	2.09	1663.165266	0.0577475	0.087950034
3	2	4.129504	4.17	3318.372804	0.1150475	0.087819355
4	3	6.194255	6.27	4989.495798	0.1727080	0.087678685
5	4	8.259007	8.35	6644.703336	0.2287165	0.087188686
6	5	10.32376	10.46	8323.784059	0.2869680	0.087327474
					Average	0.087464726

Table 5.2

Calibration of H_y-sensing coil

Si	I (A) (rms)	B_I (mT) (peak)	B_{GM} (mT) (peak)	H_m (A/m)	V_{Hy} (V)	K_{Hy} (m^2)
1	0.5	1.032376	1.05	835.5614973	0.0280250	0.084958226
2	1	2.064752	2.09	1671.122995	0.0560780	0.085000667
3	2	4.129504	4.17	3318.372804	0.1117965	0.085337765
4	3	6.194255	6.27	4989.495798	0.1679070	0.085241361
5	4	8.259007	8.35	6644.703336	0.2237875	0.085309709
6	5	10.32376	10.46	8323.784059	0.2792230	0.084970587
					Average	0.085136386

5.2.3 Misalignment of H Sensing Coils

Due to the misalignment of the **H**-sensing coils with the specified axes, the calculation of power loss becomes different from its original values. The effect of misalignment of the **H**-sensing coils on the power loss calculation can be eliminated by averaging the power losses at both clockwise and anticlockwise rotating magnetic field directions. On the other hand, the effect of misalignment of the **H**-sensing coils on the magnetic field strength can be corrected by rotating the coordinate axes as shown in Fig. 5.4, which can be done by the following equation [5.2]:

$$\begin{bmatrix} C_x \\ C_y \end{bmatrix} = \frac{1}{\cos\alpha_x \cos\alpha_y + \sin\alpha_x \sin\alpha_y} \begin{bmatrix} \cos\alpha_y & -\sin\alpha_x \\ \sin\alpha_y & \cos\alpha_x \end{bmatrix} \begin{bmatrix} C'_x \\ C'_y \end{bmatrix} \tag{5.4}$$

where α_x and α_y are the misalignment angles with the X and Y-axes respectively, C_x and C_y are the corrected values, and C'_x and C'_y are the corresponding measured values. Misalignment angles are then calculated as follows [5.2]:

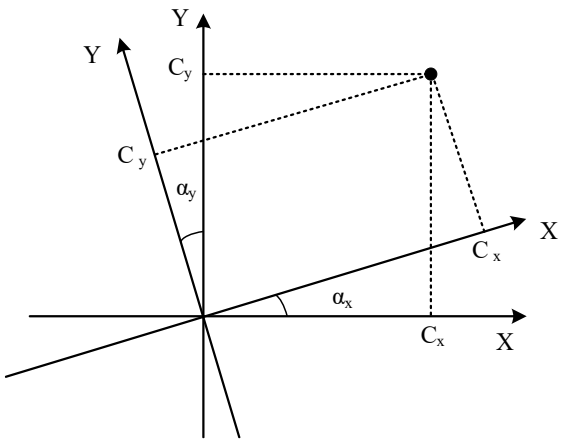

Fig. 5.4. Rotation of the co-ordinate axis to deal the misalignment problems [5.2].

$$\alpha_x = \cos^{-1}\left(\pm A_x \sqrt{\frac{1-A_y^2}{A_x^2-A_y^2}}\right) \tag{5.5}$$

$$\alpha_y = \cos^{-1}\left(\frac{\sin\alpha_x}{A_y}\right) \tag{5.6}$$

where $A_x = C'_x / C'_y$ when only the X-axis coils are excited, and $A_y = C'_x / C'_y$ when only the Y-axis coils are excited.

There is another approach for calculating the misalignment angles α_x and α_y, which is based on the trial and error method [5.26]. The α_x and α_y are considered such values that the calculated power loss is equal to the average value of power losses obtained from both clockwise and anticlockwise rotations.

5.2.4 Feedback System

The magnetisation on ferromagnetic materials shows a non-linear relationship with the magnetic field strength especially at the vicinity of the saturation point. Consequently,

the magnetic flux density becomes non-sinusoidal in spite of sinusoidal excitation voltage. Therefore, the rotating magnetic field **B** no longer exists as circular. To obtain a circular rotating magnetic field, a feedback differential control circuit on each axis is added in the testing system [5.2]. A differential amplifier is mainly exploited as the feedback system on each axis of the tester which receives the differential input obtained from Labview and amplified **B**-sensing coil signals as shown in Fig. 5.5. A high pass filter with very low cut off frequency (0.3 Hz) is also used in each axis to decrease the drift voltage which appears from the amplifier. Moreover, a low pass filter is used in each axis circuit to eliminate the high frequency interferences which may exist from inter-windings interference or other electrical equipment near the testing set up. Fig. 5.5 shows the feedback circuit for each axis of the tester. Precision amplifier LTC1151 is used as the operational amplifier of the feedback circuit which shows the maximum offset voltage 5 μV, and low noise 1.5 $\mu V_{p\text{-}p}$ [5.27].

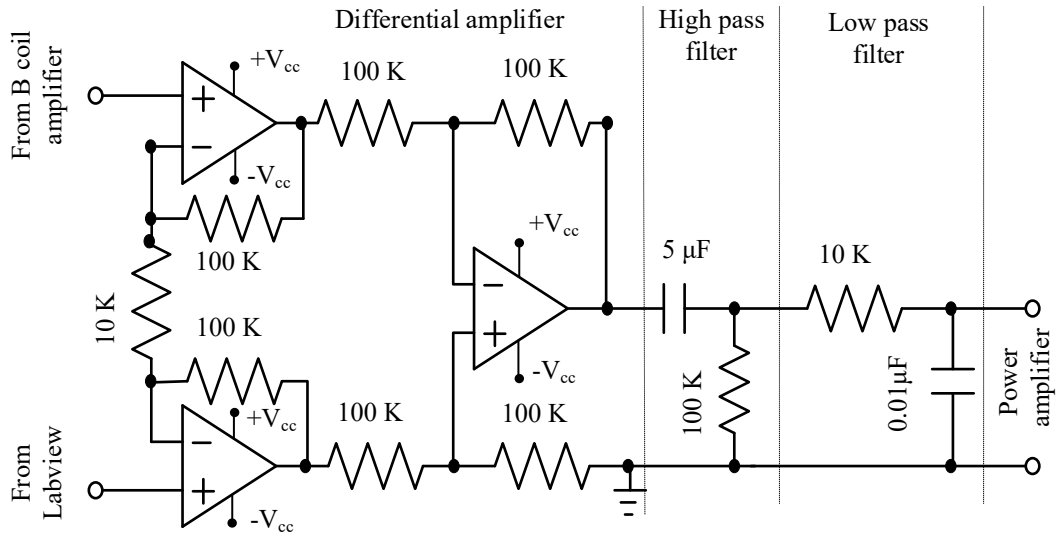

Fig. 5.5. Feedback system used for the 2-D magnetic properties measurement system [5.2].

5.3 Core Loss Measurements under Different Rotating Magnetic Fields

5.3.1 Core Loss Measurement under Circularly Rotating Magnetic Field

If a rotating magnetic field is imposed on a magnetic specimen, power dissipation

happens which can be theoretically derived from Poynting's theorem [5.2]. Accordingly, the loss dissipated in the specimen is obtained by the following equation,

$$P_t = \frac{1}{T\rho}\int_0^T \left(H_x \frac{dB_x}{dt} + H_y \frac{dB_y}{dt} \right) dt \tag{5.7}$$

where P_t is the total core loss (W/kg), T the time period (s), ρ the mass density (kg/m^3), H_x and H_y the components of **H**, and B_x and B_y the components of **B,** respectively. Fig. 5.6 shows the rotational core losses of the magnetic material at different frequencies and different maximum magnetic flux densities (B_m). It is noticed from Fig. 5.6 that the loss increases with the increase of the **B** except when it is near to the magnetic saturation region especially at low frequencies, e.g., 5 Hz, 10 Hz and 20 Hz. In those cases, the core loss decreases slowly due to the annihilation and formation of the magnetic domain walls.

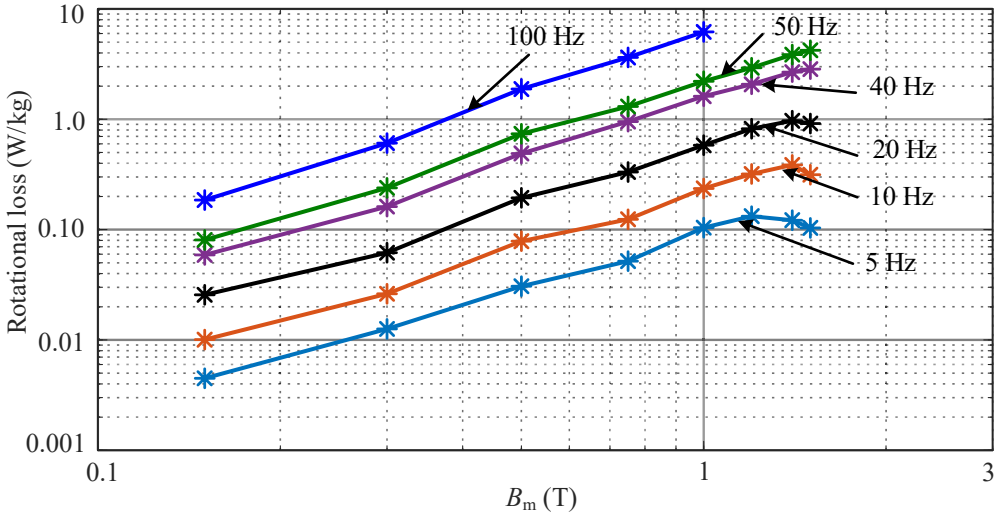

Fig. 5.6. Rotational core losses of the amorphous magnetic material with B_m for different frequencies.

Figs. 5.7 and 5.8 show the controlled circular loci of **B** and the corresponding loci of **H** at different magnetic flux densities under 50 Hz rotating magnetic fields, respectively. It is noticed from Fig. 5.8 that the loci of **H** are not circular as the permeability of the amorphous material varies with **B**. In addition, the maximum values of H_x and H_y are not exactly the same, which indicates that the permeability of the magnetic material in the X and Y-directions differs slightly.

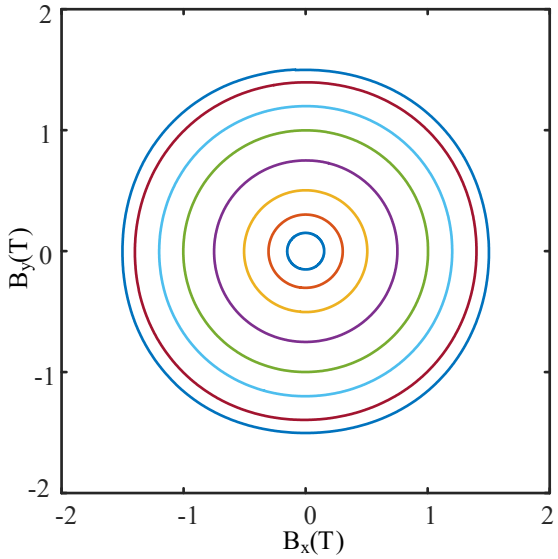

Fig. 5.7. Loci of **B** at different magnetic flux densities under 50 Hz rotating magnetic field.

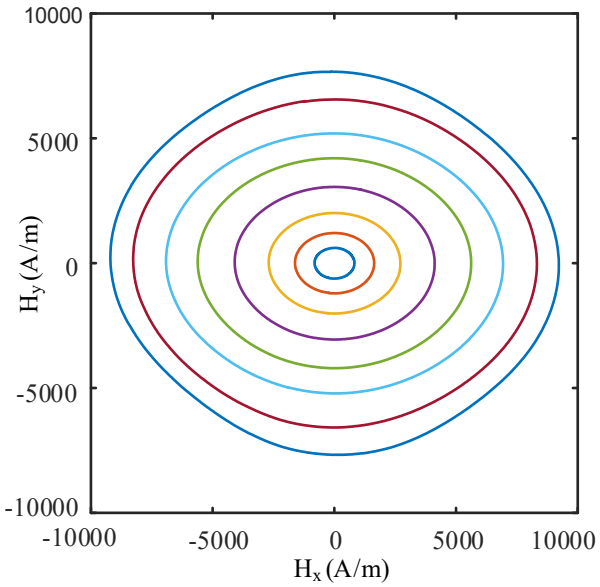

Fig. 5.8. Loci of **H** at different magnetic flux densities under 50 Hz rotating magnetic field.

5.3.2 Core Loss under Alternating Magnetic Field

The above mentioned 2-D core loss testing system can also be utilised to measure the alternating loss of the magnetic material. In this case, the excitation coils on X and Y-axes of the tester are excited separately, and their corresponding core losses are measured. The alternating losses on the X-axis (Transverse direction) and Y-axis (Rolling direction) differ slightly from each other due to the anisotropy of the magnetic material. The average value of them can be used as the final alternating core loss of the material.

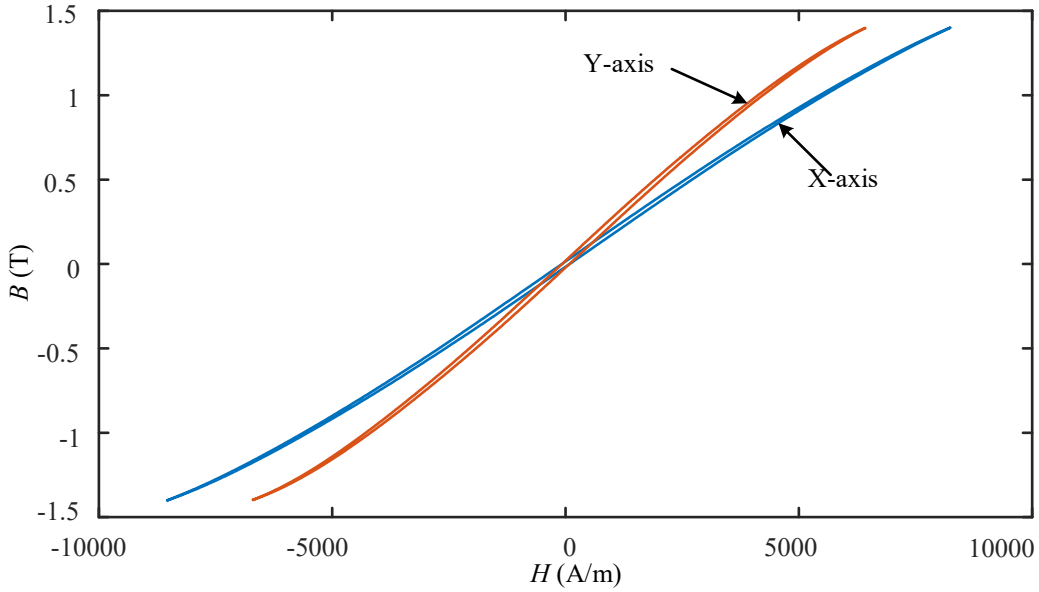

Fig. 5.9 *B-H* loops under alternating magnetic field at 50 Hz and peak value of magnetic flux density 1.40 T at X and Y-axes.

Fig. 5.9 shows the *B-H* loops in both directions with the peak value of 1.40 T under 50 Hz sinusoidal voltage excitation. It is observed from Fig. 5.9 that the *B-H* loops for X and Y-axes directions are slightly different. Therefore, the corresponding permeabilities are not the same which indicates that the selected magnetic material shows anisotropy property. The alternating loss always shows an increasing trend with the increase of B_m at any operating frequency as shown in Fig. 5.10.

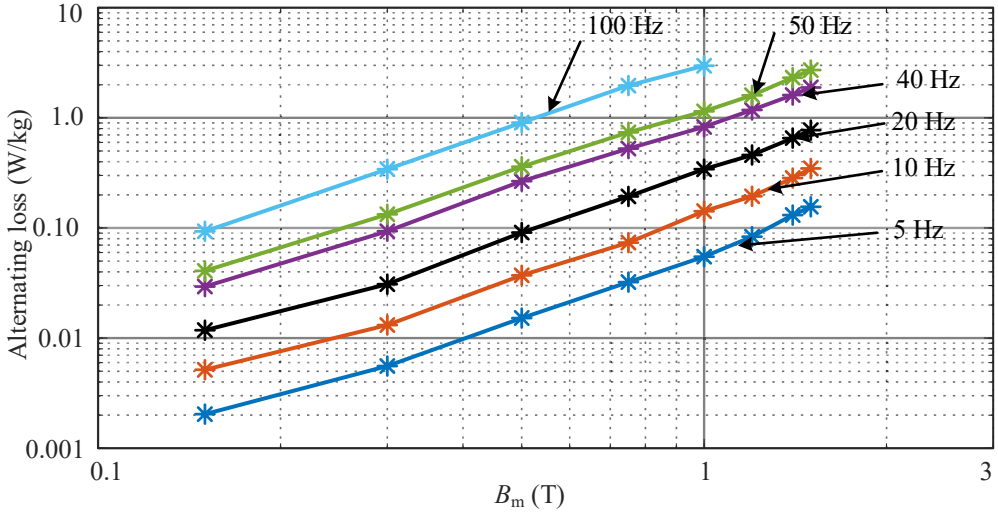

Fig. 5.10. Alternating core losses of the amorphous magnetic material with B_m for different frequencies.

Figs. 5.11 and 5.12 show the alternating and rotational core losses of the amorphous material at 50 Hz for different magnetic flux densities, respectively. From the figures, it is observed that the rotational core loss (P_r) is higher than the alternating core loss (P_{alt}) for the same value of B_m. It is observed from the measured core loss data that the ratio of the rotational and alternating core losses (P_r/P_{alt}) of the magnetic material at 50 Hz remains nearly 1.90 with some fluctuations for B_m up to 1 T, and after that it decreases dramatically. There are mainly two reasons for the significant reduction of the ratio: (i) the rotational hysteresis loss decreases dramatically at the vicinity to the saturation region, and (ii) the sharp increase of the alternating loss in the magnetic saturation region. In addition, the rotating excess loss coefficient changes slightly with the change of B_m (details in Section 5.4.3), which also affects the ratio.

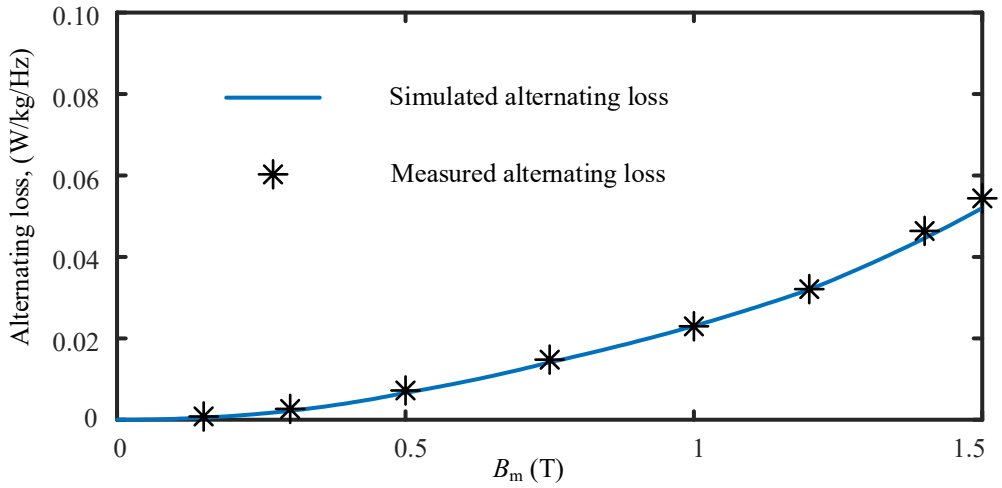

Fig. 5.11. The alternating core losses of the amorphous material with B_m under 50 Hz sinusoidal excitation.

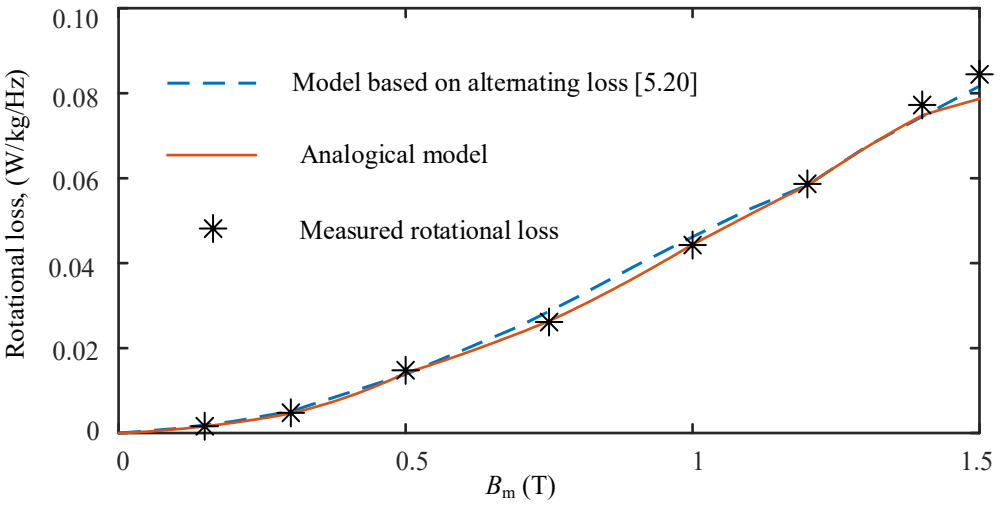

Fig. 5.12. The rotational core loss of the amorphous material with B_m under 50 Hz rotating magnetic field.

5.3.3 Core Loss under Elliptical Magnetic Field

For elliptically rotating magnetic field, the values of B_m at the major and minor axes of elliptical loci of **B** differ from each other. Consequently, both the rotational and alternating core losses exist in the total loss. Their shares in the total loss depend on the axis ratio of the loci of **B**. The elliptical loss is measured by keeping the major axes on one axis and the minor axes on the other axis as shown in Fig. 5.13.

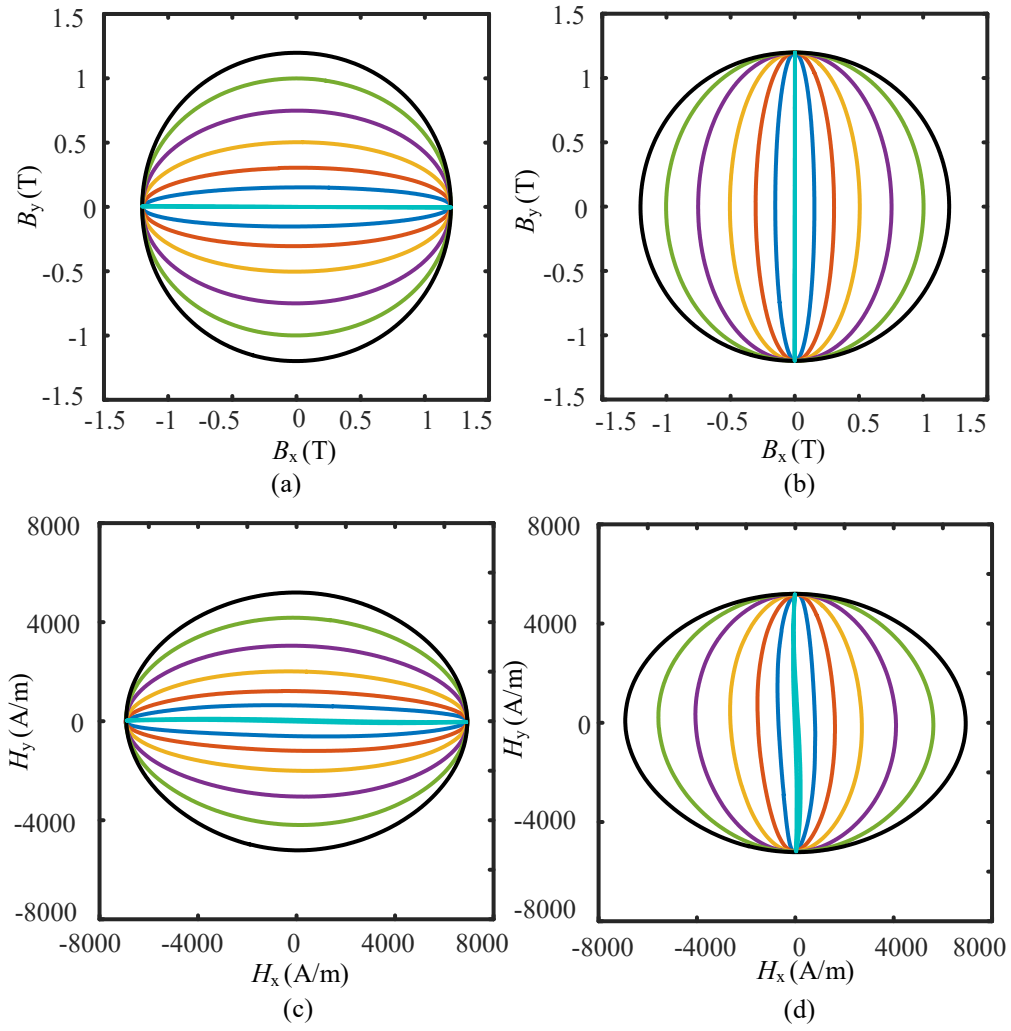

Fig. 5.13. Elliptical loci of **B** at 50 Hz when major axis is on (a) X-axis and (b) Y-axis, and the corresponding loci of **H** when major axis is on (c) X-axis and (d) Y-axis.

Fig. 5.14 shows the average elliptical loss with the axis ratio of the loci of **B**. In Fig. 5.14, B_m for the major axis is considered as 1.20 T, and B_m for the minor axis varies discretely from 0 to 1.2 T. From Fig. 5.14, it is observed that when only one of the axes is excited,

the loss becomes equal to the alternating core loss. After that the core loss increases with the increase of the axis ratio although the increasing trend is not linear. At the low value of the axis ratio, the loss changes slowly with the change of axis ratio but at a high value of the axis ratio the loss changes rapidly with the change of the axis ratio. When the minor and major axes of loci **B** are equal, the elliptical loss becomes equal to the circular rotational loss.

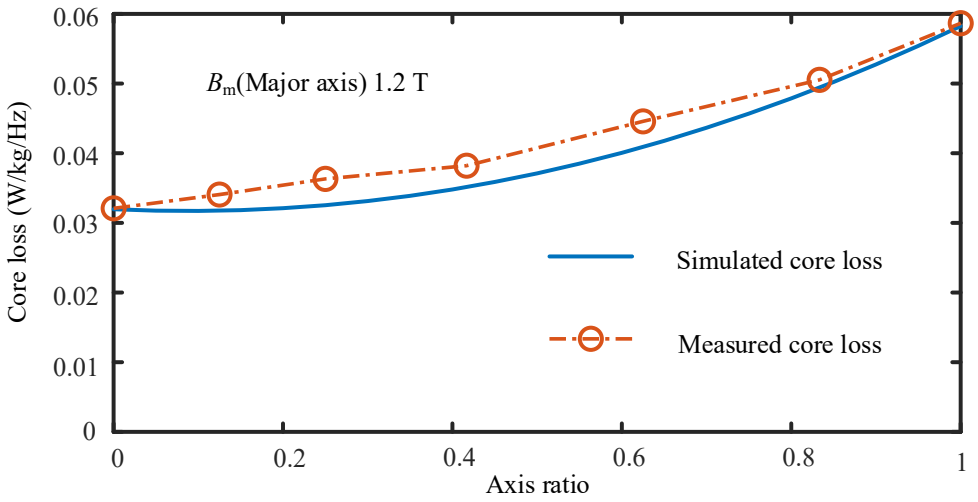

Fig. 5.14. Total core loss with different axis ratios at 50 Hz excitation.

5.4 Modelling of Circularly Rotational Losses

Loss separation method is exploited to model the core loss. In the loss separation method, hysteresis, eddy current and excess losses are modelled separately, and after that they are combined to obtain the total rotational core loss which are discussed below.

5.4.1 Rotational Hysteresis Model

5.4.1.1 Existing Rotational Hysteresis Models

It has already been discussed in introduction section that two types of empirical models are generally utilised to model the rotational hysteresis loss which are (i) an analogical approach-based model; and (ii) the alternating hysteresis loss-based model. The details of both models are discussed below.

In [5.2] and [5.23], it was reported that in spite of different mechanisms, there is an analogy between the patterns of the rotational hysteresis loss and the torque-slip curve of

a single-phase induction motor. Accordingly, a rotational hysteresis model was proposed in [5.23], which is based on the equation of torque-slip relation of a single-phase induction motor. By using the analogical approach, the rotational core loss per frequency P_{hr}/f can be modelled which is given by

$$P_{hr}/f = a_1\left[\frac{1/s}{\left(a_2+1/s\right)^2+a_3}-\frac{1/\left(2-s\right)}{\left\{a_2+1/\left(2-s\right)\right\}^2+a_3}\right] \tag{5.8}$$

where a_1, a_2 and a_3 are constant parameters, and the s is defined by

$$s = 1-\frac{M}{M_s}\sqrt{1-\frac{1}{a_2^2+a_3}} \tag{5.9}$$

where M is the amplitude of magnetisation vector **M (M=B/μ0-H)**, and M_s is the saturation magnetisation of a magnetic material. Since it can be generally considered as M >> H, M/M_s in (5.9) can be written as B_m/B_s. Accordingly, (5.9) can also be written as [5.18]

$$s = 1-\frac{B_m}{B_s}\sqrt{1-\frac{1}{a_2^2+a_3}} \tag{5.10}$$

Another method was postulated in [5.28], where the rotational core loss can be assumed as the sum of alternating losses in both axes under the same maximum magnetic flux density. Unfortunately, this approach cannot be used for rotational hysteresis loss as the rotational hysteresis loss at the vicinity of the saturation magnetic flux density shows different characteristic compared to that of alternating loss. To solve the problem, the method was modified in [5.24] where an approximate modification factor is included in the calculation as follows:

$$P_{\mathrm{hr}} = \left(1-a_{\mathrm{m}}\right)\left\{P_{ha}\left(B_{\mathrm{lm}}\right)+P_{ha}\left(B_{\mathrm{sm}}\right)\right\} \tag{5.11}$$

where P_{ha} is the alternating hysteresis loss in W/kg, and a_{m} is the modification factor calculated using measured data, B_{lm} and B_{sm} are the maximum magnetic flux densities in

major and minor axes, respectively. Since the magnetic flux densities in both directions are the same for circular rotating magnetic field, (5.11) can be written as

$$P_{hr} = 2\left(1 - a_m\right) P_{ha} . \tag{5.12}$$

According to [5.24], the value of a_m for the low magnetisation is considered as zero and for the rest part, it increases linearly up to one until full magnetic saturation. The modification factor of the Fe-based amorphous magnetic material for the alternating hysteresis loss-based rotational hysteresis loss model is shown in Fig. 5.15.

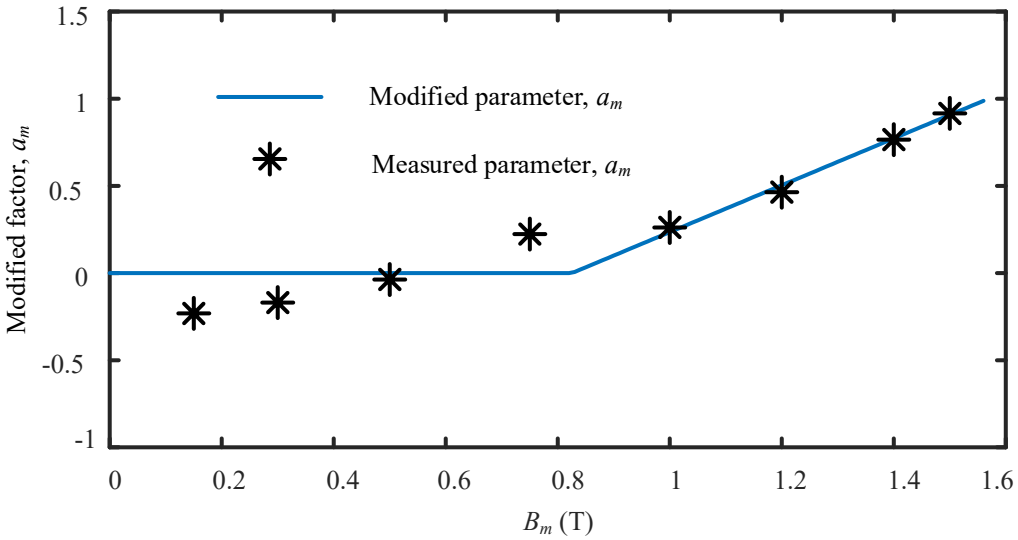

Fig. 5.15 Modification parameter a_m of the alternating hysteresis loss-based rotational hysteresis loss model.

5.4.1.2 Proposed Rotational Hysteresis Model

The proposed model is also an analogical approach, which is based on equation of mechanical power developed on a three-phase induction motor. The developed power in the three-phase induction motor can be calculated by

$$P_m = T_r \omega_r \tag{5.13}$$

where P_m is the developed mechanical power, T_r is the torque, and $\omega_r = (1\text{-}s)\omega_s$ is the angular speed of the rotor, ω_s synchronous angular speed of the three-phase induction motor. The torque can be written as [5.29]

$$T_r = \frac{3V_{th}^2 R_2 / s}{\omega_s \left[\left(R_{th} + R_2 / s \right)^2 + \left(X_{th} + X_2 \right)^2 \right]} \tag{5.14}$$

where V_{th}, R_{th} and X_{th} are the parameters related to the three-phase induction motor. From (5.13) and (5.14), one can write,

$$P = \frac{3\omega_r V_{th}^2 R_2 / s}{\omega_s \left[\left(R_{th} + R_2 / s \right)^2 + \left(X_{th} + X_2 \right)^2 \right]}. \tag{5.15}$$

If b_1, b_2 and b_3 are assumed for $3V^2_{th}/R_2$, R_{th}/R_2, $\{(X_{th}+X_2)/R_2\}^2$, respectively, by using analogical approach, the hysteresis loss per frequency (P_{hr}/f) can be obtained by

$$P_{hr}/f = \frac{b_1 (1 - s) s}{\left[\left(b_2 s + 1 \right)^2 + b_3 s^2 \right]} \tag{5.16}$$

where

$$s = 1 - \frac{B_m}{B_s} \tag{5.17}$$

From (5.16) and (5.17), it is observed that the proposed analogical rotational hysteresis loss model is more simplified approach than that of the existing analogical rotational hysteresis model [5.23], as shown in (5.8) and (5.9).

5.4.2 Modelling of Rotational Eddy Current Loss

Rotational eddy current loss appears due to the micro-eddy currents generated near to the moving domain walls. Since the thickness of the amorphous sheet is much smaller than that of silicon steel, the eddy current loss of the amorphous material slightly affects the total loss. Thus, the skin effect on the material in the low and medium frequency ranges can be neglected. For modelling of the rotational eddy current loss, the classical model can be used which is as follows [5.28]:

$$P_{er} = 2\frac{\sigma\pi^2 d^2}{6\rho} B_m^2 f^2 \tag{5.18}$$

where P_{er} is the rotational eddy current loss in W/kg, σ the conductivity of the amorphous sheet, d the thickness of amorphous sheet, f the frequency, ρ the mass density and B_m the maximum magnetic flux density. The conductivity is defined as reciprocal of resistivity. The resistivity of the amorphous material studied in this research is 130 μ .cm [5.7]. The value of mass density of the material is 7180 kg/m^3.

5.4.3 Modelling of Rotational Excess Loss

Rotational excess loss can be modelled by two ways: one is the conventional analytical model [5.23], and the other is obtained from measured alternating excess loss data [5.24]. In this study, the first one, i.e. conventional excess loss model is incorporated with the analogical rotational hysteresis model. The conventional rotational excess or anomalous loss P_{ar} (W/kg) can be obtained by

$$P_{ar} = C_{ar} B_m^{1.5} f^{1.5} \tag{5.19}$$

where C_{ar} is the rotational excess loss coefficient. Therefore, the total rotational core loss can be obtained as follows:

$$P_r = P_{hr} + 2\frac{\sigma\pi^2 d^2}{6\rho} B_m^2 f^2 + C_{ar} B_m^{1.5} f^{1.5} \tag{5.20}$$

where both P_{hr} and C_{ar} are unknowns which can be obtained by extrapolation and curve fitting of the measured core losses. Fig. 5.16 shows the curve fitting of the measured core losses per frequency (P_r/f) with f for different B_m, where P_r is obtained from (5.20). The separation of the rotational hysteresis loss from the total loss at different magnetic flux densities is also observed in Fig. 5.16. Thus, C_{ar} and P_{hr} for the whole magnetic flux density range can be obtained as shown in Figs. 5.17 and 5.18, respectively. From Fig. 5.17, it is observed that rotating excess loss coefficient changes with the magnetic flux density. Consequently, the change of excess loss coefficient with magnetic flux density

affects the total core loss as well as the ratio of rotating and alternating core losses. In addition, it is observed from Fig. 5.16 that the lines for hysteresis loss and eddy current loss plus hysteresis loss seem overlapping to each other which indicates that the effect of eddy current loss of the amorphous material is very small.

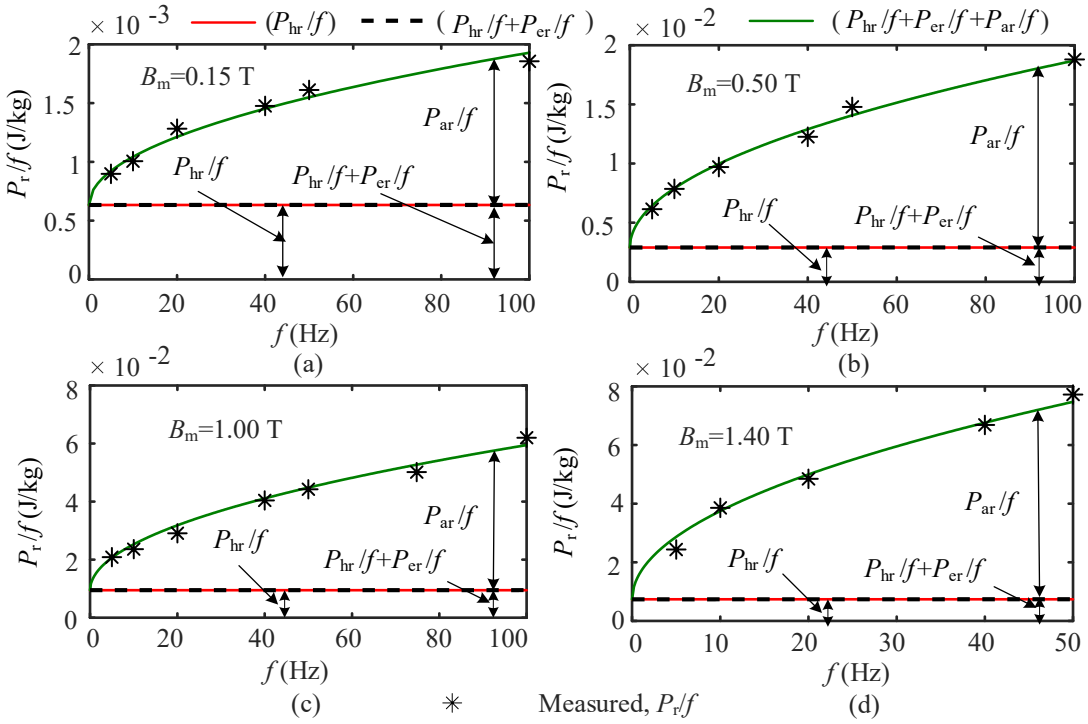

Fig. 5.16. Curve fitting of the measured core loss data with frequency for different maximum magnetic flux densities, e.g. (a) 0.15 T, (b) 0.50 T, (c) 1.00 T and (d) 1.40 T.

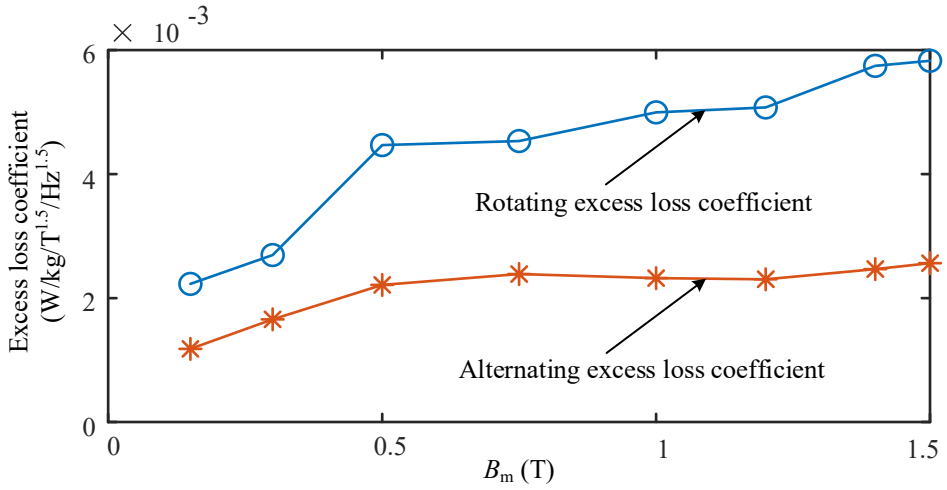

Fig. 5.17. Rotating and alternating excess loss coefficients with magnetic flux density.

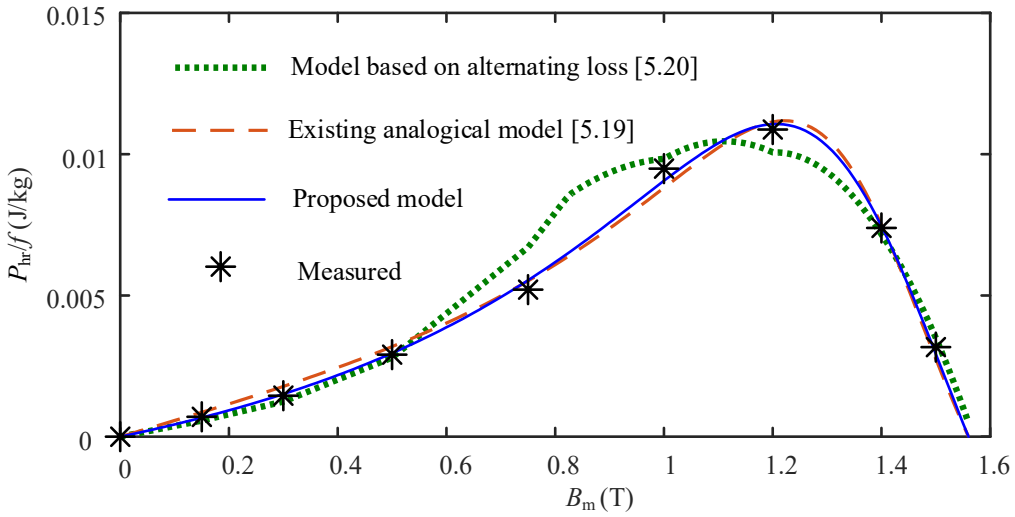

Fig. 5.18. Comparison of different models for modelling rotational hysteresis loss of the amorphous magnetic material.

In the second method, the rotational excess loss can be directly obtained from the alternating excess loss which is as follows:

$$P_{ar} = 2\left(1-a_e\right)P_{aa} \tag{5.21}$$

where P_{ar} is the rotational excess loss, P_{aa} is the alternating excess loss and a_e is the modification factor for the excess loss. Alternating excess loss can be obtained by subtracting the alternating hysteresis and eddy current losses from the total alternating loss. The value of factor a_e is determined as the same as the factor for the rotational hysteresis loss as discussed in Section 5.4.1.1.

5.5 Modelling of Alternating Core Loss

The loss separation method is also used for modelling of the alternating core loss. The alternating eddy current and excess losses are modelled as the same as the rotational core loss modelling. As the total loss is the sum of hysteresis, eddy current and excess losses, the total alternating loss P_{alt} can be expressed as

$$P_{\text{alt}} = P_{\text{ha}} + \frac{\sigma\pi^2 d^2}{6\rho} B_{\text{m}}^2 f^2 + C_{\text{aa}} B_{\text{m}}^{1.5} f^{1.5} \tag{5.22}$$

where C_{aa} is the alternating excess loss coefficient. The calculations of the P_{ha} and C_{aa} are carried out as the same as that for the rotational core loss. The calculated alternating excess loss coefficient with magnetic flux density is shown in Fig. 5.17. From this figure, it is seen that the rotating excess loss coefficient is higher than the alternating excess loss coefficient. In the low magnetic flux density region, e.g., up to 0.5 T, both coefficients increase but after that the alternating excess loss coefficient becomes almost constant. On the other hand, the rotating excess loss coefficient shows an increasing trend. The pattern of the alternating hysteresis loss is quite different from the rotational hysteresis loss especially at the situation near to B_s. Thus, the modelling of the alternating hysteresis loss is not carried out as the same as the rotational hysteresis loss. In this research, the alternating hysteresis loss is modelled by the following Steinmetz equation [5.30], [5.31]:

$$P_{ha} = C_{ha} B_m^{\beta} f \tag{5.23}$$

where C_{ha} and β are the Steinmetz parameters which are obtained by curve fitting of hysteresis loss data.

5.6 Modelling of Elliptical Core Loss

The elliptical rotational core loss model was done by an analytical approach reported in [5.23]. In the analytical approach, some assumptions are considered such as the ratio of minor and major axes of loci of **B** is equal to that of loci of **H**, and the components of **B** and **H** on both axes are sinusoidal. The expression of elliptical loss is then written as [5.23]:

$$P_t = R_B P_r + \left(1 - R_B\right)^2 P_{alt} \tag{5.24}$$

where R_B is the ratio of minor and major axes of the elliptical **B** loci.

5.7 Experimental Verification of Modelling of Core Losses

This section presents the experimental verification of the proposed rotational hysteresis loss model, and compares it with other models. Accordingly, the modellings of the rotational loss, alternating loss and elliptical core losses are also carried out and

experimentally verified.

The proposed rotational hysteresis model is verified by curve-fitting the rotational hysteresis losses with respect to the B_{m}. To assess the accuracy of the model, the error is defined as follows [5.23]:

$$Err = \frac{\sqrt{\frac{1}{N-1}\sum_{i=1}^{N}\left(P_{i(\mathrm{test})} - P_{i(\mathrm{cal})}\right)^2}}{\max\left(P_{i(\mathrm{test})}\right)} \tag{5.25}$$

where σ is the standard deviation, N is number of measured data, $P_{i(\mathrm{test})}$ the measured data and $P_{i(\mathrm{cal})}$ the calculated data. The optimisation technique with considering the minimum error is applied for calculating the parameters of analogical rotational hysteresis models. The above-mentioned hysteresis models are applied to model the amorphous magnetic material. Fig. 5.18 (Section 5.4.3) shows the comparison among their results with the measured values. It is observed from Fig. 5.18 that the proposed model achieves a better agreement with the measured values than other models. The error for the proposed model is 2.11% whereas it is 3.55% and 6.42% for the existing analogical model and alternating loss-based model, respectively.

To achieve high power density, transformer and electrical machines are generally operated near to the saturation magnetic flux density. From the Fig. 5.7, it is observed that loci of **B** at high magnetic induction levels become slightly distorted form being exact circle. It happens due to the influence of saturation in high magnetic induction especially at near to the saturation magnetic flux density. From Fig. 5.18, it is observed that the rotational hysteresis loss in this region decreases with increase of magnetic induction level. However, excess and eddy current losses increase with increase of magnetic induction level.

Fig. 5.12 (Section 5.3.2) shows the comparison among the simulation results and experimental results of the rotational core losses. It is observed from Fig. 5.12 that the analogical approach achieves a better agreement with the experimental results than the alternating loss-based approach.

Fig. 5.11 (Section 5.3.2) shows the simulated and measured alternating losses. It is observed from Fig. 5.11 that the simulated results are close to the measured results. For the elliptical core loss, the simulation results also agree with the experimental results, although there exist small errors in the middle range of the axis ratio as shown in Fig. 5.14 (Section 5.3.3). As the analytical model, which is used for the simulation, is based on some approximations discussed in Section 5.6, it shows small errors with the experimental results especially in the middle of the axis ratio range. In addition, in both rotational and alternating excess loss models, the excess loss is considered to be proportional to $(B_m f)^{3/2}$ as shown in (5.20) and (5.22), which is not a generalised approach for all types of magnetic materials as a perfect alignment of magnetic domains of the magnetic materials with magnetic field is hardly possible. Therefore, the aforementioned excess loss model introduces a small error in the calculation of core loss. Moreover, in this research the effect of temperature change, mechanical stress, and change of annealing process have not been considered in the measurement and modelling processes

5.8 Conclusion

Two-dimensional magnetic properties of the selected Fe-based amorphous magnetic material are measured and investigated under different excitation conditions. From the investigation, some remarkable results have been obtained, which are: (i) the rotational hysteresis loss of the amorphous magnetic material decreases at the vicinity of the saturated magnetic flux density which is similar to that of the silicon steels; (ii) the permeability differs slightly with the change of the direction of the magnetic field; (iii) the ratio of the rotational to alternating core losses is about 1.90, and decreases dramatically at the vicinity of saturation magnetic flux density; and (iv) for elliptical rotational core loss, the small change of axis ratio near to the peak axis ratio highly affects the total core loss. In addition, a simple improved rotational hysteresis loss model is proposed and experimentally verified. It is also observed that the proposed model achieves a better agreement with measured data compared to others. Moreover, alternating and elliptical rotating core losses are modelled and compared with the measured results.

References

[5.1] J. C. Akiror, J. Wanjiku, P. Pillay, J. Cave, and A. Merkhouf, "Rotational core loss magnetizer: design and measurements," *IEEE Trans. Ind. Appl., vol.* 54, no. 5, 4355–4364, Sep.-Oct. 2018.

[5.2] J. G. Zhu, "Numerical modelling of magnetic materials for computer aided design of electromagnetic devices," *Ph.D. Dissertation*, School of Electrical Engineering, University of Technology Sydney, Australia, July 1994.

[5.3] N. Ertugrul, R. Hasegawa, W. L. Soong, J. Gayler, S. Kloeden, and S. Kahourzade, "A novel tapered rotating electrical machine topology utilizing cut amorphous magnetic material," *IEEE Trans. Magn.,* vol. 51, no. 7, Jul. 2015, Art. 8106006.

[5.4] Z. Wang, *et al*., "Development of a permanent magnet motor utilizing amorphous wound cores," *IEEE Trans. Magn., vol.* 46, no. 2, pp. 570–573, Feb. 2010.

[5.5] S. Kahourzade, N. Ertugrul, and W. L. Soong, "Loss analysis and efficiency improvement of an axial-flux PM amorphous magnetic material machine," *IEEE Trans. Ind. Electron*., vol. 65, no. 7, pp. 5376–5383, Jul. 2018.

[5.6] Henan ZY Amorphous Technology Co. Ltd. [Online]. Available: https://www.zyamorphous.com/. Accessed on. 25 Jul. 2020.

[5.7] Guangzhou Amorphous Electronic Technology Co. Ltd. [Online]. Available: https://coilcore.en.alibaba.com/. Accessed on. 22 Dec. 2020.

[5.8] F. G. Baily, "The hysteresis of iron and steel in a rotating magnetic field," *Phil. Trans. Royal Soc. A*, pp. 715–746, 1896.

[5.9] Basak and A. J. Moses, "Influence of stress on rotational loss in silicon iron," *Proc. IEE,* vol.125, no.2, pp. 165–168, Feb. 1978.

[5.10] J. Sievert, H. Ahlers, M. Enokizono, S. Kauke, L. Rahf, and J. Xu, "The measurement of rotational power loss in electrical sheet steel using a vertical yoke system," *J Mag. Magn. Mat*., vol. 112, no. 1–3, pp. 91–94, July 1992.

[5.11] Kaplan, "Magnetic core losses resulting from a rotating flux," *J. Appl. Phys*., vol. 32, no.3, pp. 370s–371s, Mar. 1961.

[5.12] F. Brailsford, "Rotational hysteresis loss in electrical sheet steels," *J. Inst. Elect. Engrs.*, vol. 83, no. 502, pp. 566–575, Oct. 1938.

[5.13] M. Enokizono, T. Todaka, T. Sashikata, J. D. Sievert, and H. Ahlers, "Magnetic field analysis of rotational loss tester with vertical yoke," *J. Mag. Magn. Mat*., vol. 112, no. 1–3, pp. 81–84, Jul. 1992.

[5.14] W. Brix, K. Hempel, and F. Schulte, "Improved method for the investigation of the rotational magnetization process in electrical steel sheets," *IEEE Trans. Magn., vol.* 20, no. 5, pp. 1708–1710, Sep. 1984.

[5.15] P. J. Flanders, "The rotating-sample magnetometer," *J. Appl. Phys.,* v. 38, no. 3, pp. 1293-1294, Mar 1967.

[5.16] X. Ding and S. Ren, "Accuracy analysis of sensing coils in 2-D magnetic properties measurement," *IEEE Trans. Magn.*, vol. 54, no. 11, pp. 1–5, Nov. 2018, Art no. 6100905.

[5.17] S. Zurek, P. Marketos, T. Meydan, and A. J. Moses, "Use of novel adaptive digital feedback for magnetic measurements under controlled magnetizing conditions," *IEEE Trans. Magn.*, vol. 41, no. 11, pp. 4242–4249, Nov. 2005.

[5.18] Y. G. Guo, J. G. Zhu, and J. J. Zhong, “Measurement and modelling of magnetic properties of soft magnetic composite material under 2D vector magnetisations,” *J. Mag. Magn. Mat.,* 302, no. 1, pp. 14–19, Jul. 2006.

[5.19] M. Enokizono, T. Suzuki and J. D. Sievert, “Measurement of iron loss using rotational magnetic loss measurement apparatus,” *IEEE Trans. J. Magn. Jpn.*, vol. 6, no. 6, pp. 508–514, Jun. 1991.

[5.20] Cecchetti, G. Ferrari, F. Masoli, and G. Soardo, “Rotational power losses in 3% SiFe as a function of frequency,” *IEEE Trans. Magn*., vol. 14, no. 5, pp. 356–358, Sep. 1978.

[5.21] S. Ueno, T. Todaka, and M. Enokizono, “Measurement of vector magnetic properties of Fe–Si–B amorphous material,” *IEEE Trans. Magn*., vol. 47, no. 10, pp. 3188–3191, Oct. 2011.

[5.22] M. Enokizono, G. Shirakawa, and J. Sievert, “Anomalous anisotropy and rotational magnetic properties of amorphous sheet,” *J. Magn. Magn. Mater*., vol. 112, no. 1–3, pp. 195–199, Jul. 1992.

[5.23] J. G. Zhu and V. S. Ramsden, “Improved formulations for rotational core losses in rotating electrical machines,” *IEEE Trans. Magn., vol.* 34, no. 4, pp. 2234–2242, July 1998.

[5.24] Y. Gao, *et al*., “Simple numerical calculation method of rotational iron loss in silicon steel sheets,” *IEEE Trans. Magn.,* vol. 55, no. 6, Jun. 2019, Art. 6300404.

[5.25] J. G. Zhu and V. S. Ramsden, “Two dimensional measurement of magnetic field and core loss using a square specimen tester,” *IEEE Trans. Magn.,* vol. 29, no. 6, pp. 2995–2997, Nov. 1993.

[5.26] S. Zurek, “Two-dimensional magnetisation problems in electrical steels,” *Thesis Dissertation*, Wolfson Centre for Magnetics Technology, Cardiff School of Engineering, Cardiff University, UK, Mar. 2005.

[5.27] LTC 1151, Dual ±15 V zero-drift operational amplifier, Linear Technology. Online access: July 3, 2020, Available on: https://www.analog.com/media/en/technical-documentation/data-sheets/1151fa.pdf

[5.28] T. Yamaguchi and K. Narita, “Rotational power loss in commercial silicon-iron laminations,” *Elect. Eng. Jpn*, vol. 96, no. 7, pp. 15–21, 1976.

[5.29] S. J. Chapman, Eelectric Machinery Fundamentals, Induction Motor, 5th Edition, McGraw Hill, New York, Feb. 2011.

[5.30] C. P. Steinmetz, “On the law of hysteresis,” *Trans. American Ins. Elect. Engr.*, no. 1, pp. 1–64, Jan. 1892.

[5.31] K. Venkatachalam, C. R. Sullivan, T. Abdallah, and H. Tacca, “Accurate prediction of ferrite core loss with nonsinusoidal waveforms using only Steinmetz parameters,” *in Proc. IEEE Workshop Comp. Power Electron.*, Mayaguez, Puerto Rico, USA, Jun. 3–4, 2002, pp. 36–41.

Chapter 6 Design of Medium Frequency Transformer

6.1 Introduction

In the last few decades, the multi-stage energy conversion techniques such as solid-state transformer (SST) are getting attentions in energy conversion systems [6.1]. The SSTs are also used for power flow regulation and galvanic isolation [6.2], [6.3]. Low volume and low weight SSTs are generally demanded in the different energy conversion systems such as power grid connected converters, solar and wind farms, and tractions. One of the components of the SSTs is the DC-DC converter in which transformers are mainly used to provide galvanic isolation, and to change the voltage levels in the energy conversion systems. To reduce the size and weight of the transformers, the operating frequency and magnetic flux density of the transformers are generally required to be high as the cross-sectional area of the transformer core mainly depends on the frequency and magnetic flux density. Thus, the high-power density can be obtained by increasing the operating frequency and magnetic flux density.

One of the disadvantages of SST is that an additional loss known as switching loss occurs in the system, and it increases with the increase of the frequency. Therefore, the increase of the switching frequency of SST decreases the efficiency of the DC-DC converter. Moreover, the nonsinusoidal excitation voltage such as square wave voltage is generally applied on the transformer of SST. As a result, harmonics, which are also related with the switching frequency, are generated in SST based systems, and affect the power quality and efficiency [6.2]. Accordingly, in this chapter, the switching frequency of 1 kHz is used so that it remains under the design requirement of harmonic contents of SST.

The selection of core material of the MFT transformer in the DC-DC converter is important as the core loss highly affects the efficiency of the MFT. There are many core materials, e.g., amorphous magnetic material, silicon steel, nanocrystalline magnetic material and ferrite, which are normally used in SSTs. The amorphous magnetic materials are suitable for medium frequency ranges [6.4], [6.5]. Among different amorphous magnetic materials such as Fe-based, Co-based, and Ni-based amorphous materials, the Fe-based magnetic material shows the highest maximum magnetic flux density.

Accordingly, in this chapter, the Fe-based amorphous magnetic material is used as the core material.

The optimal design of an MFT is a multi-objective problem. Improvement of one objective by changing the design variables may affect the other objectives. For instance, the increase of operating magnetic flux density increases the power density and reduces the volume, and at the same time the efficiency decreases as the core loss increases with the increase of the magnetic flux density. In the literature, it is observed that many optimal designs were proposed, and each design focused on a specific design variable or objective of the multi-objective problem such as the ripple voltages [6.1], the isolation requirement [6.6]−[6.8], thermal models [6.9], heuristic optimisation technique [6.10], and Litz wire modelling for leakage inductance [6.11], [6.12], and winding loss modelling [6.13]. To achieve the high-power density, the transformer is generally operated at high magnetic flux density. At the same time, the number of the turns in the windings are also kept low in order to decrease winding losses. The low number of turns in excitation winding increases the value of the no-load current which is mainly responsible for the magnetisation of the windings. The no-load current becomes significant if the transformer operates in low and medium power ranges. The no-load current of the transformer actually affects the winding loss and leakage inductance of the windings. The empirical core loss model-based design of medium frequency transformers with the effect of no-load current, which is the vector sum of magnetising and core loss equivalent current, is not found in the literature. Based on the optimal design consideration, a prototype of a 2.5 kW, 1 kHz MFT is considered, and that prototype is used for experimental verification of the design.

6.2 Modelling of MFT

A design approach of an MFT requires mathematical expressions. Thus, before applying the optimisation technique, different analytical and empirical expressions of all transformer design prospects are firstly required to be modelled. In this section, the modellings of different design prospects of MFT are discussed.

6.2.1 Core Loss

The determination of the core loss of magnetic material is important in the design process as it largely affects the efficiency. The empirical methods of the core loss are generally chosen, as they reduce the computational cost significantly. Since the excitation voltage is not sinusoidal, the original Steinmetz equation is not utilised for core loss prediction [6.14]–[6.16]. For non-sinusoidal excitation, other empirical models such as generalised Steinmetz equation (GSE) [6.15], improved generalised Steinmetz equation (IGSE) [6.16], natural Steinmetz equation (NSE) [6.17], and waveform coefficient Steinmetz equation (WCSE) [6.18] can be used. Depending on the accuracy, the IGSE model is used for prediction of the core loss which is obtained by following equation.

$$P = \frac{1}{T}\int_{0}^{T} k_i \left|\frac{\mathrm{d}B(t)}{\mathrm{d}t}\right|^{\alpha} (\Delta B)^{\beta-\alpha}\,\mathrm{d}t \tag{6.1}$$

where

$$k_i = \frac{K}{(2\pi)^{\alpha-1}\int_{0}^{2\pi} \left|\cos(\theta)\right|^{\alpha} 2^{\beta-\alpha}\, d\theta} \tag{6.2}$$

and $\Delta\beta$ is the peak to peak amplitude of the magnetic flux density, and K, α and β are the Steinmetz coefficients of the OSE. The coefficients of K, α and β are calculated by curve fitting of measured core loss data [6.19] under sinusoidal excitation with OSE equation [6.14], [6.16] which is as follows:

$$P_s = Kf^{\alpha}B^{\beta} \tag{6.3}$$

where, P_s is the calculated power loss. A rectangular shape of amorphous core (uncut AMCC 50 [6.20] which consists of amorphous 1k101 strips) is considered for calculation of Steinmetz coefficients. The process of the measurement of core losses of the magnetic core at different magnetic flux densities is detailed in Chapter 3.

6.2.2 Core Geometry

Different core shapes, e.g., double C-core and EE-core, are generally used in medium frequency transformer. The double C-core is generally core-type transformer, and the EE-core is shell type transformer. The leakage inductance in the shell type transformers is less than that in the core type transformers. Moreover, since the whole primary and secondary windings are generally wound in only one limb of the EE core, the insulation requirement in EE-core based transformer is also higher than that of the double C-core type transformer. Thus, the double C-core transformer is selected in this study. The typical double C-core type magnetic core is shown in Fig. 6.1. In order to reduce the leakage inductance of the transformer, halves of both primary and secondary windings are wound in the same limb, and the other halves are wound in another one. Two important parameters of the core are the cross-sectional areas and core window area. The cross-section of the core depends on the operating magnetic flux density, frequency, the number of the turns and excitation voltage, which is expressed as follows:

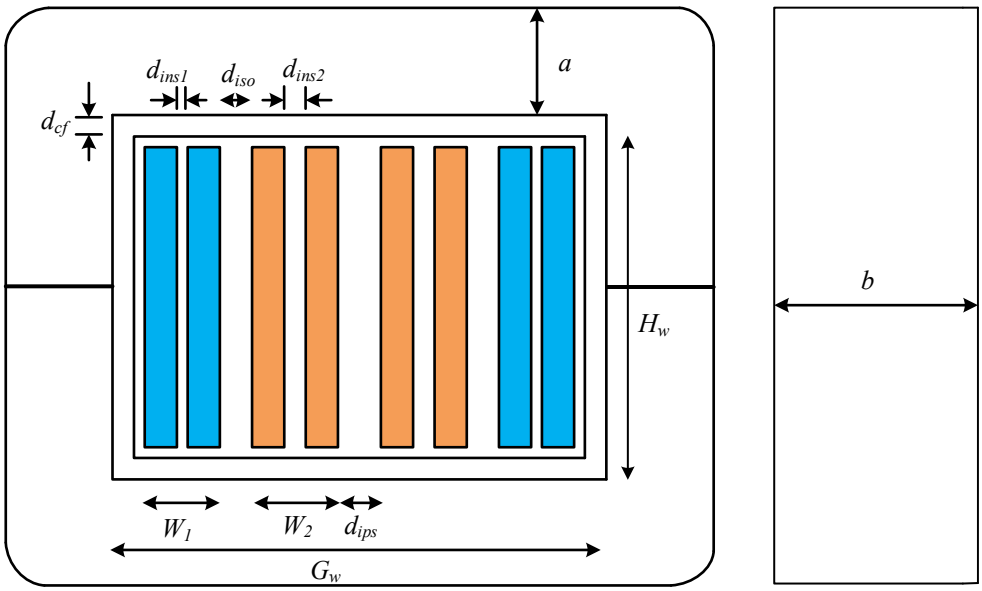

Fig. 6.1. Design sketch of a double C-core type MFT (Only inside conductors are shown).

$$A_c = \frac{V_1}{K_f K_s N_1 B_m f} \tag{6.4}$$

where A_c is the cross-sectional area of the core which is the product of core bread and core height, K_f the form factor, K_s the stacking factor of the core, N_1 the half number of turns of the primary winding, B_m maximum magnetic flux density, V_1 the half of primary voltage, and f the frequency. The window cross sectional area, which is the product of the window height (H_w) and window width (G_w), mainly depends on the primary and secondary winding cross-sectional areas and insulation thickness. The core window width can be obtained by

$$G_w = 2\left(W_1 + W_2 + d_{iso} + d_{cf}\right) + d_{isa} \tag{6.5}$$

where G_w is the window width, W_1 the primary half winding width, W_2 the secondary half winding width, d_{iso} the insulation thickness between the primary and secondary half windings, d_{cf} the insulation thickness between core and the nearest winding, and d_{isa} is the insulation thickness between outer windings of the limbs as shown in Fig. 6.1. The primary and secondary half winding widths can be expressed by

$$W_1 = p_1 d_{w1} / K_{u1} + \left(p_1 - 1\right) d_{ins1} \tag{6.6}$$

$$W_2 = p_2 d_{w2} / K_{u2} + \left(p_2 - 1\right) d_{ins2} \tag{6.7}$$

where p_1 and p_2 are numbers of winding layers of primary and secondary half winding, d_{ins1} and d_{ins2} are the insulation thickness between two layers in the primary and secondary windings, K_{u1} and K_{u2} are the utilisation factors. Similarly, the core window height can be obtained as follows:

$$H_w = N_{l1} d_{w_1} / K_{uh} + 2d_{cf} \tag{6.8}$$

where N_{l1} is the number of the turns per layer in the excitation winding and K_{uh} is the utilisation factor.

6.2.3 Insulation Design

Proper insulation among core limb, primary, secondary winding and inter winding turns are necessary to prevent the electrical breakdown of the transformer. For medium frequency transformers, dry type insulation is generally used. The minimum insulation distance between conductors is calculated by [6.2]

$$d_{ins} = \frac{V_{ins}}{\nu E_{ins}} \tag{6.9}$$

where d_{ins} is the insulation distance, ν the safety factor, V_{ins} the voltage needed to be insulated, and E_{ins} the dielectric strength of the insulating medium. Similarly, all the insulation thickness such as $d_{\text{ins}1}$, $d_{\text{ins}2}$, d_{iso}, d_{isa}, and d_{cf} can be calculated by (6.9).

6.2.4 Winding Wire Selection

In this study, Litz wire is used as winding wire to decrease the effect of eddy current on the coils. There are many types of Litz wires, such as AWG 28 and AWG 30, depending on the operating frequency ranges. AWG 28 is generally used for frequency range from 60 Hz to 1 kHz, and AWG 30 is used for frequency range from 1 kHz to 10 kHz. Since, the excitation current contains harmonics, the AWG 30 is used to reduce further eddy current due to harmonics. The Litz wire consists of many strand conductors, and is generally covered by insulation. Therefore, the diameters of the Litz wires can be written for both windings as follows [6.21]:

$$d_{w1} = 1.154\sqrt{N_{s1}}d_{s1} + 2t_1 \tag{6.10}$$

$$d_{w2} = 1.154\sqrt{N_{s2}}d_{s2} + 2t_2 \tag{6.11}$$

where d_{w1} and d_{w2} are diameters of the primary and secondary Litz wires, d_{s1} the strand diameter of primary Litz wire, d_{s2} strand diameter of secondary Litz wire, N_{s1} and N_{s2} are numbers of strands in primary and secondary Litz wire, t_1 the insulation thickness of the primary Litz wire, and t_2 the insulation thickness of the secondary Litz wire.

6.2.5 Consideration of Transformer's No-Load Current

The no-load current mainly rises in the transformer due to the magnetisation of the magnetic material. The no-load current is then superimposed on the primary current. The magnetic flux in the magnetic core of a transformer is almost constant whatever the load conditions, and it is approximately equal as at no-load condition [6.22]. Therefore, the magnetic field strength of a transformer can be calculated using the no-load current as shown in (6.12). If the magnetic flux density is known, the corresponding magnetic field strength can be easily calculated from the magnetisation curve of the magnetic material. Fig. 6.2 shows the magnetisation curve of a Fe-based magnetic material (uncut AMCC 50 [6.20]). The magnetic field strength can be expressed by (6.12) which is as follows:

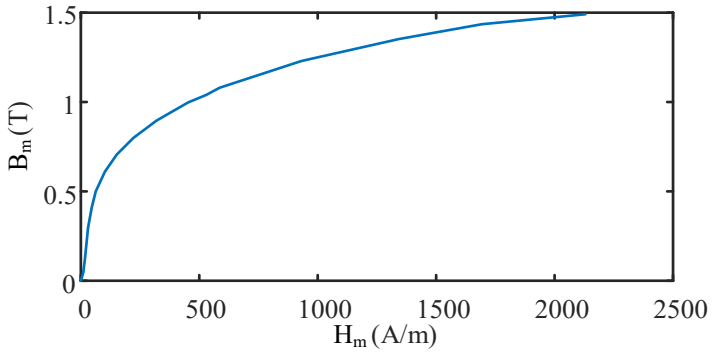

Fig. 6.2. *B-H* curve of the selected AMCC 50 core.

$$H_m = \frac{2\sqrt{2}N_1 I_0}{L_{ml}} \tag{6.12}$$

where H_m is the maximum magnetic field strength, I_0 the no-load current (rms), L_{ml} the effective magnetic flux path and N_1 the number of turns in the primary half winding. From (6.12), one can write

$$I_0 = \frac{H_m L_{ml}}{2\sqrt{2}N_1} \ . \tag{6.13}$$

Therefore, (6.13) can be used for calculation of the no-load current of any transformer. As the no-load current is vectorially added with the primary current, the resultant primary current can be written as [6.22]:

$$I_p = \sqrt{I_0^2 + I_p'^2 + 2I_0 I_p' \cos\varphi} \tag{6.14}$$

where I_p is the primary current, I_p' the equivalent load current in the primary winding, and φ the angle between I_p' and I_0.

6.2.6 Winding Losses

For winding loss calculation, the AC resistances of the windings are firstly determined. To acquire the AC resistances of the windings, the Litz wires need to be modelled. For modelling the Litz wire, the strands in the Litz wire are considered as an arrangement of $\sqrt{N_s} \times \sqrt{N_s}$ where N_s is the number of strands of the Litz wire, as shown in Fig. 6.3 [6.23]. In addition, the round conductor is converted to equivalent rectangular conductor. Dowell's expression [6.24] is then applied to calculate the AC resistance. The expression of AC resistance of the Litz wire of the primary winding is given below [6.5],

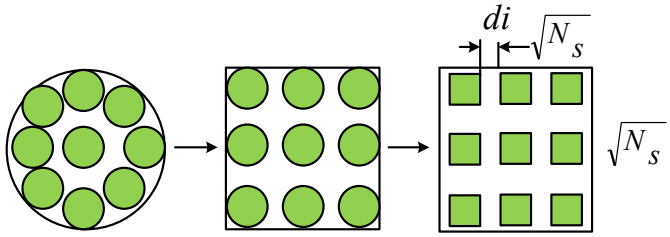

Fig. 6.3. Conversion method of a Litz wire to several layers for calculation of AC resistance [6.23].

$$R_{ac1} = 2R_{dc1}\Delta_1 \left[\frac{\sinh 2\Delta_1 + \sin 2\Delta_1}{\cosh 2\Delta_1 - \cos 2\Delta_1} + \frac{2(N_{s1}p_1^2 - 1)}{3} \frac{\sinh \Delta_1 - \sin \Delta_1}{\cosh \Delta_1 + \cos \Delta_1} \right] \tag{6.15}$$

where $\Delta_1 = \frac{d_{s1}}{2\delta} \sqrt{\frac{\pi N_{l1} d_{s1} \sqrt{\pi N_{s1}}}{2H_w}}$,

and d_{s1} is the diameter of a strand, $\delta = \sqrt{1/(\pi\sigma f \mu)}$ is the skin depth, σ is the conductivity, R_{dc1} is the primary half winding DC resistance, and f is the frequency. Similarly, the expression of secondary AC resistance is obtained as follows:

$$R_{ac2} = 2R_{dc2}\Delta_2\left[\frac{\sinh 2\Delta_2 + \sin 2\Delta_2}{\cosh 2\Delta_2 - \cos 2\Delta_2} + \frac{2(N_{s2}p_2^2 - 1)}{3}\frac{\sinh \Delta_2 - \sin \Delta_2}{\cosh \Delta_2 + \cos \Delta_2}\right] \tag{6.16}$$

where $\Delta_2 = \frac{d_{s2}}{2\delta}\sqrt{\frac{\pi N_{l2} d_{s2}\sqrt{\pi N_{s2}}}{2H_w}}$.

Therefore, the winding loss can be calculated by

$$P_{ac} = I_p^2 R_{ac1} + I_s^2 R_{ac2} \tag{6.17}$$

where I_p indicates current in primary winding and I_s indicates current in secondary winding.

6.2.7 Leakage Inductance

Just like the model of AC resistance of the Litz wire, the strands are arranged as $\sqrt{N_s} \times \sqrt{N_s}$ patterns and converted to rectangular equivalent for the modelling of the leakage inductance as shown in Fig. 6.4. Due to the presence of the magnetic field, the magnetic energy is stored in the conductor and insulation, which is responsible for the leakage inductance. For the conducting part, Dowell's expression [6.24] is used to calculate the leakage inductance, and for the insulation part the calculation of the leakage inductance is carried out by calculating magnetic stored energy in the insulation [6.25]. Thus, the leakage inductance for the round Litz wire can be calculated by the following equation:

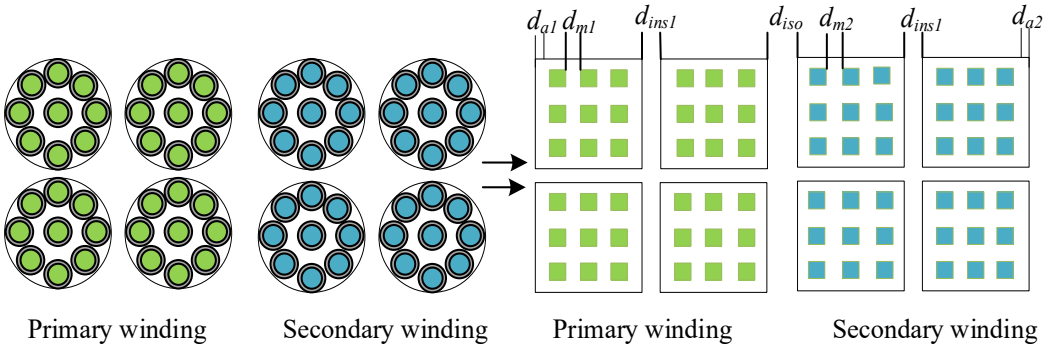

Fig. 6.4. Conversion method of a Litz wire-based transformer windings to several layers for calculation of leakage inductance.

$$L_{lP}=\frac{2R_{dc1}}{\omega}\Delta_1\left[\frac{\sinh 2\Delta_1-\sin 2\Delta_1}{\cosh 2\Delta_1-\cos 2\Delta_1}+\frac{2(N_{s2}p_2^2-1)}{3}\frac{\sinh\Delta_1+\sin\Delta_2}{\cosh\Delta_1+\cos\Delta_1}\right]+$$

$$\left(\frac{I_s}{I_p}\right)^2\frac{2R_{dc2}}{\omega}\Delta_2\left[\frac{\sinh 2\Delta_2-\sin 2\Delta_2}{\cosh 2\Delta_2-\cos 2\Delta_2}+\frac{2(N_{s2}p_2^2-1)}{3}\frac{\sinh\Delta_2+\sin\Delta_2}{\cosh\Delta_2+\cos\Delta_2}\right]+$$

$$\frac{\mu_0 N_{l1}^2 p_1}{3H_w}\left\{\frac{l_{w1}d_{m1}}{\sqrt{N_{s1}}}\left(\sqrt{N_{s1}}p_1+1\right)\left(2\sqrt{N_{s1}}p_1+1\right)+l_{w1}d_{ins1}\left(p_1-1\right)\left(2p_1-1\right)\right.$$

$$\left.+2l_{w1}d_{a1}\left(p_1+1\right)\left(2p_1+1\right)+6l_{iso}d_{iso}p_1\right\}+$$

$$\left(\frac{I_s}{I_p}\right)^2\frac{\mu_0 N_{l2}^2 p_2 l_{w2}}{3H_w}\left\{\frac{d_{m2}}{\sqrt{N_{s2}}}\left(\sqrt{N_{s2}}p_2+1\right)\left(2\sqrt{N_{s2}}p_2+1\right)+\right.$$

$$\left.2d_{a2}\left(p_2+1\right)\left(2p_2+1\right)+d_{ins2}\left(p_2-1\right)\left(2p_2-1\right)\right\} \tag{6.18}$$

where l_{w1} and l_{w2} are the mean length of the primary and secondary half windings on a limb respectively, and d_{mi} and d_{ai} can be calculated using Fig. 6.4 which are as follows [6.26]:

$$d_{mi}=\frac{\sqrt{\pi}}{2}\left(\frac{d_{wi}-2t_i}{\sqrt{N_{si}}}-d_i\right)\qquad i=1,2 \tag{6.19}$$

$$d_{ai}=\frac{d_{wi}}{2}-\frac{\sqrt{\pi}}{4}\left(d_{wi}-2t_i\right)\qquad i=1,2 \tag{6.20}$$

6.2.8 Temperature Rise

The electromagnetic power loss in any electromagnetic devices associates with the increase of the temperature. Thus, the temperature rises in the MFT due to the core and winding losses which affects the insulation and the life span of the transformer. Different empirical methods have been reported in [6.2], [6.5], [6.11], [6.27], for analysing temperature rise in the transformer. In this chapter, one of the common expressions of the temperature rise is used which is as follows [6.27]:

$$\Delta T = 450\left(\frac{P_T}{K_{st}\left(A_c A_w\right)^{0.5}}\right)^{0.826} \tag{6.21}$$

where P_T is the total loss in W, and A_w is the cross-sectional area of the core window and K_{st} is a constant related to the structure of the core.

6.3 Design Methodology

The design of the MFT is traded off between the high-power density and high efficiency with including all design requirements, e.g., low leakage inductance, proper thermal management and isolation. The parameters used for design of the MFT can be divided into two groups [6.13]: (i) fixed parameters and (ii) variable parameters. The fixed parameters are the output power, voltage levels, frequency, core material, core stacking factor, turn ratio and Litz wire type. In contrast, geometrical parameters of the core, magnetic flux density, number of turns of the primary winding, the number of layers in primary and secondary windings, number of strands in primary and secondary Litz wire may be considered as free or variable parameters. In the optimisation method, a large number of free parameters are firstly made by changing the variable parameters within their specific ranges. Then, using each set of the free parameters along with the fixed parameters, different design objectives and parameters such as the core loss, winding loss, efficiency, power density, leakage inductance and temperature rise are calculated. In addition, the maximum leakage inductance, maximum temperature rise, and minimum efficiency are set in such a way that the unacceptable set of the free parameters are automatically rejected. At the same time, the free parameters and the corresponding evaluated results are stored. The process is repeated until the all sets of free parameters are executed for design consideration. Fig. 6.5 shows the flow chart of the design technique for medium frequency transformer (MFT). Due to the several conflicting objective functions, the optimisation process provides a set of optimal results instead of a single global optimal point. The optimal results are shown in Fig. 6.6 where each dot represents a unique transformer design which satisfies the all design objectives. Designer can choose any design set from the optimal results depending on the design targets, and magnetic core and Litz wire specifications.

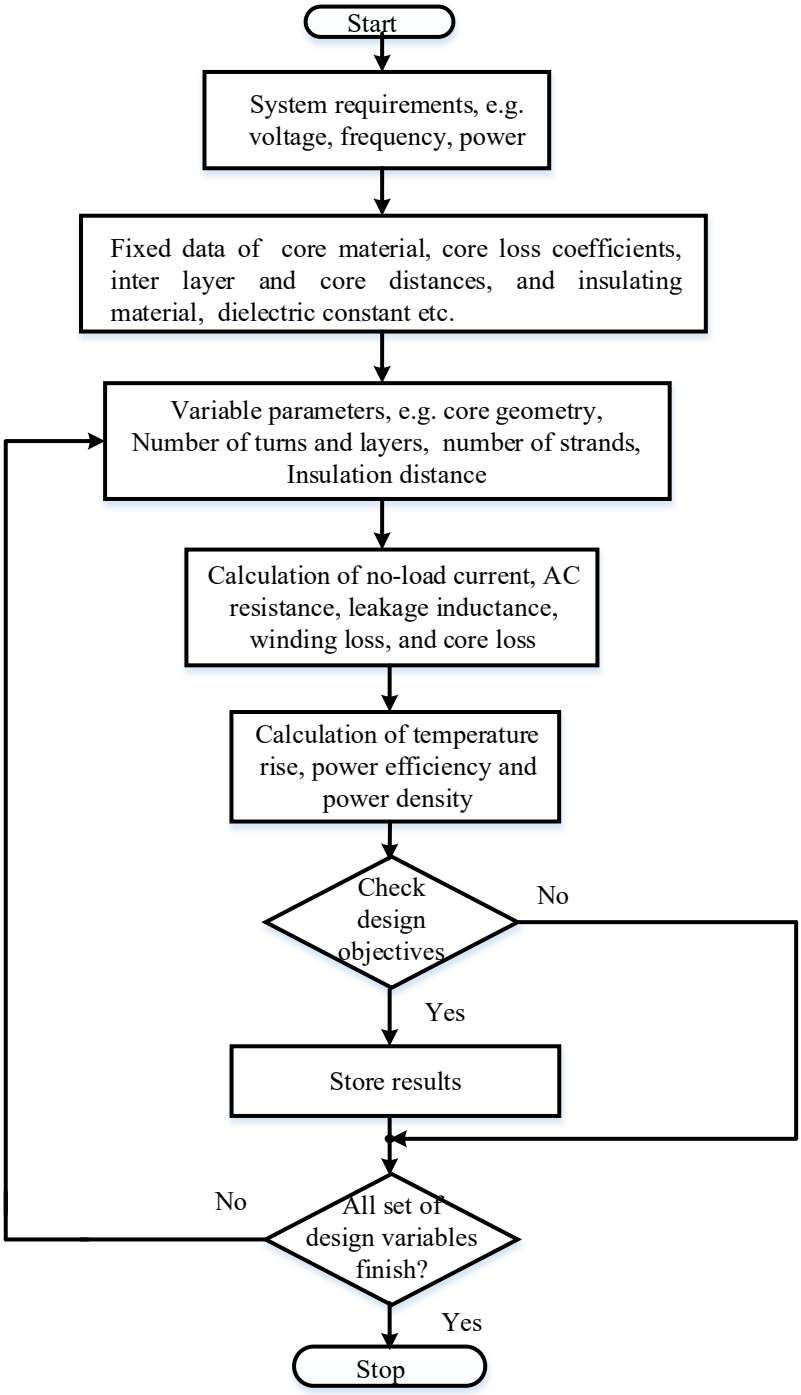

Fig. 6.5. The flow chart of the optimal design of MFT.

The above-mentioned design technique is carried out for both the inclusion and exclusion of the no-load current. The efficiency of the MFT with respect to the power density at same temperature rise limit (<70^0C) and leakage inductance (< 100 μH) is shown in Fig.

6.6. From the figure, it is observed that due to the consideration of the no-load current in the primary current, the efficiency decreases especially at the vicinity of the high-power density. A design set from the region of the high-power density of Fig. 6.6 is selected for the comparison of winding losses with and without no-load current. It is observed from Table 6.1 that the winding loss increases from 32.60 W to 33.15 W due to the consideration of the no-load current. Similarly, it is obtained that the leakage inductance from the primary side decreases due to the inclusion of the no-load current as listed in Table 6.1. The efficiency of the MFT reaches a certain maximum value of power density, and after that it decreases with the increase of power density, as shown in Fig. 6.6.

Table 6.1

Comparison of winding loss and leakage inductance from primary side of a selected MFT (2.5 kW, 200V/400V, 1.2 T)

Conditions	Winding loss	Leakage inductance
With no-load current	33.15 W	46.15 µH
Without no-load current	32.60 W	47.08 µH

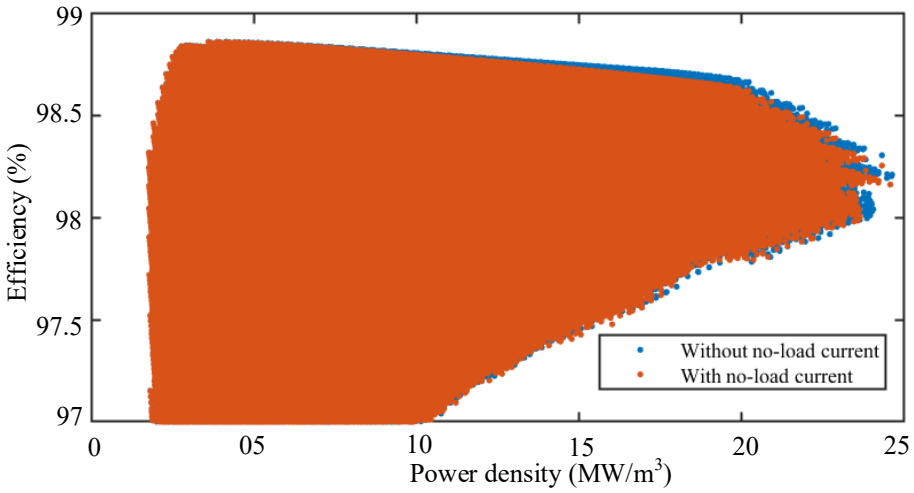

Fig. 6.6. Efficiency with respect to power density with inclusion and exclusion of the no-load current.

Based on the availability of the magnetic core and Litz wire, an optimal MFT design set is selected from the optimal design results. The specifications of the selected MFT design is shown in Table 6.2.

Table 6.2

Selected optimal design parameters of MFT (2.5 kW, 1 kHz, 200V/400V)

Parameters	Values	Parameters	Values
Number of turns per limb in primary winding, N_1	34	Magnetic flux density, B_m	1.20 T
Number of layers per limb in primary winding, q_1	2	Core loss	12.20 W
Number of turns per limb in secondary winding, N_2	68	Winding loss	33.15 W
Number of layers per limb in secondary winding, q_2	2	Power density	17.31 MW/m^3
Core height, b	50 mm	Efficiency	98.19 %
Core width, a	15.32 mm	Temperature rise	66.32 ºC
Number of strands for primary winding, N_{s1}	65	Leakage inductance	46.15 µH
Number of strands for secondary winding, N_{s2}	17	Core window height, H_w	60.29 mm
Turn ratio, n	2	Core window width, G_w	26.94 mm

6.4 Experimental Testing

For experimental verification of the design, a prototype of the MFT (2.5 kW, 200V/400V) is utilised in this study. As the MFT is generally utilised in DC-DC converters, a DC-DC converter is desired for experimental verification. Fig. 6.7 shows a DC-DC converter used for testing the MFT which is mainly based on [6.2]. A computer based digital signal processing unit is used to generate the gate pulses which are +5 V. To drive the inverters' gates of the selected DC-DC converter, the voltage of gate pulses needs to be +15 V. Therefore, a gate driver circuit is used to amplify the signals from +5 V to +15 V. Differential voltage probes are utilised to measure the voltages. Fig. 6.8 shows a photo of the experimental set-up.

For core loss verification of the proposed MFT, open circuit test is carried out. The primary and secondary voltages, and excitation current under no-load condition are shown in Fig. 6.9. The corresponding magnetic flux density is shown in Fig. 6.10. The experimental core loss is 13.07 W which is close to the simulation result (12.20 W) as shown in Table 6.2. For measuring the copper or winding loss, the short circuit test is carried out. The obtained winding loss is 35.78 W which is slightly higher than that of the

simulated loss of 33.15 W. One of the main reasons for this variation is that for modelling of the winding loss, the effect of harmonics in the load current is not considered.

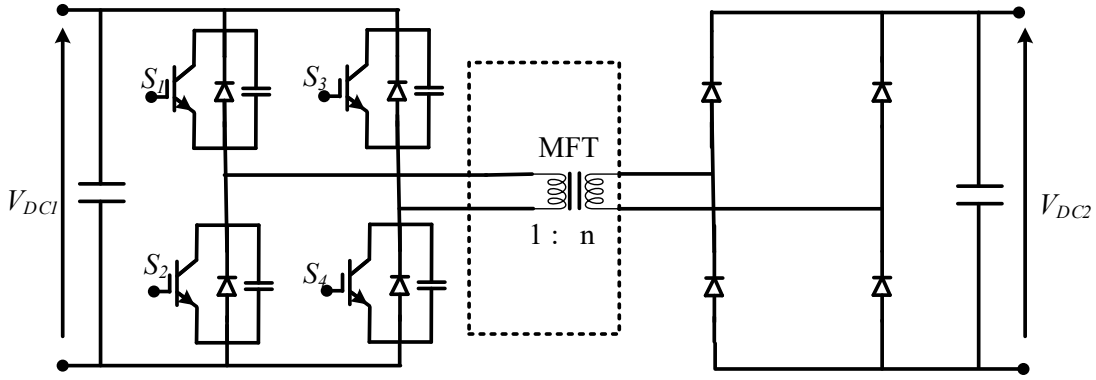

Fig. 6.7. The experimental circuit for testing the MFT.

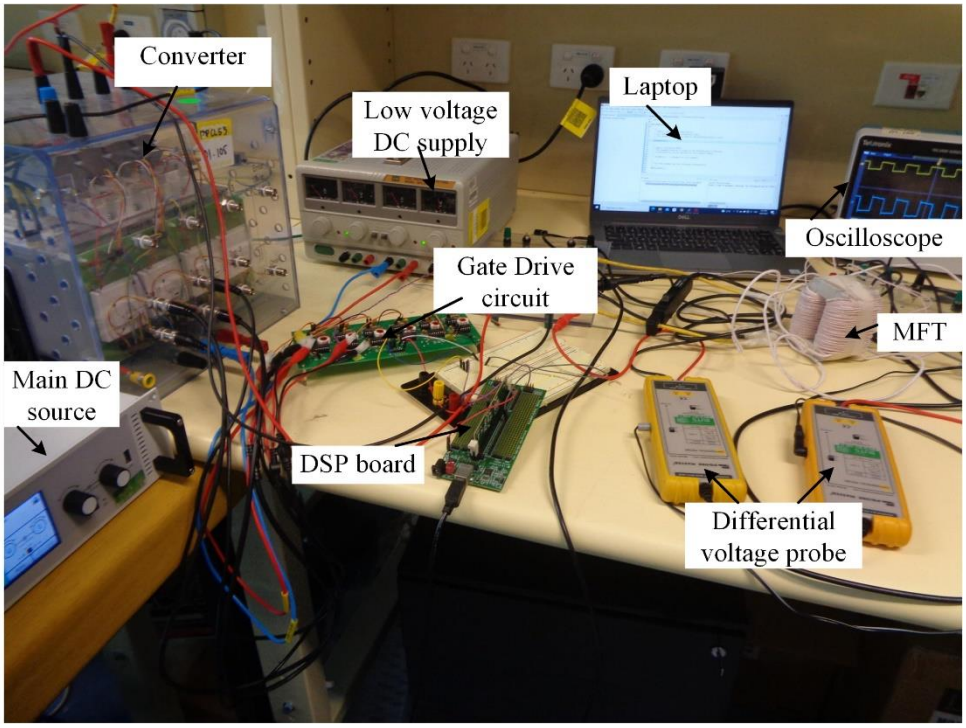

Fig. 6.8. A photo of the experimental set-up for testing the MFT.

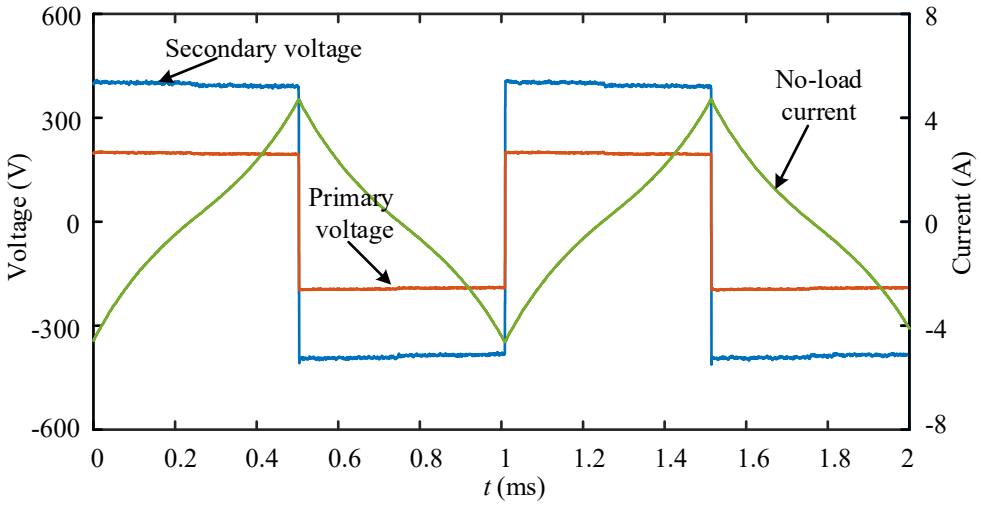

Fig. 6.9. Measured Primary and secondary voltages, and excitation current of the MFT at no-load condition.

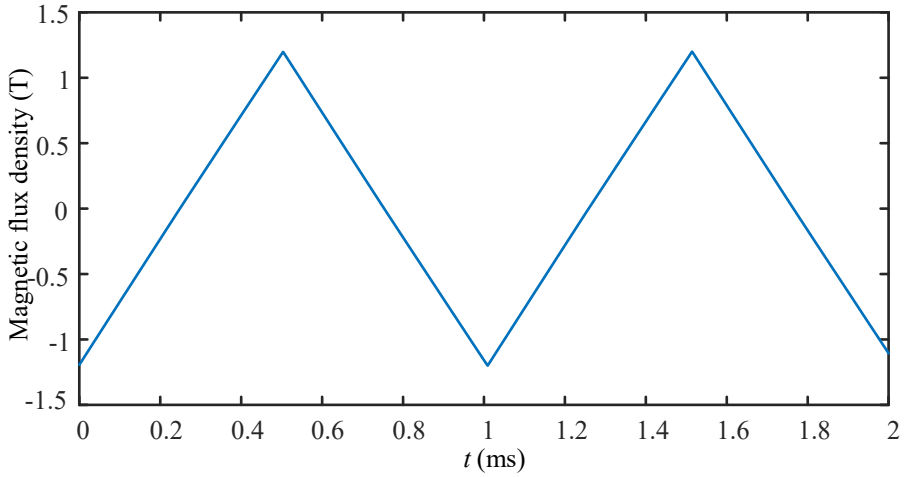

Fig. 6.10. The measured magnetic flux density of the MFT.

6.5 Conclusion

This chapters represents an optimal design of Fe-based amorphous MFT design. In the design process, power density and efficiency are considered as the optimal targets which provides a set of optimal results. According to the magnetic core and Litz wire specifications, necessary design of MFT can be chosen from the optimal results. From the obtained results, it is observed that the no-load current of MFT at high power density affects the efficiency as well as the leakage inductance. For the verification of core loss and winding loss of the MFT, open circuit test and short circuit test are conducted which shows a considerable agreement with the simulation results.

Reference

[6.1] X. She, A. Q. Huang, and R. Burgos, "Review of solid-state transformer technologies and their application in power distribution systems," *IEEE J. Emer. Sele. Topics Power Electron*., vol. 1, no. 3, pp. 186–198, Sep. 2013.

[6.2] P. Huang *et al*., "Optimal design and implementation of high-voltage high-power silicon steel core medium-frequency transformer," *IEEE Trans. Ind. Electron.*, vol. 64, no. 6, pp. 4391–4401, Jun. 2017.

[6.3] M. Mogorovic and D. Dujic, "Sensitivity analysis of medium-frequency transformer designs for solid-state transformers," *IEEE Trans. Power Electron.*, vol. 34, no. 9, pp. 8356–8367, Sept. 2019.

[6.4] T. Kauder and K. Hameyer, "Performance factor comparison of nanocrystalline, amorphous, and crystalline soft magnetic materials for medium-frequency applications," *IEEE Trans. Magn.*, vol. 53, no. 11, pp. 1–4, Nov. 2017, Art no. 8401504.

[6.5] Y. Xu, L. Chen, W. Guo, C. Shangguan, J. Zuo, and K. He, "Optimal design of medium-frequency Fe-based amorphous transformer based on genetic algorithm," *IEEE Trans. Plas. Sci.*, vol. 46, no. 10, pp. 3240–3248, Oct. 2018.

[6.6] G. Ortiz, J. Biela, and J. W. Kolar, "Optimized design of medium frequency transformers with high isolation requirements," *IECON 2010 - 36th Ann.l Conf. IEEE Ind.l Electron. Society*, Glendale, AZ, 2010, pp. 631–638.

[6.7] M. Jaritz, S. Blume, and J. Biela, "Design procedure of a 14.4 kV, 100 kHz transformer with a high isolation voltage 115 kV)," *IEEE Trans. Dielec. Elect. Ins.*, vol. 24, no. 4, pp. 2094–2104, 2017.

[6.8] S. Zhao, Q. Li, and F. C. Lee, "High frequency transformer design for modular power conversion from medium voltage ac to 400V dc," *2017 IEEE Appl. Power Electron. Conf. Exp. (APEC)*, Tampa, FL, 2017, pp. 2894–2901.

[6.9] M. Leibl, G. Ortiz, and J. W. Kolar, "Design and experimental analysis of a medium-frequency transformer for solid-state transformer applications," *IEEE J. Emerg. Select. Top. Power Electron.*, vol. 5, no. 1, pp. 110–123, Mar. 2017.

[6.10] L. Zhang, D. Zhang, H. Shui, Y. Yuan, Q. Pei, and J. Zhu, "Optimisation design of medium frequency transformer for the offshore dc grid based on multi-objective genetic algorithm," *IET Power Electron.*, vol. 10, no. 15, pp. 2157–2162, Dec. 2017.

[6.11] E. L. Barrios, A. Ursúa, L. Marroyo, and P. Sanchis, "Analytical design methodology for litz-wired high-frequency power transformers," *IEEE Trans. Ind. Electron.*, vol. 62, no. 4, pp. 2103–2113, Apr. 2015.

[6.12] E. L. Barrios, A. Urtasun, A. Ursúa, L. Marroyo, and P. Sanchis, "High-frequency power transformers with foil windings: maximum interleaving and optimal design," *IEEE Trans. Power Electron.*, vol. 30, no. 10, pp. 5712–5723, Oct. 2015.

[6.13] M. A. Bahmani, T. Thiringer, and M. Kharezy, "Design methodology and optimization of a medium-frequency transformer for high-power dc–dc applications," *IEEE Trans. Ind. Appl.*, vol. 52, no. 5, pp. 4225–4233, Sept.-Oct. 2016.

[6.14] C. P. Steinmetz, "On the law of hysteresis," *Trans. American Ins. Elect. Engr.*, no. 1, pp. 1–64, Jan. 1892.

[6.15] J. Li, T. Abdallah, and C. R. Sullivan, "Improved calculation of core loss with nonsinusoidal waveforms," *in Proc. IEEE Ind. Appl Conf. 36th IAS Annu Meeting*, Chicago, IL, USA, Sep. 30–04 Aug. 2001, vol. 4, pp. 2203–2210.

[6.16] K. Venkatachalam, C. R. Sullivan, T. Abdallah, and H. Tacca, "Accurate prediction of ferrite core loss with nonsinusoidal waveforms using only Steinmetz parameters," *in Proc. IEEE Workshop Comp. Power Electron.*, Mayaguez, Puerto Rico, USA, Jun. 3–4, 2002, pp. 36–41.

[6.17] A. Van den Bossche, V. C. Valchev, and G. B. Georgiev, "Measurement and loss model of ferrites with non-sinusoidal waveforms*," in Proc. IEEE 35th Annu. Power Electron. Spec. Conf.*, Aachen, Germany, Jun. 20–25, 2004, vol. 6, pp. 4814–4818.

[6.18] W. Shen, F. Wang, D. Boroyevich, and C. W. Tipton, "Loss characterization and calculation of nanocrystalline cores for high-frequency magnetics applications," *IEEE Trans. Power Electron*, vol. 23, no. 1, pp. 475–484, Jan. 2008.

[6.19] L. Evangelista, M. A. Carvalho, and P. A. P. Wendhausen, "Steinmetz coefficients' prediction based on processing parameters of soft magnetic composites," *IEEE Trans. Magn.*, vol. 56, no. 2, pp. 1–5, Feb. 2020, Art no. 2000205.

[6.20] Guangzhou Amorphous Electronic Technology Co. Ltd. [Online]. Available: https://www.coilcore.com/. Accessed on: Dec. 22, 2019.

[6.21] Litz wire calculation and design. (Online) Available: https://www.hflitzwire.com/litz-wire-calculation-and-design/.

[6.22] B.L. Theraja and A. K. Thereaja, "AC and DC Machines- A textbook of Electrical Technology- vol. II," S. Chand and company Ltd., India.

[6.23] W. J. Gu and R. Liu, "A study of volume and weight vs. frequency for high-frequency transformers," *in Proc. IEEE Power Electrn. Spec. Conf.*, Seattle, USA, Jun. 20–24 1993, pp. 1123–1129.

[6.24] P. L. Dowell, "Effects of eddy currents in transformer windings," in *Pro. Inst. Elect. Engs.*, vol. 113, no. 8, pp. 1387–1394, Aug. 1966.

[6.25] M. A. Bahmani and T. Thiringer, "Accurate evaluation of leakage inductance in high-frequency transformers using an improved frequency-dependent expression," *IEEE Trans. Power Electron.*, vol. 30, no. 10, pp. 5738–5745, Oct. 2015.

[6.26] J. Schutz, J. Roudet, and A. Schellmanns, "Modeling Litz wire windings," In Proc. *IEEE Ind. Appl. Conf. 32th IAS Annl. Meet.*, vol. 2, pp. 1190-1195, 5–9 Oct. 1997.

[6.27] C. W. T. McLyman, Transformer and inductor design handbook, Third Edition, Revised and Expanded, Kg. Magnetic, Inc. California, USA.

Chapter 7 Conclusion and Future Works

7.1 Conclusion

In this study, the conventional alternating (one-dimensional) and two-dimensional rotational magnetic properties of the selected Fe-based magnetic material have been measured and modelled. Moreover, a high-power density MFT is designed and implemented using the Fe-based amorphous magnetic material. The main contributions of this study are listed as follows:

(1) A generalised inverse Preisach model is proposed for modelling the alternating core loss, where the reversible magnetisation and magnetisation dependent hysteresis effects are considered. In addition, a new technique to find out the feedback coefficient of the generalised inverse Preisach model is also proposed and verified.

(2) An improved J-A model parameter identification technique, where the relative core loss error is also considered as optimisation criterion along with the general existing error criterion, is proposed for modelling the alternating core loss. The proposed parameter identification technique significantly increases the accuracy in the calculation of core loss using J-A model. In addition, a modified J-A model is proposed in order to improve the agreement between experimental and simulated results at the low magnetic induction levels.

(3) An improved and simplified analogical rotational hysteresis model under 2-D rotational magnetic field is proposed and verified for the amorphous magnetic material. Moreover, the modellings of total specific rotational losses of the Fe-based amorphous magnetic material for both circular and elliptical rotating magnetic fields are carried out in this study.

(4) An optimal design of a high-power density MFT is proposed where the effect of the no-load current is considered in empirical core loss model-based transformer

design process. The experimental verification of the design is also done in the study.

7.2 Possible Future Works

In this thesis, a Fe-based amorphous magnetic material is characterised by both experimental and mathematical ways where modified modellings have been also proposed. To improve further performance of the characterisation processes as well as its applications, many possible approaches can be considered in future. A few of the possible works are listed below:

(1) In this study, skin effect which affects the magnetic flux distribution in the core is not considered. To consider the skin effect as well as better observation of distribution of magnetic flux density in the magnetic material, the finite element analysis needs to be incorporated with the inverse Preisach or inverse J-A model.

(2) In this study, Preisach distribution function of the Preisach model is based on an experimental limiting loop of the magnetic material. Preisach model for other distribution functions which are based on first order reversible curve or gaussian distribution functions may be implemented for further improvement of the model.

(3) The optimum design of MFT can be done using finite element method to obtain high accuracy of leakage inductance, winding loss and core loss. In addition, the temperature distribution on the transformer can also be obtained which helps to find out the hot spot points in the magnetic core.

(4) For modelling of the amorphous magnetic material under rotating magnetic field, the empirical method is used in this study. Vector Preisach and vector J-A models can also be implemented for observation of the high accuracy of the core loss and magnetic flux distribution in the magnetic material.

(5) The measured rotational core loss and proposed rotational core loss model can be used for design of an amorphous core based rotating electrical machine.

(6) The magnetic flux in the core of rotating electrical machines may pass through in all direction. Therefore, the three dimensional (3-D) magnetic properties of the core material are also important for the design of the electrical machines. The 3-D magnetic properties of the amorphous magnetic material can be investigated in future.